Stony Brook University

In situ Characterization of Promoted Rh Nanocatalysts During CO Hydrogenation

A Dissertation Presented

by

Robert M. Palomino

to

The Graduate School

in Partial Fulfillment of the

Requirements

for the Degree of

Doctor of Philosophy

in

Chemistry

Stony Brook University

August 2015

Stony Brook University
The Graduate School

Robert M. Palomino

We, the dissertation committee for the above candidate for the
Doctor of Philosophy degree, hereby recommend
acceptance of this dissertation.

Michael G. White, Ph. D., Advisor
Professor, Department of Chemistry

Trevor Sears, Ph. D., Chairperson of Defense
Professor, Department of Chemistry

Stanislaus Wong, Ph. D., 3rd Member of Defense
Professor, Department of Chemistry

Charles T. Black, Ph. D., 4th Member of Defense
Senior Scientist, Brookhaven National Laboratory

Sanjaya Senanayake, Ph. D., Outside Member
Associate Chemist, Brookhaven National Laboratory

This dissertation is accepted by the Graduate School

Charles Taber
Dean of the Graduate School

Abstract of the Dissertation

In Situ Characterization of Promoted Rh Nanocatalysts During CO Hydrogenation

by

Robert M. Palomino

Doctor of Philosophy

in

Chemistry

Stony Brook University

2015

The world's dependence on the limited supply of fossil fuels has provided the motivation for research into alternative renewable fuel sources. Ethanol is a promising alternative due to its low toxicity, high energy density, and compatibility with the current fuel distribution system. An attractive route to ethanol production would be through the conversion of synthesis gas or 'syngas' ($CO + H_2$), which is currently used to produce methanol, hydrogen, and synthetic fuels (diesel and gasoline). However, there are currently no commercially used catalysts for efficient ethanol production from syngas. In general, catalysts for syngas conversion to ethanol should promote C–C coupling while suppressing methane formation. Previous studies have shown that oxide supported bi-metallic catalysts composed of noble and early transition metals can potentially meet these catalytic requirements, but identifying the structure and active phase of these systems under reaction conditions remains a significant challenge. This work focuses on *in situ* characterization of Fe-Rh bi-metallic catalysts supported on titania (TiO_2) and ceria (CeO_2). Synchrotron based techniques (X-ray diffraction, pair distribution function analysis, and X-ray

absorption spectroscopy) are used to elucidate catalyst structure under reaction conditions, which is compared to the catalytic efficiency obtained via reactor studies from mass spectrometry and gas chromatography.

The first catalytic system studied is bimetallic Fe–Rh/TiO_2, synthesized via two deposition methods: diblock co–polymer reverse micelle template and incipient wetness impregnation. Both approaches are used to control the particle size and overall composition in order to determine the effect each have on the catalyst structure. In general, the addition of Fe results in alloying with Rh. Further increasing Fe loading serves to increase the alloy concentration, but alloy formation is limited as metallic Fe forms in catalysts that contain over 4 wt% Fe. Ethanol selectivity was found to be dependent upon the alloyed Fe concentration. Fe–modification was also found to suppress the overall CO conversion when coupled with the methane suppression, the conclusion is that the alloying of Fe and Rh blocks active Rh sites responsible for methane formation and other side reactions. Fe from the alloy and metallic deposits was also found to be carburized into Fe_3C during the reaction, but the presence of Fe_3C had a negligible effect on the product distribution and CO conversion.

The second major catalytic system studied consists of Fe–promoted Rh/CeO_2, synthesized via the incipient wetness impregnation method. The alloying of Fe and Rh is promoted on CeO_2 compared to TiO_2, where a larger concentration of Fe–Rh alloy was observed at lower Fe loadings than on TiO_2. Metallic Fe was not formed, but Fe–Rh alloy formation began to plateau at ~5 wt% Fe, indicating that there is a limit to alloy formation. Fe from the alloy was carburized during the reaction, but as with TiO_2, a negligible effect was observed on product distribution and CO conversion. Ethanol selectivity also peaked at a lower Fe loading than TiO_2–supported catalyst due to the promotion of Fe–Rh alloy on CeO_2. Additionally, the ethanol enhancement

peaked at ~ 3 wt% alloyed Fe and a further increase of alloy concentration lead to the suppression of ethanol and a subsequent increase in methane selectivity. Lastly, CeO_2 differs from TiO_2 in that an interface with Fe promotes ethylene production. Overall, Fe–Rh/CeO_2 appears to have reactivity comparable to TiO_2–supported catalysts, where the maximum CO conversion and ethanol selectivity are arguably the same.

Dedication Page

This thesis is dedicated to my loving and supportive family.

Table of Contents

List of Tables

List of Figures

List of Abbreviations

ML: Monolayer

DFT: Density Functional Theory

KMC: Kinetic Monte Carlo

XAS: X-ray Absorption Spectroscopy

EXAFS: Extended X-ray Absorption Fine Structure

XANES: X-ray Absorption Near Edge Structure

SEM: Scanning Electron Microscopy

AFM: Atomic Force Microscopy

TEM: Transmission Electron Microscopy

XRD: X-ray Diffraction

PDF: Pair Distribution Function

dPDF: difference Pair Distribution Function

CFN: Center for Functional Nanomaterials

PS–b–PVP: Polystyrene–b–poly (vinyl pyridine)

MW: Molecular Weight

AAO: Anodic Aluminum Oxide

ALD: Atomic Layer Deposition

GC: Gas Chromatography

TCD: Thermal Conductivity Detector

GHSV: Gas Hourly Space Velocity

NSLS: National Synchrotron Light Source

APS: Advanced Photon Source

EDS: Energy Dispersive Spectroscopy

MS: Mass Spectrometry

SR: Synchrotron Radiation

SMSI: Strong Metal Support Interaction

Acknowledgments

I would like to acknowledge my parents, Rohan and Pauline, and my wife, Sharde for their endless support and encouragement during my graduate career. I would also like to acknowledge my children, Hannah and Josiah, for the motivation they gave me to earn my doctorate. I would like to thank my brother, Omar and my cousin, Christopher for their overall support and guidance in my life outside of graduate school. Additionally, I would like to thank my adviser, Michael G. White, for his guidance during my graduate career that helped to mold me into a better scientist. I would also like to thank Charles T. Black for all of his support in the synthesis of catalysts at the CFN, not only in regards to using the facility, but also for the helpful discussion that lead to successful syntheses. I would like to acknowledge Joe Magee for his assistance in synchrotron experiments and in the countless hours editing my work. Last, but not least, I would like to thank Jonathan Hanson for his guidance in PDF and XRD synchrotron experiments.

Chapter 1. Introduction

Converting synthesis gas or 'syngas' ($CO + H_2$) into useable liquid fuels (alcohols and other oxygenates) has been of interest for decades. Currently, syngas is used to catalytically synthesize methanol via the Cu-based catalyst, $Cu\text{-}ZnO/Al_2O_3$.[1] Ethanol is a significant improvement over methanol due to its higher energy density and non-toxicity. Unfortunately, a commercially viable catalyst for the direct conversion of syngas to ethanol has yet to be identified. Catalysts for the conversion of syngas to ethanol should have C-C coupling abilities and be able to suppress the formation of methane. Oxide supported Rh bi-metallic catalysts have been shown to enhance ethanol production while suppressing methane formation. Transition metal promoters, such as CeO_2, Fe, Mn, and Mo, have shown to enhance ethanol selectivity and suppress methane formation.[2-4]

Although no single reaction scheme has been accepted, general schemes for direct conversion of H_2 + CO to ethanol have been proposed. Figures 1.1 shows a possible reaction schemes for CO conversion to ethanol over Rh-based catalysts.[2] A general consensus in these schemes is that major steps towards enhancing ethanol selectivity are the dissociative adsorption of CO and the insertion of CO into CH_x to form a "enol" species that can be hydrogenated to ethanol. A less desired pathway would be the hydrogenation of adsorbed CO or CH_x, which leads to methanol and methane formation, respectively. It becomes apparent that there needs to be a balance between dissociative and non-dissociative adsorption of CO in order to both produce the CH_x species and have non-dissociated CO to insert into the CH_x species. Rh primarily adsorbs CO dissociatively, which results in the production of methane.[2] Due to this fact, the promoters used to enhance ethanol selectivity must serve several purposes in order to

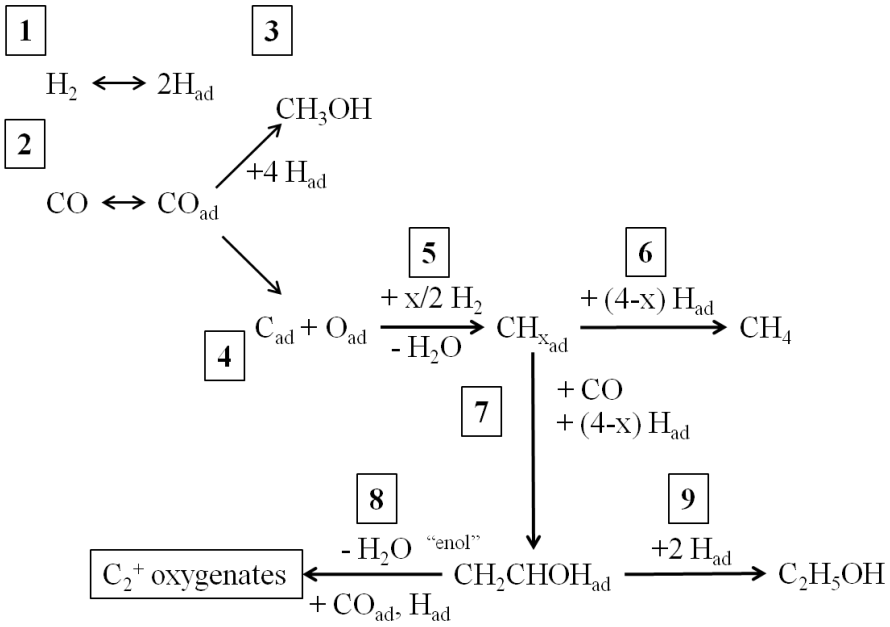

Figure 1.1: General reaction scheme for CO conversion to ethanol. *Adapted from [2].

maximize ethanol selectivity and overall activity. The promoter must facilitate some non-dissociative adsorption of CO to form the "enol" species without suppressing all dissociative adsorption of CO. It should also suppress the hydrogenation of the CH_x species to prevent the formation of methane. Alternatively, it could promote CO insertion, which would have the same effect as CO insertion and CH_x hydrogenation are competing processes.

One notable promoter of Rh, known to enhance ethanol selectivity while simultaneously suppressing methane formation is Fe. Burch *et al.* studied the effect that Fe loading has on the product distribution and CO conversion on Rh supported on Al_2O_3.[5] The authors observed that the methane selectivity lowered with increasing Fe loading, while ethanol increased. This suggests that ethanol is produced at the expense of methane. It is likely that Fe modifies steps 6 and 7 in the reaction scheme (Figure 1.1), i.e., Fe suppresses CH_x hydrogenation and promotes CO insertion, through the strengthening of the Rh-CH_x interaction and increased binding energy of CH_3CO, respectively. One other important observation in this study is that the promotional effect of Fe reaches a maximum at 10 wt%, after which the ethanol selectivity drops and the methane selectivity rises. They also observed a similar relationship with Fe loading and CO conversion, where CO conversion reaches a maximum with an Fe loading of 10 wt% Fe. According to the authors, a Fe loading of 11.7 wt% would be equivalent to one full monolayer (ML) on the Al_2O_3 support so that higher loadings would block Rh active sites essential for the production of ethanol. A more recent study by Haider *et al.* explored Fe-promotion on Rh supported on TiO_2 and compared it to SiO_2, which was had been used predominantly for Rh-based catalysts.[6] The authors found that changing the support from SiO_2 to TiO_2 increased CO conversion and ethanol selectivity even on unpromoted Rh catalysts. This enhancement was attributed to the increased reducibility of TiO_2 compared to SiO_2. Additionally, Fe-promoted Rh

supported on TiO_2 exhibits a higher CO conversion than its SiO_2 supported counterpart. Overall, the interface with TiO_2, and its oxygen storage capability, serves to significantly enhance CO conversion and ethanol production on Rh catalysts with Fe promotion and in the absence of Fe–promotion.

Density Functional Theory (DFT) and Kinetic Monte Carlo (KMS) simulations also serve to elucidate the promotional role of Fe in CO conversion to ethanol. An early study by Choi *et al.* discovered that when Fe forms a surface alloy with Rh, it can serve to increase the barrier of CH_3 hydrogenation to methane, shown in step 6 of Figure 1.1.[7] By inhibiting one of the major steps that compete with ethanol production, the selectivity to ethanol is enhanced. A theoretical study later performed by Yang *et al.*, determined that Fe prefers to be subsurface until reactants and intermediates are adsorbed on the surface, at which point the Fe is drawn to the Rh surface.[8] In this study multiple dopants were considered and Density Functional Theory (DFT) combined with Kinetic Monte Carlo (KMC) calculations determined their effect on the critical steps in CO hydrogenation (HCO formation, CH4 production, and CO insertion). Fe, Mo, and Mn were all studied as dopants in Rh(111), but the results show that Fe has the highest ethanol selectivity. This study also demonstrated that Fe takes part in the reaction by interacting with reactants and intermediates (ensemble effect) and also strengthens the Rh-CH_3 interaction which hinders CH_3 hydrogenation to form methane (ligand effect).

Several structural studies have also been performed that attempt to elucidate the structure of Fe–promoted Rh nanoparticles. These studies attempt to correlate atomic structure with reactivity that can in turn determine the active phase. An early study by Ichikawa *et al.* determined the structure of reduced Fe-Rh/SiO_2 catalysts to be a combination of Fe-Rh alloy and Fe^{3+} at the interface between Rh and SiO_2.[9] Extended X-ray Absorption Fine Structure

(EXAFS) measurements at the Fe and Rh K-edges were analyzed to obtain a Fe–Rh bond length of 2.61 Å. Only alloyed Fe^0 and Fe^{3+} were found in this study. Additionally, they attribute the resistance to sintering of Fe–Rh particles to the anchoring of Rh via the interface between Rh, Fe, and the support.

More recently, an *in situ* study was conducted on Fe–Rh/TiO_2 catalysts by Gogate and Davis.[10] In this study, the catalyst that showed the highest efficiency in the work of Haider *et al.*, 2 wt% Rh– 2.5 wt% Fe/TiO_2, was characterized via X-ray Absorption Near Edge Structure (XANES) and EXAFS on as-synthesized and reduced catalysts, and catalysts under CO hydrogenation reaction conditions. This study found Fe and Rh to be in the +3 oxidation states prior to reduction. Both metals reach their maximum reduction at a temperature lower than 270 °C (reaction temperature), with Rh and Fe in the 0 and +2 oxidation states, respectively. Two important structural features are emphasized in this work: (1) Rh has an excess electronic charge, determined by an Rh E_0 energy shift of –2.1 eV from the Rh foil standard and (2) TiO_2 is partially reduced and forms bonds with Rh through Ti or lattice bound oxygen. The excess electronic charge on Rh facilitates CO dissociation, and the interface with reduced TiO_2 and FeO enhances ethanol production due to their oxophilic nature. Unlike the results found by Ichikawa *et al*., direct evidence of Rh–Fe bonding was not found. This conclusion was based primarily on the fact that a matching peak due to a Rh–Fe bond was not found in the Fe K-edge and Rh K-edge EXAFS data. Instead, the feature observed in the Rh K-edge EXAFS was assigned to Rh–Ti or Rh–O bonds following the work of Tauster *et al.* and Resasco *et al.*[11, 12] The two latter studies conclude that Rh supported on TiO_2 can undergo a strong metal-support interaction, or SMSI, where the TiO_2 is partially reduced at the interface with the supported Rh nanoparticles. Based on the collection of these findings, Gogate and Davis concluded that the

enhanced ethanol selectivity observed on Rh–FeO_x/TiO_2 was due to the direct interaction between Rh and the partially reduced TiO_2 and FeO.

This dissertation focuses on *in situ* characterization of Fe-promoted Rh nanocatalysts to elucidate the structure of the active phase during CO hydrogenation to ethanol. Various microscopy techniques are utilized to characterize the catalyst's morphology and particle size distributions including Scanning Electron Microscopy (SEM), Atomic Force Microscopy (AFM), and Transmission Electron Microscopy (TEM). Additionally, X-ray based techniques performed at synchrotron radiation facilities are used to determine the electronic/atomic structure and phase composition of the catalysts under reducing and reaction conditions (CO hydrogenation). X-ray diffraction (XRD) is used to identify phases, chemical composition, and lattice constants. X-ray absorption spectroscopy (XAS) is used to determine the local electronic and atomic structure. Difference pair distribution function (dPDF) analysis is used in conjunction with XRD to analyze the short range ordering or local atomic structure of the active components , i.e., Fe, Rh, and any interfacial phases formed from interaction of Fe and Rh with the support.

Chapter 2. Experimental Section

This chapter describes the experimental techniques used to obtain the data presented in this dissertation. Section 2.1 describes the sample synthesis for the catalysts studied, section 2.2 describes the microscopy of the catalysts, section 2.3 describes the reactivity measurements and catalytic reactor design, and section 2.4 focuses on the X-ray structural techniques that are used to characterize the catalysts atomic/electronic structure.

2.1 Catalyst synthesis

All catalyst syntheses were performed in part at the Center for Functional Nanomaterials (CFN). This user facility has all the necessary equipment for self-patterning and sample processing (calcination, hydroscopic material handling, and cleaning via Rh-plasma and UV-ozone) necessary for the fabrication of the catalysts studied in this dissertation.

2.1.1 Di-block copolymer Micelle Templating

Model catalysts are simplified versions of complex real catalysts, which are typically polycrystalline powders of varying sizes and shapes and have multiple interactions of reactants with the different phases in the catalyst. The complexity of real catalysts, make the studies of specific interactions difficult, due to inability to distinguish the effects of one interaction from another. Model catalysts represent an isolated interaction, whose effect on catalytic activity can be studied independent of the other interactions found in the complex catalyst. In an attempt to synthesize a model catalytic system, a sub-monolayer film of metal nanoparticles was patterned

on a single crystal substrate (generally natively oxidized Si (100)). In order to control the particle size and spacing, we take advantage of the self-assembly nature of di-block copolymers.[13-15] Polystyrene–block– poly (4-vinyl pyridine) (PS–b–P4VP) is a copolymer that, when dissolved in toluene, is capable of forming an inverse micelle with a hydrophilic core and hydrophobic corona. When deposited on a planar substrate, these inverse micelles can self-assemble into a pseudo-hexagonal pattern. The hydrophilic core of these micelles is capable of binding transition metal precursors via an electrostatic interaction of the metal precursor ion with the electron-rich nitrogen in the pyridine ring, which can be deposited along with the micelles. The copolymer micelle can then be decomposed via oxygen/hydrogen/argon plasma, calcination in air, or UV-ozone cleaning to leave nanoparticles on the surface in the same pseudo-hexagonal pattern as the micelles which preceded them. The particle size can be controlled in two ways: (1) increasing the amount of metal precursor, which results in more metal atoms bound to each micelle core and (2) increasing the MW of the P4VP block, which increases the size of the micelle core that effectively allows more metal atoms to bind to the micelle core.[13, 14] The particle spacing is increased by increasing the MW of the polystyrene block, which increases the size of the corona that separates the loaded micelle cores and after eliminating the polymer, results in a larger space between the metal nanoparticles. A schematic of the process is shown in Figure 2.1.

Using a template in the deposition of Rh–Fe bi-metallic particles provides control over the particle spacing, size, and composition independently, which is necessary to discover the effect that each has on the catalyst's structure and ultimately the catalytic efficiency in the CO hydrogenation to ethanol reaction. The reverse micelle solution is prepared by dissolving 0.2 wt% PS–b– P4VP in toluene then stirring for 24 hours at 80 °C.

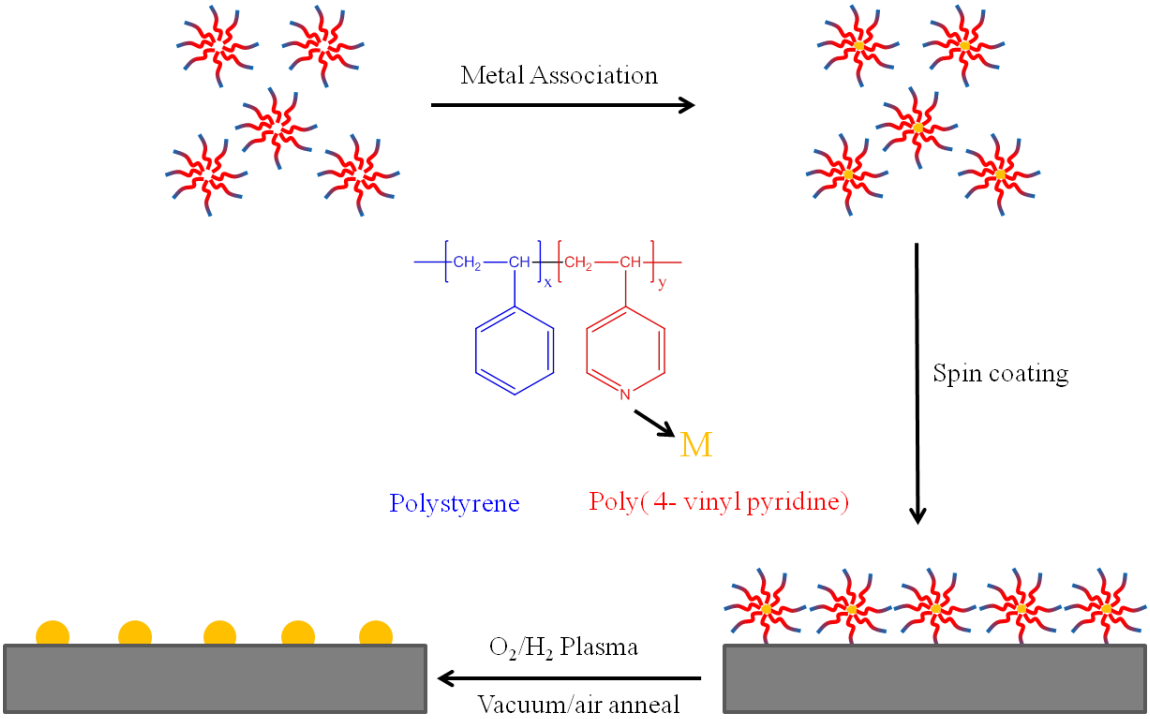

Figure 2.1: Schematic of nanoparticle formation from polymer micelle template.

The metal precursor is added to the micelle solution up to a maximum of 1 molar equivalent to the number of moles of vinyl pyridine and allowed to stir for a minimum of 48 hrs at room temperature (Rh = rhodium (II) acetate dimer, Fe = iron (III) chloride hexahydrate). The solution is then filtered through a 100 nm pore–sized filter to eliminate precursor that is not dissolved and associated inside of the micelles, which otherwise would deposit onto the substrate and disrupt the film. The loaded micelle solution is spin coated (1000-5000 rpm) onto a substrate, where the coating speed that produced an evenly coated micelle film is chosen. After deposition, the film is treated with an oxygen plasma (300 mTorr, 110W, 5 min), UV/ozone cleaning (30 min), or calcination in air (500 °C, 30 min) to decompose the polymer and leave metal (–oxide) nanoparticles in the same self- assembled pattern as the micelles. The reverse micelle template method can also be used to make powdered catalysts. The loaded micelle solution is added to Degussa P-25 TiO_2 to the desired wt% of metal and the slurry is dried overnight at 120 °C and subsequently calcined at 500 °C in air for 4 hours. The calcined powder is then crushed with a mortar and pestle into a fine powder.

2.1.4 Incipient Wetness Impregnation

Powdered catalysts are also synthesized via incipient wetness impregnation of the nanoparticulate metal oxide powders, TiO_2 and CeO_2. Rhodium (III) nitrate hydrate and iron (III) nitrate nonahydrate aqueous solutions are added drop−wise to the metal oxide powder until a paste is formed. Rhodium (III) nitrate hydrate is measured to maintain 2 wt% Rh content in all catalysts, while iron (III) nitrate nonahydrate is varied to produce 1−8 wt% Fe content. The paste that is formed from the aqueous nitrate solution and metal oxide powder is dried overnight at 120

°C before calcination in air at 450 °C for 4 hours. The dried and calcined paste is then crushed with a mortar and pestle.

2.2 Microscopy

Various microscopic techniques were utilized to characterize the catalyst's morphology: Atomic Force Microscopy (AFM), Scanning Electron Microscopy (SEM) was primarily used to study micelle-templated nanoparticle films deposited on single crystals. High Resolution Transmission Electron Microscopy (HRTEM) and Scanning TEM (STEM) were used to study powdered catalysts and micelle-templated nanoparticles deposited onto lacey C/Cu TEM grids.

2.2.1 Atomic Force Microscopy (AFM)

AFM is a microscopic technique that has a vertical resolution of <1 nm, but a lateral resolution of > 10 nm, which is largely dependent on the condition of the probe tip. Al coated AFM cantilevers were used in tapping mode to image the supported nanoparticles. In tapping mode, the cantilever taps against the surface via a frequency modulation. AFM utilizes a HeNe laser that is reflected off the Al coated side of the cantilever and the signal is measured by a photodiode detector. When the probe tip touches a particle or dip on the surface, the deflection of the laser changes and through a feedback mechanism, the probe is raised or lowered. By scanning the probe along a preset area of the surface, a topography image can be collected when the signal from the photodiode is converted into height. A depiction of the process in which an AFM image is collected is shown in Figure 2.2. The morphology of the particles on the surface (order, pattern, density of particles) can be determined in addition to an accurate measure of particle height, which can roughly be compared to particle diameter.

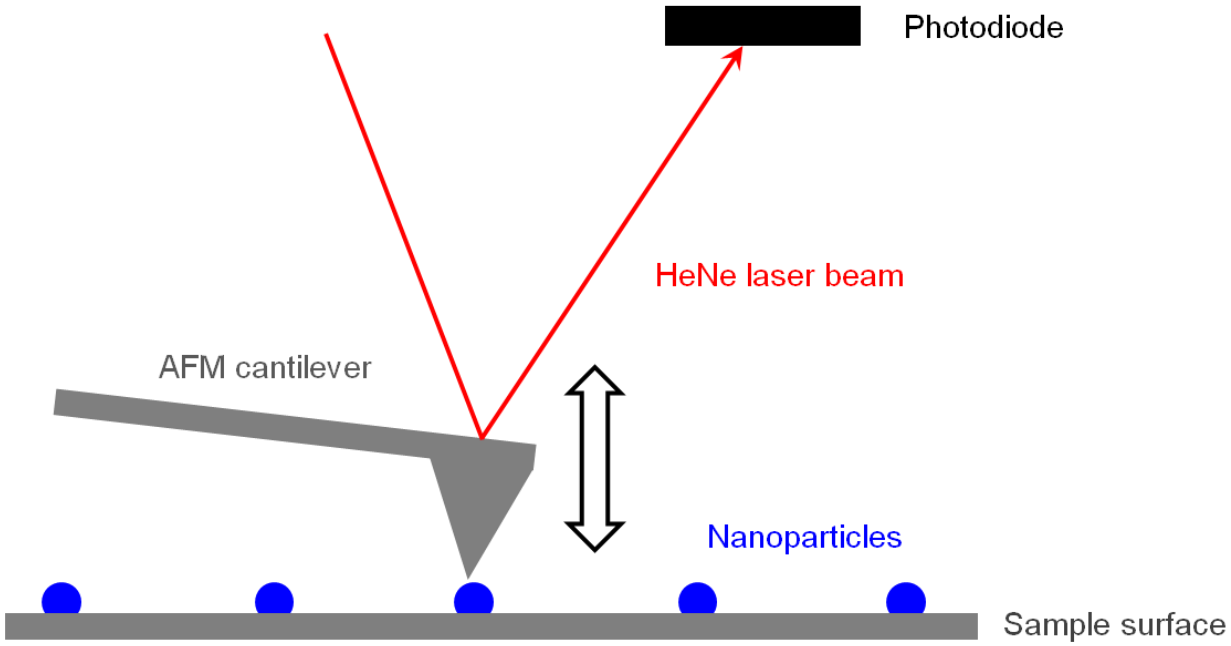

Figure 2.2: An illustration of the process in which an AFM image is collected.

A Veeco Multimode V Scanning Probe Microscope (SPM) with an AFM head was used to collect AFM images of bi-metallic Rh–Fe micelle template nanoparticles on Si(100) substrates, where the height profile of the supported nanoparticles was generated and subsequently used to calculate a particle size distribution.

2.2.2 Scanning Electron Microscopy (SEM)

SEM is another microscopic technique used to determine the morphology of the catalysts prepared by the micelle template method. A high-energy electron beam is accelerated towards the sample by electromagnetic lens. The focused beam is swept across an area of the sample by rastering with scan coils and the secondary + back–scattered electrons generated from the bombardment of the electron beam with the sample is detected to form an image. An illustration of an SEM is shown in Figure 2.3 to describe the process. SEM is capable of distinguishing different elements due a contrast difference, which is the result of differences in electron density of the atoms in the material. In comparison to AFM, SEM has a superior lateral resolution, but has no vertical resolution. Determination of the particle height is only attainable by cross–sectional imaging. SEM images bi-metallic Rh–Fe micelle template nanoparticles on Si(100) were collected on a Hitachi S-4800 HRSEM used at an acceleration voltage of 5.0 kV. The particle diameters of individual nanoparticles obtained from images using the S-4800's software were used to calculate particle size distributions.

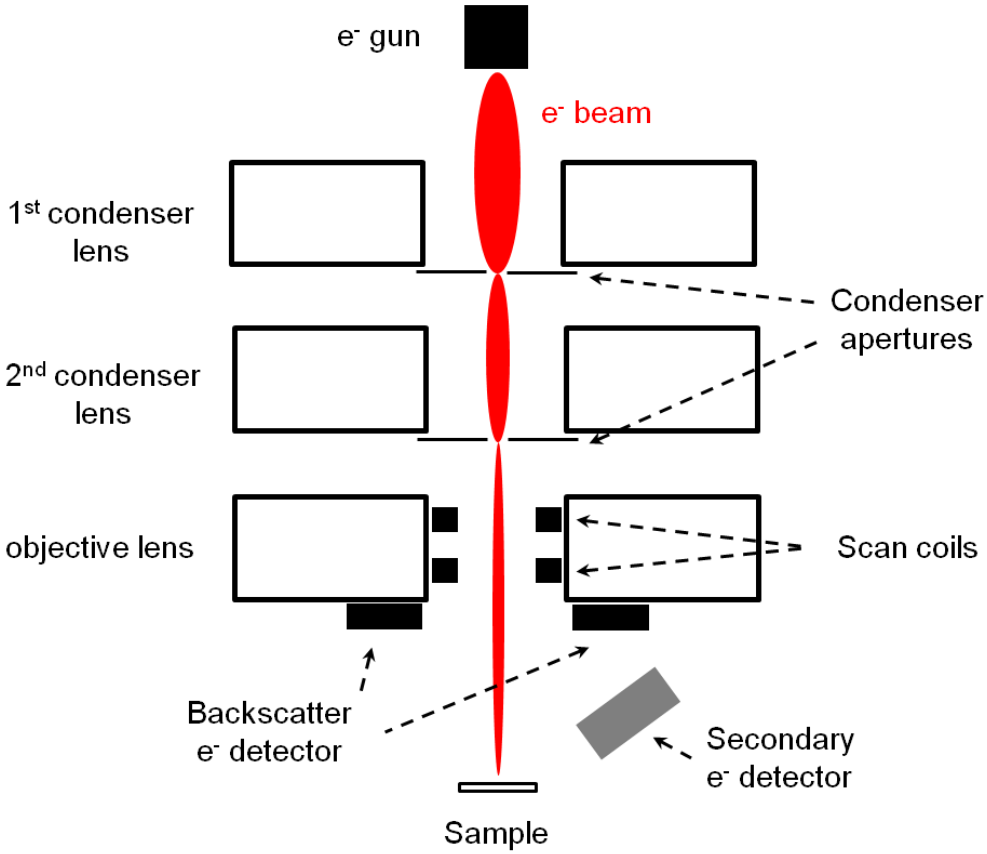

Figure 2.3: Depiction of a SEM with labeled internal components.

2.2.3 Transmission Electron Microscopy (TEM)

TEM is a superior microscopy that has a point–to–point resolution as low as 0.1 nm or 1 Å on state-of-the-art microscopes. The visualization of single atoms is possible under HRTEM magnification of particles where the beam is orthogonal to a crystal plane. The process of TEM differs from SEM in that the electron beam that is accelerated towards the sample is absorbed by the sample and a CCD detector located below the sample collects the portion of the beam not absorbed. Unlike SEM, a rastering of the beam is not necessary to produce an image. Similar to SEM, TEM image contrast is dependent on the electron density of the atoms in the material, which can distinguish different elements from one another. TEM can also be coupled with Energy Dispersive Spectroscopy (EDS) where the electron beam is used to eject an electron from an inner shell of the material leaving a hole, and an electron from an outer shell relaxes to fill that hole, releasing X-rays of an energy characteristic to the atoms in the material. This process is shown in Figure 2.4. Using EDS, the atomic and chemical composition can be qualitatively determined.

Two different TEM's were used to image catalysts synthesized from both methods described earlier: (1) a JEOL 2100F operating at a 200 kV acceleration voltage and (2) a Tecnai G^2 F20 S-TWIN operating at a 200 kV acceleration voltage. For micelle-templated nanoparticles, the loaded micelle solution was drop–cast on a lacey carbon/Cu TEM grid and calcined in air at 500 °C for 5 min or UV/ozone cleaned for 30 min. For powdered catalysts, samples were drop-cast from alcohol suspensions onto lacey carbon/Cu TEM grids. EDS was used to determine the relative amounts of Rh and Fe in the entire sample, in addition to spot scans of individual particles, which determined the location of Fe in relation to Rh.

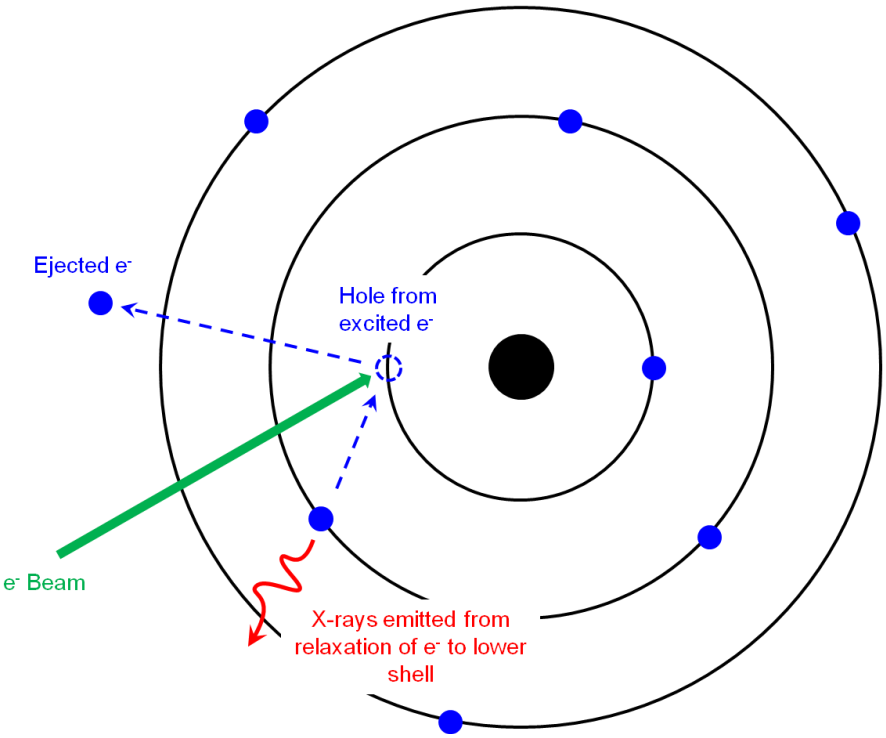

Figure 2.4: An illustration on the theory of EDS.

HRTEM was utilized to determine size distributions and crystallographic domains of selected particles, which was done by matching the Fourier coefficients and structure factor amplitudes obtained in the Fourier transform of the HRTEM to those found in a database of crystal structures.

2.3 Reactivity Measurements

Reactivity studies were carried out to determine selectivity towards various molecular products during CO hydrogenation. The catalyst was loaded into a 1/8″ OD quartz capillary tube plugged with quartz wool. Sample heating is provided by a filament wrapped around the capillary.[16] The temperature was monitored with a thermocouple in close contact to the sample. Sample temperature was controlled via current with a power supply connected to the filament heater. Reactant gases (CO/H_2) flowing through the reactor were controlled by mass flow controllers (MKS Instruments) and the output of the reactor was directed either into a vacuum chamber equipped with a mass spectrometer (MS; RGA 300, Stanford Research Systems) via a 75 μm ID fused silica capillary or into a gas chromatograph (Agilent 3000A Micro GC) via a heated 1/8 ″ OD stainless steel tube. The base pressure of the vacuum system was typically 1×10^{-10} Torr. During product sampling the pressure would rise to 4×10^{-6} Torr. The mass signals were quantified by the enhancing the Faraday cup signal with an electron multiplier. Due to the high chamber pressure during product sampling, the voltage on the electron multiplier was kept at 1852 V. A picture and diagram of the reactor study experimental setup is shown in Figure 2.5

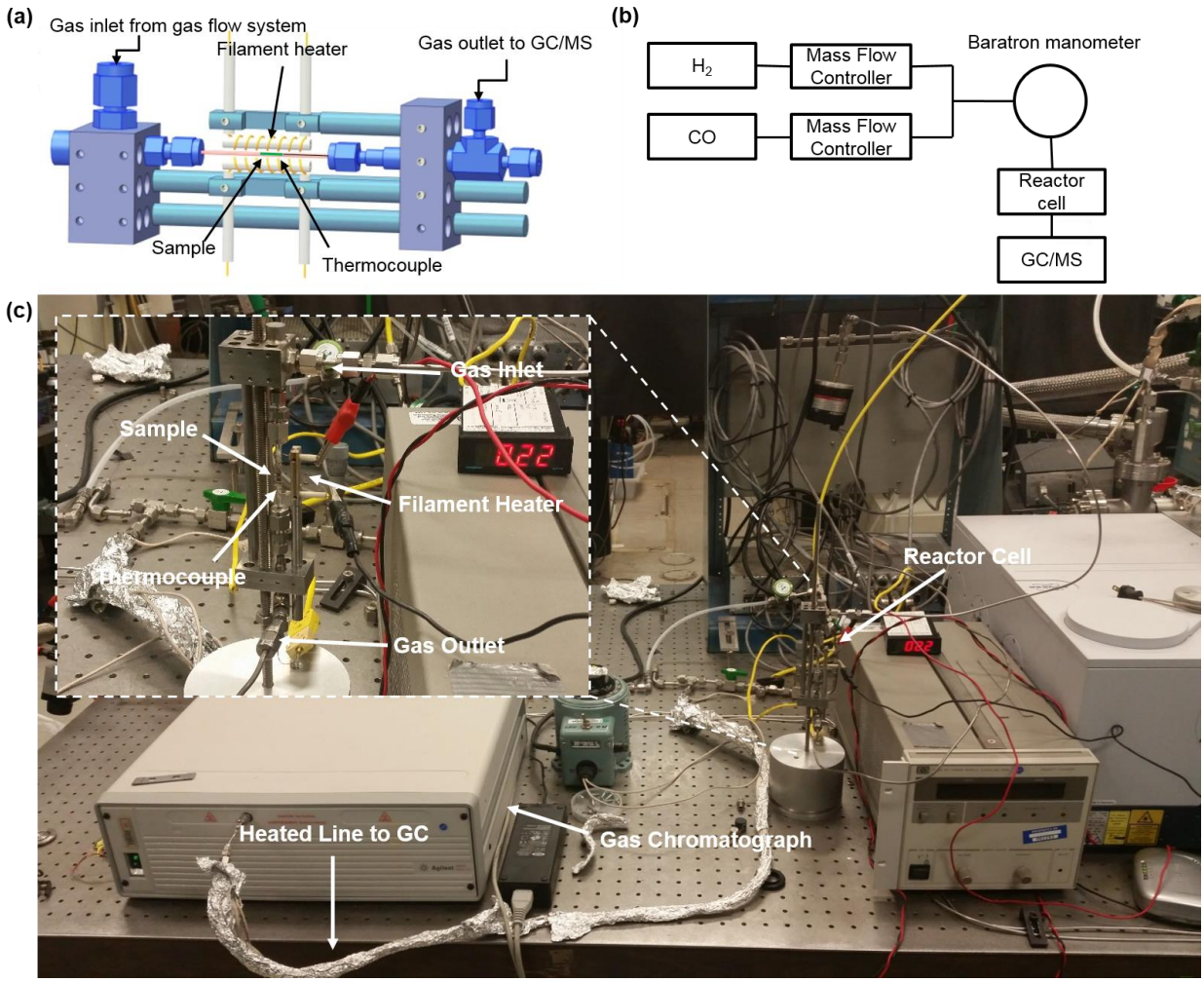

Figure 2.5: Reactor study experimental setup: (a) Labeled schematic of reactor cell, (b) Diagram of gas flow system consisting of reactant gas, mass flow controllers, and baratron manometer, (c) picture of *in situ* reactor coupled with Agilent 3000A Micro–GC.

For product analysis using the mass spectrometer, sensitivity factors at specific masses (SF_{mass}) were calculated for each targeted gas product (methane, methanol, ethanol, ethyl acetate, and acetaldehyde) by measuring the ion signals for the most prominent fragment ions at four different pressures. These target gases are determined by what is expected to be formed and what products were able to be distinguished by analyzing the mass spectra of the products. The mass spectra along with the product sensitivity factors for each product, collected by an electron multiplied signal with a multiplier voltage of 1852 V and electron energy of 70 eV, indicating the fragment ions used and their abundances in our mass spectrometer are shown in Figure 2.6. These data were then used to determine the relative product yields under specific reaction conditions. As many of the products yield the same fragment ion, e.g., mass 31 from methanol and ethanol, it was necessary to account for contributions from all products to individual mass fragments in order to extract meaningful product yields. The fragmentation patterns were used to differentiate each product's contribution to any particular fragment.

The gas chromatograph (GC) is equipped with 3 different columns for separating methane and carbon monoxide (molecular sieve MS-5A), higher hydrocarbons (Agilent Plot-U) and oxygenates (Stabilwax). All columns use a thermal conductivity detector (TCD) for the quantification of the products separated in the columns.

The MS and GC were calibrated for the main products observed from CO hydrogenation under our reaction conditions (methane, ethane, ethylene, propane, methanol, ethanol, acetaldehyde, methyl acetate and ethyl acetate). The mol % of each product in the gas feed was used to calculate the selectivity (S_i) for each product using equation (1):

$$S_i = \frac{M_i \times n_i}{\sum_i M_i \times n_i} \times 100\ \% \qquad (1)$$

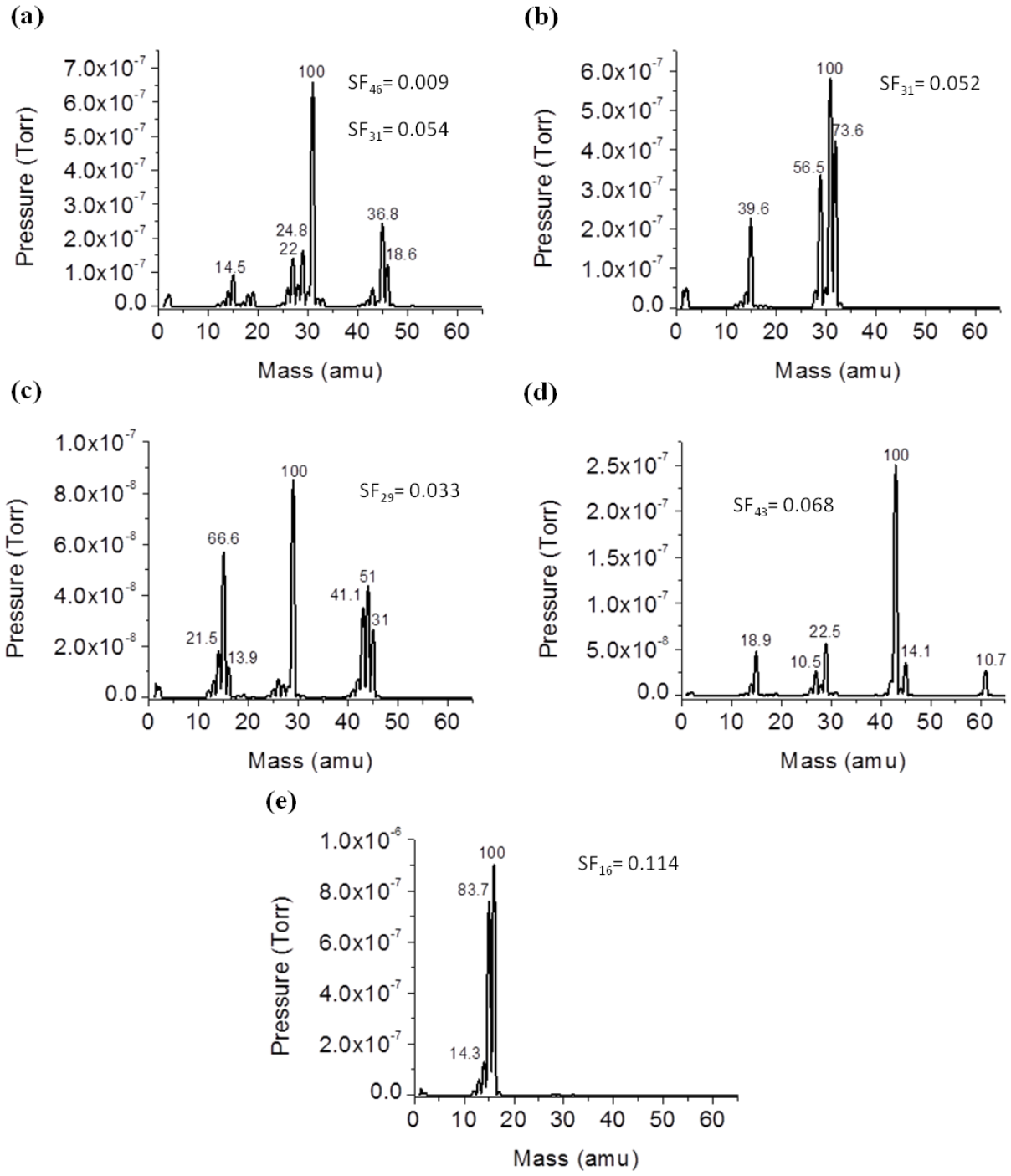

Figure 2.6: Mass spectra of all products discernible in the mass spectrometer along with ion fragment abundances and sensitivity factors used for product quantification: (a) ethanol, (b) methanol, (c) acetaldehyde, (d) ethyl acetate, (e) methane.

Where, M_i is the mol % of product *i* detected and n_i is the number of carbons in product *i*. This definition of selectivity follows the work of Haider, *et al*. who performed reactivity studies on similar catalyst systems.[6] As a measure of the overall activity, CO conversion (%) was also calculated for each catalyst via equation (2):

$$CO\ conversion = \frac{\sum_i M_i \times n_i}{M_{CO}} \times 100\ \% \qquad (2)$$

Where, M_{CO} is the mol % of CO detected in the gas feed.

Prior to reaction, the sample was reduced at 300°C under 9 mL/min H_2 flow at a pressure of 1 bar for 30 min (gas hourly space velocity (GHSV)= 0.028 $mL \cdot min^{-1} \cdot mm^{-3}$). After reduction, the sample was cooled to room temperature in 9 mL/min H_2 flow and the gas switched to a 4 mL/min H_2 flow + 2 mL/min CO flow at a pressure of 1 bar (GHSV= 0.019 $mL \cdot min^{-1} \cdot mm^{-3}$). The sample temperature was then raised to 240°C to simulate CO hydrogenation reaction conditions; this temperature was chosen after performing the reaction at a range of temperatures and determining the highest ethanol selectivity. A plot of ethanol production vs. reaction temperature for a 3 wt% Fe- 2 wt% Rh/TiO_2 catalysts collected by MS is shown in Figure 2.7.

2.4 *In situ* Structure Determination

The majority of this dissertation focuses on the *in situ* characterization of the structure of the Fe-promoted Rh catalysts using X-ray structural techniques at synchrotron radiation facilities. Synchrotron radiation (SR) provides high flux and high-energy photons caused by the acceleration of electrons around a vacuum ring guided by electromagnets. The x-rays generated from SR have a significantly higher flux and resolution than those from a laboratory source, which allows higher quality data from dilute samples (<10 wt%) to be acquired in significantly less time.

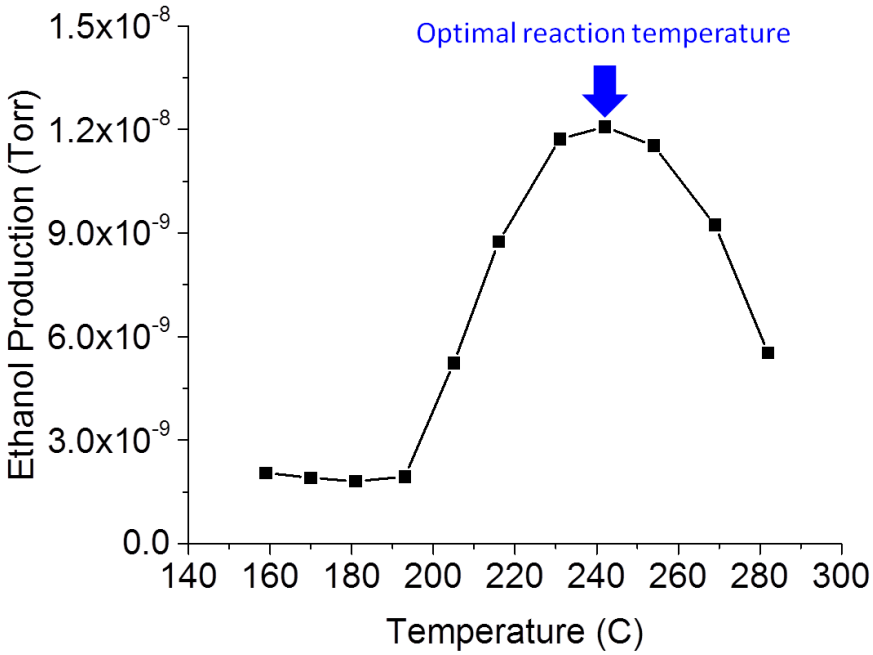

Figure 2.7: Ethanol production vs. reaction temperature for a 3 wt% Fe- 2 wt% Rh/TiO_2 catalysts during CO hydrogenation.

Additionally, the enhanced resolution from SR allows the observation of features in a spectrum, which ordinarily would be indistinguishable from one another using a laboratory source. For experiments, where long acquisition times, broad-spectrum features, and low sample concentrations make using a laboratory source unfeasible; SR is primarily used.

In order to determine the composition and accurately identify the phase of each component during different conditions (reducing and reaction conditions), XRD of the catalysts after reduction and during CO hydrogenation is performed. PDF/dPDF is used to qualitatively determine the local atomic structure of the active portions of the catalysts (Rh, Fe, and interactions of Rh/Fe with the support). Additionally, XAS was used to determine the electronic structure and local atomic structure of Fe–Rh/TiO_2 catalysts.

2.4.1 Powder X-ray Diffraction (XRD)

Since the discovery that crystals diffracted X-rays, much like gratings caused the diffraction of visible light; scientists have been attempting to resolve the structure of crystals by their characteristic diffraction patterns. The discovery by W. H. Bragg and W. L. Bragg, that X-ray diffraction was analogous to the reflection of light by a plane mirror further simplified the interpretation of diffraction patterns. The theory states that if an incident X-ray beam reflects off periodic planes in a crystal at an angle θ, the "reflected" beam will also be at the same angle θ from the planes. The diffraction pattern that is experimentally observed is the result of the constructive and destructive interference of the radiation scattered by the atoms ordered in the planes. However, because there are repeating parallel planes of atoms the reflections from successive planes cause an interference with each other, but constructive interference will only occur when the difference in path length between rays from successive planes is equal to a whole number of wavelengths. This process is illustrated in Figure 2.8.

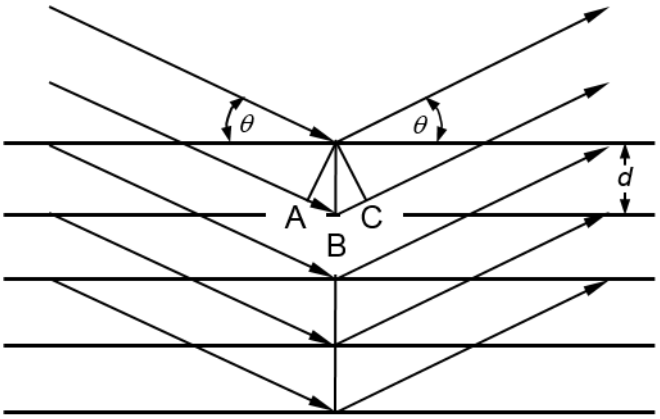

Figure 2.8: An illustration of X-ray “reflecting” off periodic crystal planes.

In the Figure, X-rays of wavelength λ are incident to crystal planes with a spacing of *d* at angle θ. The ray reflected off the second crystal plane has to travel AB + BC further than the 1st ray. According to theory, the two rays can only be in phase if:

$$AB + BC = n\lambda$$

where n is an integer. This can be translated as:

$$AB = BC = d \sin\theta$$

or

$$2d \sin\theta = n\lambda$$

This equation is formally known as Bragg's law, which simplified the interpretation of diffraction patterns and made the determination of the *d* spacing and lattice parameters of crystals easier.[17]

Bragg's law can be applied to powder X-ray diffraction, where multiple crystallites are randomly orientated in the X-ray beam. Of these crystallites, some are in orientations that satisfy Bragg's law and the beam is diffracted. The diffracted beams form a cone of half apex angle 2θ, so by scanning the diffractometer over a range of 2θ a powder diffraction pattern of intensity vs. 2θ can be generated. In single crystal diffraction, points from the lattice in the reciprocal-space are generated with a vector position of,

$$\boldsymbol{d}^* = h\boldsymbol{a}^* + k\boldsymbol{b}^* + l\boldsymbol{c}^*$$

where these points become spheres of radius $|\boldsymbol{d}^*|(=1/d)$ for a powder of randomly orientated crystallites.[17] The 2θ angle is determined by the position of the diffractometer. Each peak in

this pattern corresponds to a *d*(*hkl)* reflection of the crystallites illuminated by the X-rays. Alternatively, a 2D-detector positioned directly after the sample illuminated with X-rays can image the diffraction cones that are emitted from the sample. The 2θ position of each cone can be determined from the sample to detector distance, which is calibrated by the collection of diffraction from a known standard. Both diffraction setups are illustrated in Figure 2.9. The latter diffraction setup is used for synchrotron diffraction experiments, the method performed in this thesis.

There have been a number of significant advancements in powder XRD analysis, since its implementation. One is the compilation of powder diffraction databases, which allowed the fingerprinting of powder diffraction patterns to determine the identity of the illuminated polycrystalline material. The fitting of a powder diffraction pattern to a theoretical model was developed by Hugo M. Rietveld and was coined the term Rietveld refinement.[18] During this refinement, a powder diffraction pattern is generated from a known structural model, which is believed to be the identity of the material that powder diffraction was performed on. The calculated intensity of the diffraction pattern from the structural model is given by[17],

$$y_{cal}(x_i) = \sum_j I_j G_j \Phi(x_i - x_j) + b(x_i)$$

where G_j is a preferred-orientation function, and I_j gives the integrated intensity of the *j*th reflection. I_j contains information on the scale factor for the intensity as well as the structure factor, which summarizes the atomic coordinates, occupancies, *hkl* indices, scattering factor, nuclear scattering lengths, and temperature factors. Additionally, a non-structural model is used to correct for instrumental functions and effects of the sample's microstructure.

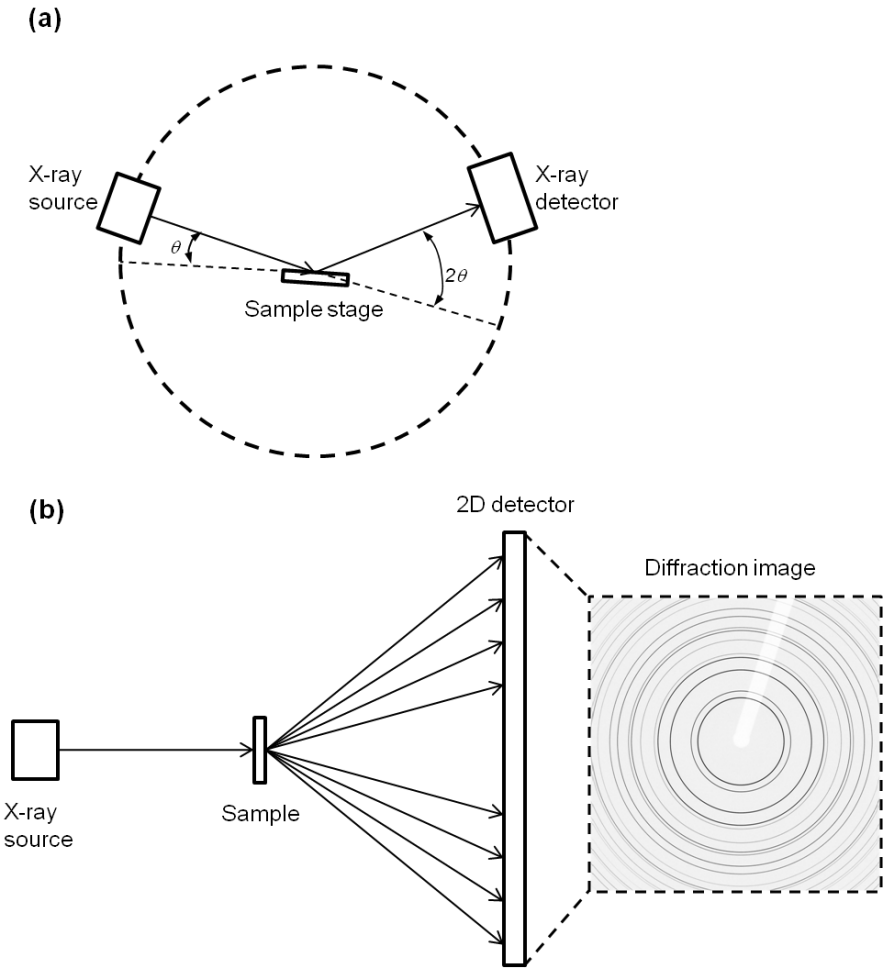

Figure 2.9: Depiction of powder diffraction experimental setups: (a) common powder diffractometer setup with moving X-ray detector (b) transmission mode setup used at synchrotron facilities with diffraction pattern of a CeO_2 standard.

These include the characteristics of the experimental setup, e.g. X-ray source and detector resolution, and specific deviations from the structural model, e.g. nano-confinement and particle shape. The experimental diffraction pattern is modeled by varying the parameters of the structural and non-structural model until the calculated diffraction pattern matches closely with the experimental pattern. The fitting parameters include lattice constants, atomic coordinates, atom potentials, scale factor, phase fractions, and peak profile functions. This allows the user to solve a crystal structure from a powder diffraction pattern, which enhanced the analysis of powder diffraction data to a massive extent. In addition to the fit, a residual value (R value) is given for the fit to the model, which allows for a quantitative judgment of the fit in relation to other fits to the same data. A fit is considered to be complete when the R value approaches a minimum and the errors given for each parameter are reasonable, in comparison to the values determined by the fit. Conspicuously large peak widths or extreme deviations from the chosen structural model suggest that the wrong model was chosen. A completed fit will contain quantitative information about the phase composition, cell lattice constants, atomic coordinates, atom potentials, and crystallite size. The structural models can be chosen from knowledge of the sample synthesis and expected product, conditions of sample during the collection of powder diffractions, and even fingerprint analyses against a database of powder diffraction patterns.

2.4.2 Pair Distribution Function (PDF)

A Pair distribution function (PDF) shows the probability of finding atoms at a given distance, r, from the scattering atom.[19] PDF analysis utilizes the scattering intensities obtained in XRD, $I_m(Q)$, and applies additive and multiplicative corrections to obtain the coherent scattering intensities:

$$I_m(Q) = a(Q)I_c(Q) + b(Q)$$

where $I_c(Q)$ is the coherent scattering intensity, a(Q) is the multiplicative corrections (such as, self-absorption and X-ray beam polarization), and b(Q) is the additive corrections (such as Compton and background scattering from the container).[20] A structure function, S(Q) can be obtained from $I_c(Q)$:

$$S(Q) = \frac{I_C(Q) - \langle f(Q)^2 \rangle + \langle f(Q) \rangle^2}{\langle f(Q) \rangle^2}$$

where *f*(Q) is the atomic scattering factor and the angle brackets represent an average over all the atom types in the sample.[20] A sine Fourier transform of S(Q) yields the PDF or G(r):

$$G(r) = (2/\pi) \int_{Q_{min}}^{Q_{max}} Q[S(Q) - 1] \sin Qr \, dQ = (2/\pi) \int_{Q_{min}}^{Q_{max}} F(Q) \sin Qr \, dQ$$

where $F(Q) = Q\,[S(Q) - 1]$ is the reduced structure function.[20]

In general, PDF can give information about the local atomic structure on length scales beyond that of the unit cell, which can be obtained by Rietveld refinements of XRD. Additionally, PDF of amorphous materials is possible, and so the local atomic structure of these materials can be determined as well. A disadvantage of PDF analysis is that it is not energy specific, meaning that the local atomic structure of all elements in the sample is displayed simultaneously. For complex samples, ≥ 2 compounds, peak assignment can prove difficult. This issue is exacerbated when there are minor components whose contribution to the overall intensity is ≤ 10 %. Fits to samples such as these are largely inaccurate, because a reasonable fit is possible even with the incorrect models for the minor phases since the fit is not sensitive to changes induced by the minor phases.. Fortunately, qualitative data can still be obtained from the PDF of complex materials by utilizing dPDF, which subtracts the PDF of the major phase from

the complete PDF to obtain a dPDF of only the minor phases. The complex samples presented in this thesis consist of Fe–promoted Rh nanoparticles supported on TiO_2 or CeO_2. PDF is collected on the supported particles and the bare supports under identical conditions. The PDF of the bare support can then be subtracted from the PDF of the supported particles yielding the dPDF of Fe-promoted Rh alone. However, this subtraction introduces features that are caused by the changes in the support from the deposition of the metals, which are difficult to model. For this reason, fitting dPDF against a model is not reasonable, and so dPDF data is generally interpreted in a qualitative fashion. The peaks in dPDF can be assigned both from the phases identified in Rietveld refinements of XRD and from the knowledge of the elemental composition combined with the reaction conditions, (i. e. Rh in a reducing atmosphere should lead to Rh metal).

2.4.3 X-ray Absorption Spectroscopy (XAS)

X-ray absorption spectroscopy is the general term for a synchrotron based technique that encompasses two distinct techniques: X-ray absorption near edge structure (XANES) and extended X-ray absorption fine structure (EXAFS). In general, XAS uses the tunable energy from a synchrotron source to excite core level electrons of an element where the energy is at or above the absorption edge of that element. This absorption can be quantified by comparing the intensity of the incident X-rays with the transmitted X-rays, measuring the fluorescence emitted from an outer shell electron filling the hole created by the photoelectron, or by measuring the electrons ejected by the filling of the hole left behind (Auger electrons). The ejected core level electron, or photoelectron, emits as a wave and scatters off neighboring atoms before it returns to the absorbing atom, where it can interact with the outgoing wave constructively or destructively. Constructive interference indicates a presence of electron density at the absorbing atom, which means that there is a greater possibility that the atom will absorb the photon, rather than allowing

it to pass through. Changing the X-ray energy, in turn, changes the kinetic energy of the photoelectron wave, which affects the absorption probability of a photon by an atom. Since the photoelectron wave is sinusoidal, the interference pattern is as well. Therefore, the change in photoelectron kinetic energy results in oscillations on absorption intensity in the absorption spectrum. The spacing of the oscillations is dependent on the distance between the absorbing and scattering atoms. Consequently, characterization of these oscillations provides information about the local atomic environment of the absorbing atoms. A schematic of this process is shown in Figure 2.10.

A typical XAS spectrum has three distinct regions: The edge region, XANES region, and EXAFS region. The last two regions are where the individual techniques are derived. The edge region is where the element begins to absorb photons and is marked by a characteristic sharp increase of absorption. The absorption edge, which is generally identified by the energy at which the change in absorption is the highest, is the energy at which the core level electron is excited. Therefore, the pre-edge features and edge position is dependent on the electronic environment of the absorbing atoms, e.g. oxidation state. The XANES region, which includes the edge region, has characteristic features on or near the edge that can identify specific phases of the element studied. The 3rd region is the EXAFS region, where periodic oscillations occur that correspond to the different atomic environments.

Various forms of data analysis are possible with XAS data. The majority of these methods require previous knowledge of the material. A visual examination of the spectrum in many cases can limit the possible phases, e.g. large ‘whiteline’ peaks appearing just after the absorption edge typically identify oxide phases, which is caused by the $2p_{3/2}$ to 5d excitation. The whiteline is a direct measure of the 5d-unoccupied states.

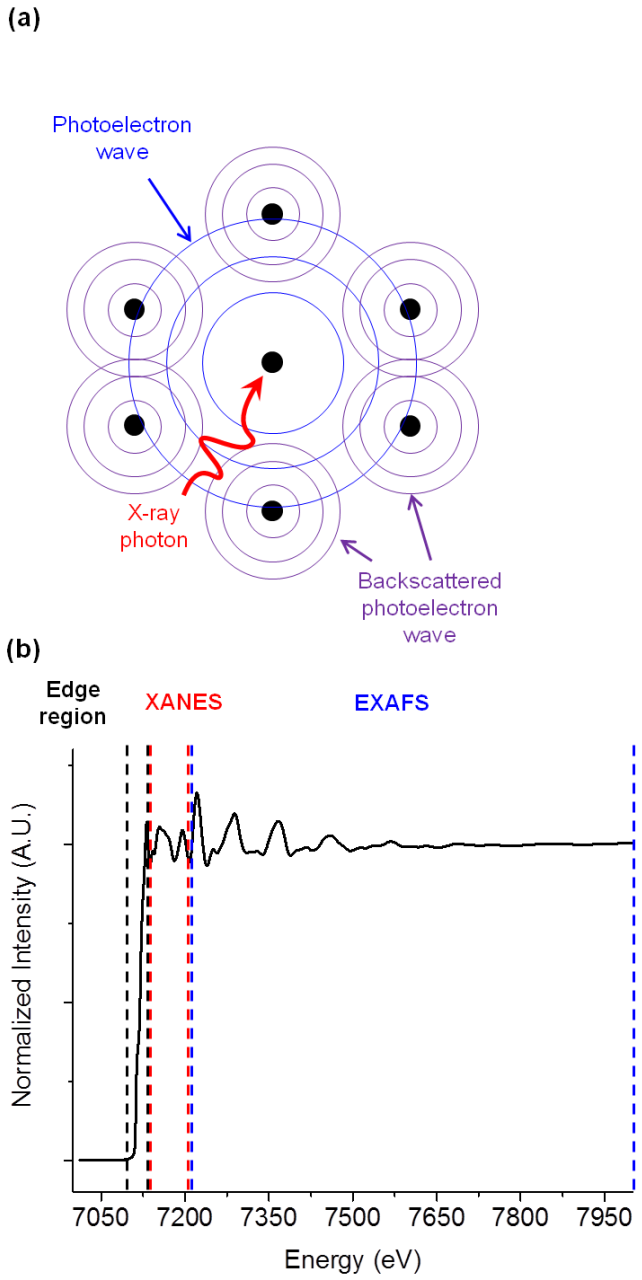

Figure 2.10: Depiction of X-ray absorption process and resulting XAS spectrum: (a) absorption of X-ray photon causing the ejection a photoelectron that scatters off neighboring atoms and interacts with the outgoing photoelectron wave (b) XAS spectrum of Fe metal foil labeling the regions of the spectrum.

Therefore, oxidized group VIII transition metals exhibit this significant feature due to the unoccupied 5d orbitals. If a list of possible phases can be generated, then the XANES region can be analyzed by a fingerprinting method where the spectra collected from standards can be linearly combined; this technique is commonly referred to as linear combination analysis (LCA).

LCA can be a powerful tool for the identification of phases, as well as the quantification of the amounts of each phase in the spectra, but unfortunately requires the standard spectra for all the possible constituents for it to be useful. If the standard spectra of all possible phases are not available, then a more general analysis can be employed called principle component analysis (PCA). PCA can combine the spectra of various materials collected on the same instrument and form variables, which can determine the similarity of a new spectrum to the database already established. This is especially useful for relatively unknown samples, where a comparison to previously collected spectra is desired. This analysis method is not useful when a detailed structural analysis is required.

The analysis method most commonly used, and the method used in this work, is the 'fitting' method. In this method, the spectrum collected is compared to a theoretical model. However, before data analysis is performed, the spectrum needs further processing. For this method of analysis, the EXAFS region is used, but the background needs to be subtracted to account for the edge jump and the major modulations in intensity from the XANES region. The background subtraction generates a χ(E), which is converted to χ(k) using the following equation:

$$k = \frac{1}{\hbar}\sqrt{2m_e(E - E_0)}$$

Where E_0 is the energy necessary to eject the photoelectron from the core shell, m_e is the mass of an electron, and ħ is Planck's constant. In order to separate the individual contributions of each scattering pair from the χ(k), a Fourier transform (FT) is done. It's important to note that the FT is **not** a radial distribution, although it is proportional to one. This FT is what is used to fit against a theoretical model. By taking the structural parameters of the theoretical model and inputting them into the 'EXAFS' Equation, a FT from the theoretical model can be generated to compare to the experimental FT:

$$\chi(k) = S_0^2 \sum_i N_i \frac{f_i(k)}{kD_i^2} e^{-\frac{2D_i}{\lambda(k)}} e^{-2k^2\sigma_i^2} \sin(2kD_i + \delta_i(k))$$

Where, S_0^2 is the amplitude reduction factor that models the incomplete overlap of the initial state before the photoelectron is ejected and the final state when it returns. N_i is the degeneracy or number of scattering pairs identical to the current one, $f_i(k)$ is a proportionality constant that is proportional to the possibility of scattering elastically off of the atom, D_i is half the total distance of the scattering path, σ_i^2 is the mean square radial displacement factor that models thermal and static disorder, and $\delta_i(k)$ is the phase shift that the scattering atom induces on the photoelectron. By allowing these parameters from the model in the EXAFS equation to vary, a FT that is comparable to the experimental FT can be generated. It would then be assumed that the structural parameters of the model that was fit to the experimental data are identical to the sample measured. This method of analysis provides the most specific information about the structure of the material and is therefore the most commonly used analysis method of XAS data, which is also the analysis method used in this work.

2.4.4 Synchrotron Experimental Setup

The structures of the Fe-Rh/TiO_2(CeO_2) catalysts under different conditions were investigated by XRD and PDF at the X7B beamline at the National Synchrotron Light Source (NSLS) operating at a wavelength of 0.3196 Å and at the 11-ID-B beamline of the Advanced Photon Source (APS) operating at a wavelength of 0.2114 Å. The powder diffraction pattern was collected with a Perkin Elmer amorphous silicon 2-D detector. The detector distance was changed from 400 mm for XRD to 180 mm for PDF measurements, since high quality XRD measurements require long detector distances to increase the resolution of individual peaks, while PDF measurements need short detector distances to collect the total scattering pattern, which is observed out to high 2θ or Q. The detector position was calibrated by measuring the diffraction from either a sodium hexaboride standard or cerium dioxide standard at both detector positions. XRD and PDF data were collected on the as-synthesized samples and after reduction at 300°C for 30 min. under 9 mL/min H_2 flow at a pressure of 2 bar (GHSV= 0.191 $mL \cdot min^{-1} \cdot mm^{-3}$). After cooling to room temperature, XRD and PDF measurements were made on the reduced catalysts and then under CO hydrogenation conditions of 4 mL/min H_2 + 2 mL/min CO flow at 240 °C at a total pressure of 2 bar (GHSV= 0.127 $mL \cdot min^{-1} \cdot mm^{-3}$). XRD and PDF data were also collected for the bare support under identical conditions to compare with loaded catalysts for analysis by dPDF where only the contributions of Fe and Rh are observed. A picture of the synchrotron experimental setup for XRD/PDF and XAS is shown in Figure 2.11.

The XAS study of micelle templated Fe_xRh_y/TiO_2 was performed at beamline 5−BM−D of the APS. Ionization chambers were used to measure the X−ray intensity before and after in the same reactor cell used for the XRD/PDF studies. A 4−channel Si Vortex detector that was positioned orthogonal to the reactor cell measured the fluorescence signal from the sample.

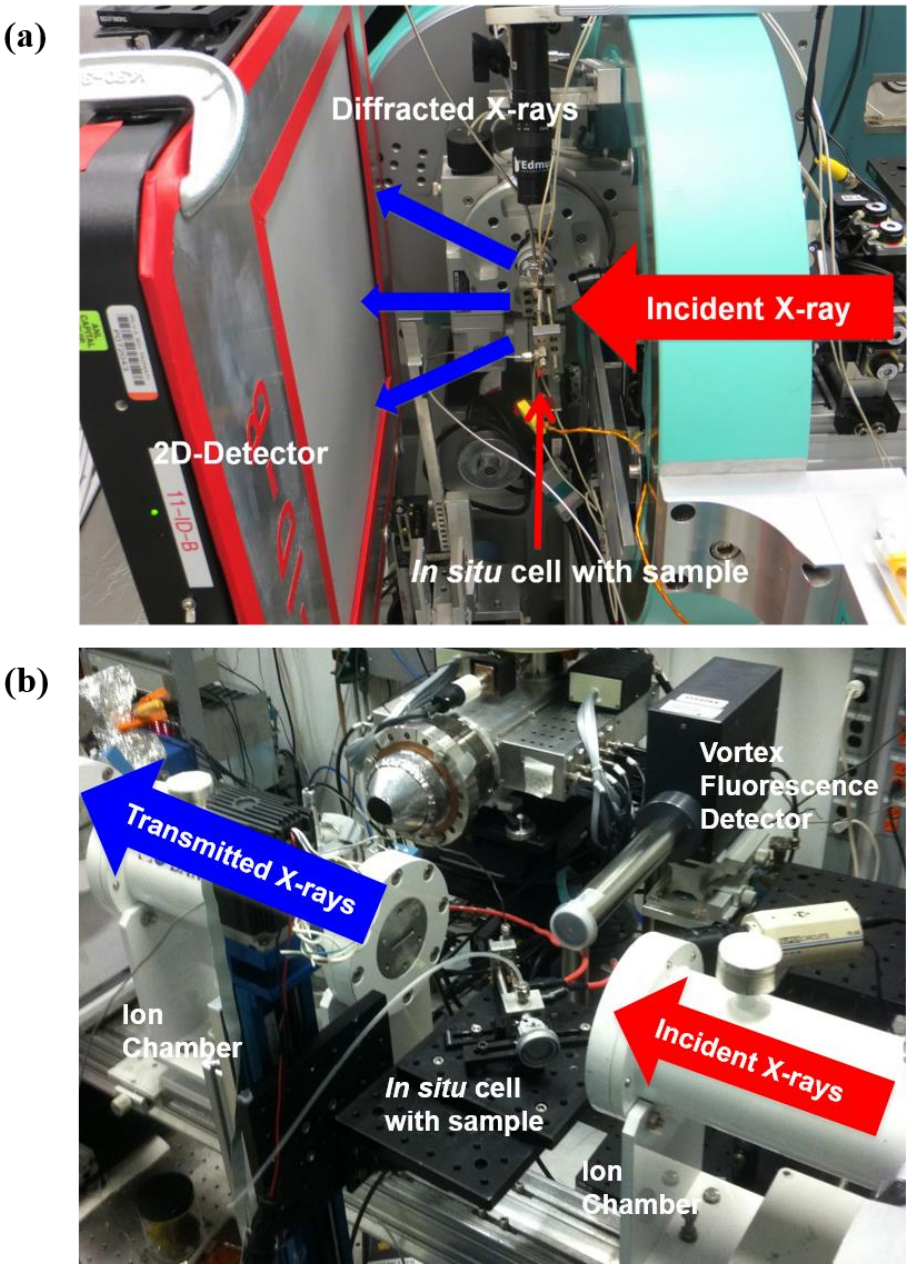

Figure 2.11: Image of synchrotron experimental setup: (a) *in situ* cell during XRD/PDF study (b) *in situ* cell during XAS study. (Images taken at APS 11-ID-B and 5-BM-D)

The reactor cell was also tilted at a 45° angle to maximize the cross−section of X−ray absorption in the sample and fluorescence hitting the detector. The standard metal foil of the element measured was located immediately after the transmission ionization chamber and an ionization chamber is positioned behind it to allow the measurement of transmission for the reference, which is used as an internal calibration standard. The sample is loaded into a 1/8 ″ OD kapton capillary tube, plugged on both ends with glass wool and loaded into the reactor cell. Sample heating and temperature measurement is identical to that of the XRD/PDF experiment. The sample is reduced at 300°C under 9 mL/min H_2 flow at a pressure of 1 bar for 30 min (gas hourly space velocity (GHSV)= 0.028 $mL \cdot min^{-1} \cdot mm^{-3}$) and the EXAFS was collected on the Rh and Fe K-edge after cooling to room temperature. To simulate CO hydrogenation reaction conditions, the reactant gas was switched to a 4 mL/min H_2 flow + 2 mL/min CO flow at a pressure of 1 bar (GHSV= 0.019 $mL \cdot min^{-1} \cdot mm^{-3}$) and the temperature was increased to 300 °C. The EXAFS of the Rh K-edge was then measured.

2.4.4 Data Analysis

The XRD and PDF 2-D diffraction images were integrated into 1-D "2θ scans" using the Fit2D software.[21] The Rietveld refinement of XRD data was performed with the EXPGUI-GSAS software package.[22, 23] The analysis was completed by fitting the sample diffraction to an appropriate model where the lattice constants, scale factor, peak profile functions, and atomic potentials were varied to produce a simulated diffraction pattern nearly identical to the experimental XRD data. The models were chosen based upon knowledge of synthesis, reaction conditions, and phases previously identified in similar studies, i.e., Rh metal, Fe metal, FeRh alloys (FeRh and Fe0.7Rh0.3), FeO, Fe_2O_3, Fe_3C, Fe_2C, Fe_5C_2, CeO_2, anatase TiO_2, and rutile

TiO_2.[24-37] A complete refinement provides information about phase quantification, lattice constants, and particle size.

The PDF data was processed with the software package pdfgetX3 which provides a Fourier transform of the scattering function obtained from the diffraction pattern.[20] Ordinarily, PDF can be fit against a model to quantifiably determine the particle size, coordination number, and order. For the catalysts studied in this work, the Fe and Rh components of interest are less than 10 wt % of the major phase, i.e., the TiO_2 or CeO_2 support, which makes fits to the PDF data insensitive to structural parameters involving the Fe and Rh components. The dPDF, where the scattering signal from the bare TiO_2/CeO_2 support is subtracted from that of the metal loaded catalyst under the same conditions, allows the contributions from the minor phases to be observed more clearly. However, dPDF data includes changes in support structure associated with the deposition of Fe and Rh that cannot be readily accounted for in structural models. Here, the dPDF data is used to qualitatively analyze the first shell atomic distances and coordination of the Fe and Rh components utilizing the phase information obtained from the XRD refinement and the phases identified in previous studies.[6, 9, 11, 38]

The analysis of the XAS data is performed by the IFEFFIT package consisting of Athena, Artemis, and Hephaestus software programs.[39] The XAS data is normalized, background subtracted, converted to $\chi(k)$, and subsequently Fourier transformed using the Athena software. Models identical to that used in XRD refinement are fit against the experimental FT using the Artemis software.

Chapter 3. Diblock Copolymer Micelle Templating of Fe-promoted Rh

3.1 Introduction

Heterogeneous catalysis has grown to have an immense impact on the global economy, considering that over 90 % of industrial chemical processes involve the use of catalysts.[40] Catalysts have been used in the production of essential chemicals like ammonia synthesis from the Haber process, down to pollution mitigation such as the reduction of CO and NO_x gas in the catalytic converters of automobiles. Most aspects of our daily lives are improved by the processes that are possible due to heterogeneous catalysis. A specific area of catalysis that has grown and received much attention in the past few decades is nanocatalysis. It has been found that when materials are confined to sizes <10 nm, their catalytic activity and selectivity is enhanced when compared to their bulk counterparts.[40] A classic example is that found by Valden *et al.*, where they established a correlation between a metal-to-semiconductor transition found when decreasing the particle diameter of Au supported on TiO_2, to an enhancement of CO oxidation activity.[41] Other features caused by nano-confinement that lead to enhanced reactivity include low coordinated sites, increase nanoparticle-support interactions, and excess electronic charge localized on the nanoparticles.[40]

Since the discovery of the 'nano–effect', research has focused on improving catalyst designs by attempting to control some of the important parameters that affect catalytic activity and selectivity: particle size, oxidation state, composition, support. A deposition method capable of controlling these parameters independently could be used to assist in the studies that attempt to elucidate key structural aspects of catalysts as a function of these parameters. The diblock

copolymer reverse micelle templating approach for deposition of nanoparticles, is a method which gives control over the approximate size of the particles, inter-particle spacing, and individual particle composition. The approach takes advantage of the self assembling nature of diblock copolymers to deposit ordered arrays of metal nanoparticles on planar substrates. One of the first efforts at depositing metal nanoparticles via a polymer template was by Spatz *et al.*, who deposited Au nanoparticles from a polymer template constructed of poly(styrene)-block-poly(2-vinylpyridine) (PS-b-P2VP) micelles.[15] They report that upon dissolution in toluene, this diblock copolymer forms spherical micelle structures that can serve as a compartment for transition metal salts. When these micelles are deposited onto a planar substrate, they assemble into a pseudo-hexagonal array. This polymer in this micelle film is cleaned via oxygen plasma to reveal ordered metal or metal oxide nanoparticle in the same array of the micelle that preceded them. Figure 3.1 shows an SEM micrograph of Au/Si(100) prepared via this approach. This process was later expanded upon by Cuenya *et al.* and Glass *et al.*, where it was used as a size-selected deposition method that controls the approximate size of the particle diameter.[13, 14] They deposited Au nanoparticles of difference particle diameters via this approach by keeping a constant Au/2VP ratio, while changing the MW of the P2VP block. The approach also has the ability to deposit numerous metals (Pt, Fe, Ni, Cu, Pd, Ru) and bi-metallic alloys (PtFe, FeAu, PtPd, PtRu) on different supports, including powdered nanoparticulate metal oxides.[42-47] Additionally, this approach fabricates particles which are resistant to sintering during high temperature reductions and reactions.[42, 48-50]

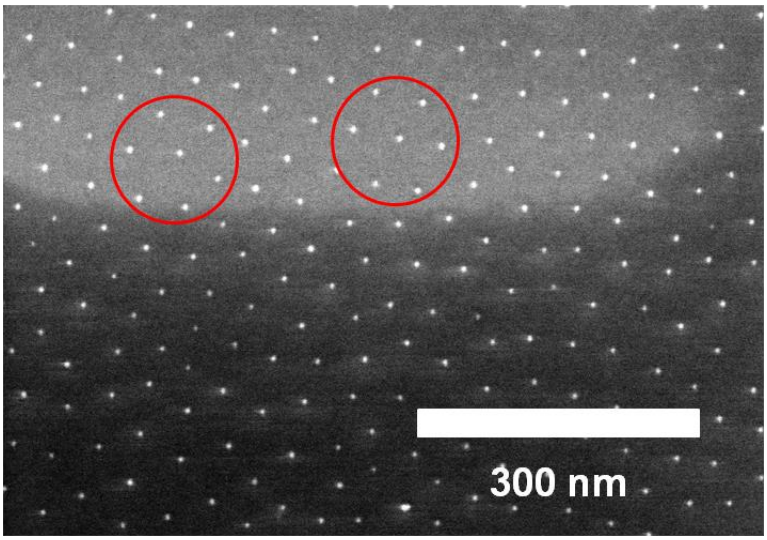

Figure 3.1: SEM micrograph of Au nanoparticles synthesized via the diblock copolymer reverse micelle template approach with pseudo-hexagonal pattern circled: PS(53400)-b-P2VP(8800) used as template.

This chapter focuses on the deposition of Rh–Fe bimetallic catalysts via the diblock copolymer reverse micelle approach on Si (100) and powdered TiO_2 supports, for use towards the catalytic hydrogenation of CO to ethanol. The morphology of these catalysts was determined collectively by AFM, SEM, and TEM. The electronic and local atomic structure of the reduced catalysts and catalysts under CO hydrogenation reaction conditions were determined by XANES and EXAFS, respectively.

3.2 Experimental Methods

A detailed version of the deposition method is given in section 2.1.1, but is briefly described here. Two diblock copolymers (PS_{37000}-b-$P4VP_{16000}$ and PS_{40000}-b-$P4VP_{5600}$) were used to form micelle templates for control over the size of nanoparticles. A 0.2 wt% polymer solution in toluene was stirred at 80 °C for 24 hours to form spherical micelles suspended in toluene. Rhodium (II) acetate dimer and iron (III) chloride hexahydrate were added to the micelle solution, at room temperature, in varying ratios to control the composition of the deposited nanoparticles. The loaded micelle solution was filtered through a 100 nm pore sized filter to eliminate undissolved precursor not associated to the cores of the micelles and subsequently spin cast onto Si(100) single crystal subtrates to form a ML of micelles or nanoparticulate TiO_2 powder was added to the micelle solution and dried at 120 °C overnight. The loaded micelles deposited on Si(100) were cleaned via oxygen plasma (300 mTorr, 110W, 5 min), while those deposited on nanoparticulate TiO_2 powder were calcined in air at 500°C for 4 hours.

The morphology of catalysts supported on Si(100) are studied by AFM, using a Veeco Multimode V scanning probe microscopy with an AFM head in tapping mode, and SEM, using a

Hitachi S-4800 HRSEM at an acceleration voltage of 5 kV. HRTEM of particles deposited on Si(100) and TiO_2 powder are obtained on a JEOL 2100F HRTEM operating at an acceleration voltage of 200 kV.

The XANES and EXAFS are measured on reduced catalysts and catalysts under CO hydrogenation conditions at beamline 5-BM-D of the APS. The powdered catalysts were loaded into the reactor cell, described in section 2.3 and 2.4, where the catalysts were placed in a 1/8 ″ OD kapton capillary plugged with glass wool before the assembling the reactor cell. The catalysts were reduced at 300°C under 9 mL/min H_2 flow at a pressure of 1 bar for 30 min (gas hourly space velocity (GHSV)= 0.028 $mL \cdot min^{-1} \cdot mm^{-3}$) and cooled to room temperature before Rh and Fe K-edge EXAFS data is collected. The catalysts were then brought to CO hydrogenation reaction conditions, 300°C under 4 mL/min H_2 flow + 2 mL/min CO flow at a pressure of 1 bar (GHSV= 0.019 $mL \cdot min^{-1} \cdot mm^{-3}$). The Rh K-edge EXAFS data was then collected under these conditions.

3.3 Results and Discussion

3.3.1 Fe_xRh_y/Si(100)

Size–selected Rh and Rh–Fe nanoparticles deposited on Si(100) were fabricated using the reverse micelle templates. The ability to control both the particle size via controlling the MW of the P4VP block of the diblock copolymer, PS–b–P4VP, was demonstrated on both the monometallic Rh nanoparticles and the bimetallic Rh–Fe nanoparticles. Figure 3.2 shows the AFM, SEM, and size distribution of Rh/Si(100) nanoparticles deposited from the polymer micelle templates using two different diblock copolymers with P4VP units of 5600 mol and 16000 mol.

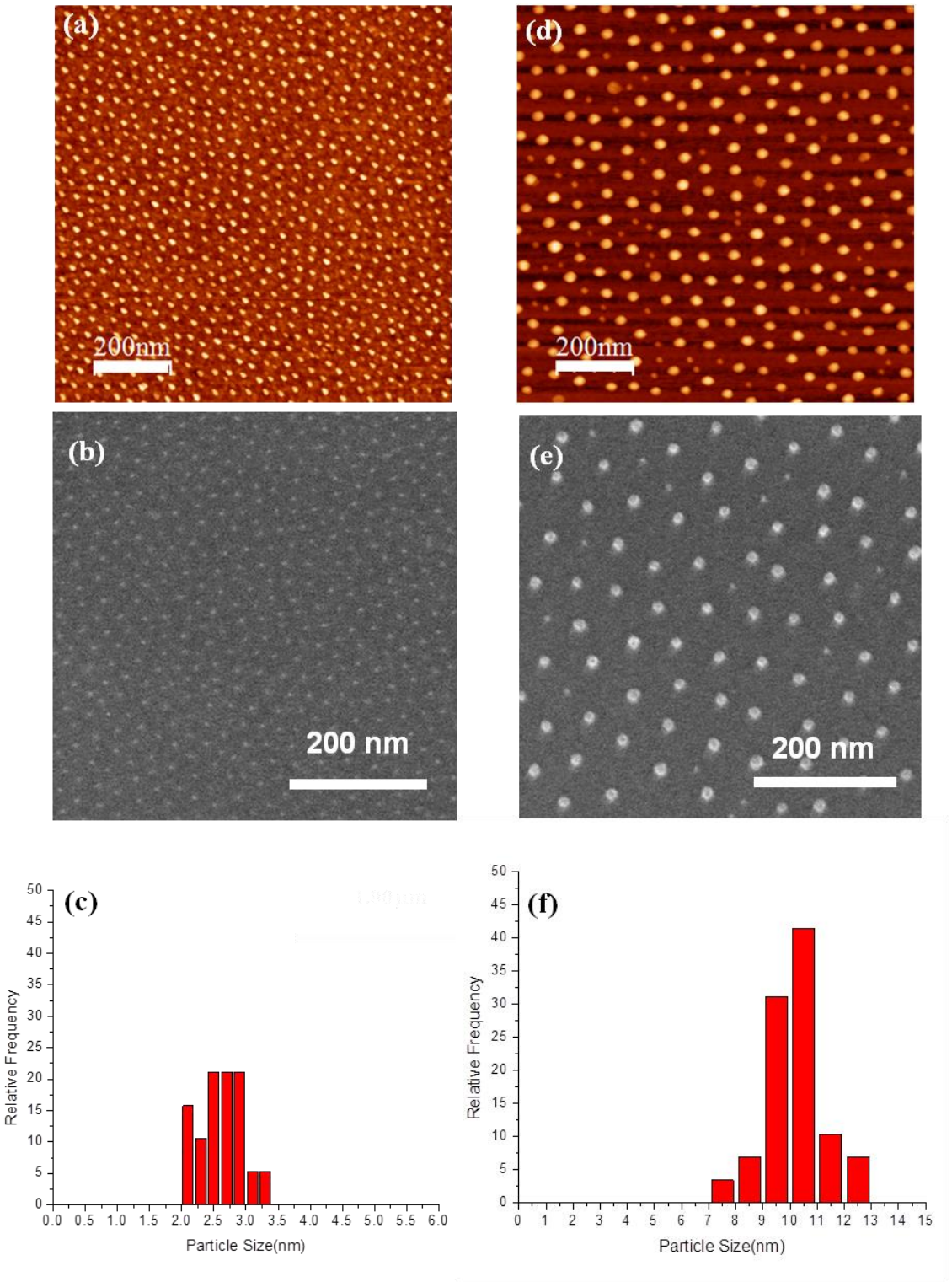

Figure 3.2: AFM (a, d), SEM (b, e), and size distribution (c, f) of Rh/Si(100) using two different MW polymers: PS_{40000}−b−$P4VP_{5600}$ (a−c) and PS_{37000}−b−$P4VP_{16000}$ (d−f).

Figure 3.3 shows the AFM, SEM and size distribution of $Fe_{0.5}Rh_{0.5}$/Si(100) bimetallic nanoparticles formed from templates of the same diblock copolymers used for the Rh nanoparticles. These results demonstrate this method's ability to control the approximate particle size by varying the MW of the P4VP block in the polymer. In both Figures (3.1 and 3.2) the effect of changing the MW of the P4VP block is the same; the particle size is increased by almost 5 fold. However, the size distribution for either is not as narrow as would be needed for size dependent studies, especially for smaller particles. In addition, nanoparticles made from PS_{37000}−b−$P4VP_{16000}$ appear to have a bimodal distribution in particle size, which becomes more apparent in the bimetallic nanoparticles. The micelle templating method was also used to control the ratio of Rh to Fe. This was done by changing the ratio of the respective precursors to each other to achieve the desired ratio of Rh/Fe in the catalyst.

Figure 3.4 shows AFM and TEM (along with their respective size distributions) for Rh−Fe bimetallic nanoparticles with an Rh/Fe ratio ranging from 3 to 0.2. Overall, each sample has comparable size distributions and morphologies regardless of the Rh/Fe ratio. This shows that the sample morphology is preserved when altering the nanoparticle composition with the micelle template approach.

3.3.2 Fe_xRh_y/TiO_2

The same micellar solutions that were used to deposit the Rh and Fe_xRh_y nanoparticles on Si(100) were used to deposit these metals on nanoparticulate TiO_2. The Rh/Fe ratio of bimetallic nanoparticles studied on TiO_2 ranged from 3 to 1. The morphology and composition were investigated via TEM and EDS, respectively.

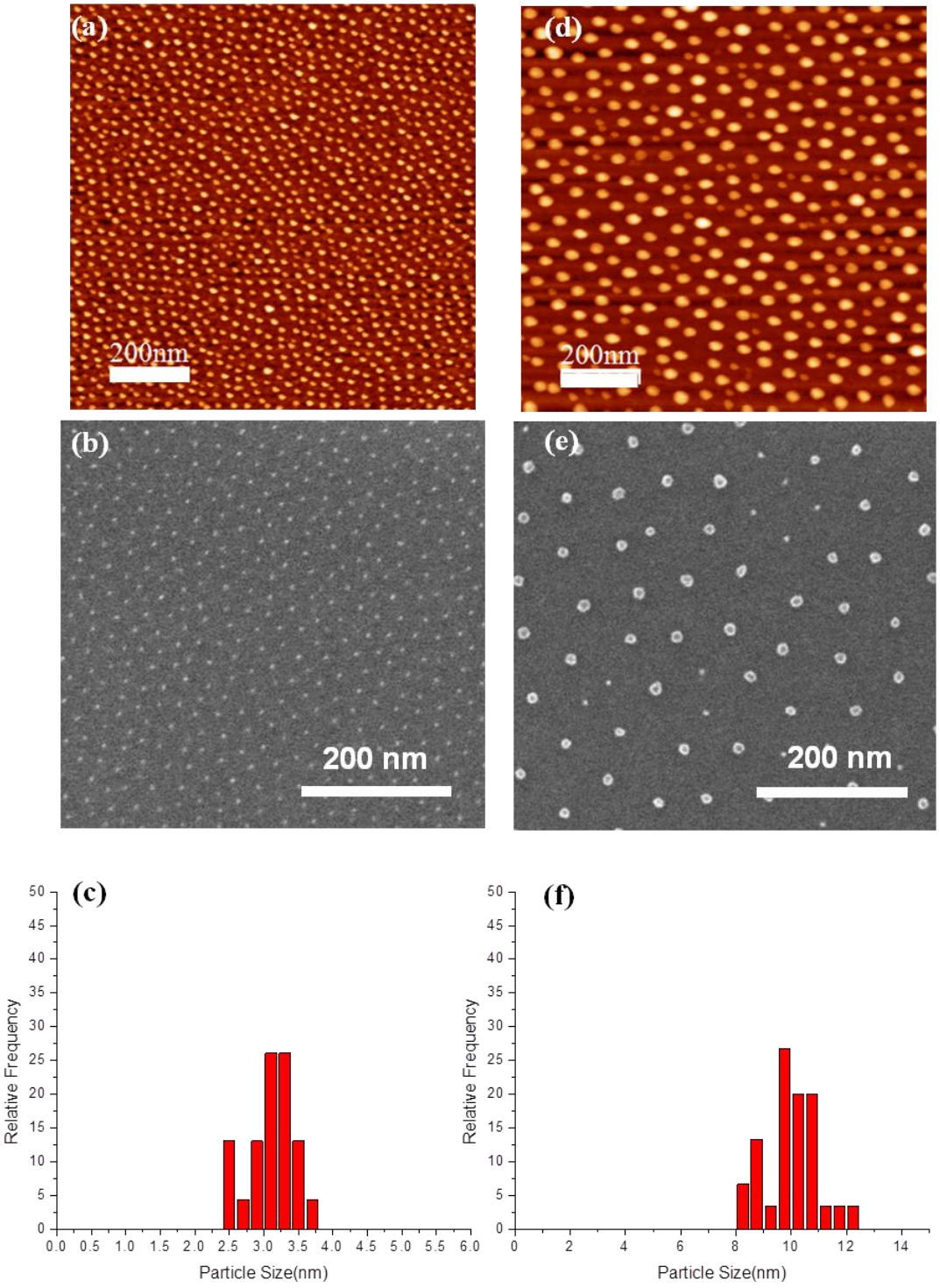

Figure 3.3: AFM (a, d), SEM (b, e), and size distribution (c, f) of $Fe_{0.5}Rh_{0.5}$/Si(100) using two different MW polymers: PS_{40000}−b−$P4VP_{5600}$ (a−c) and PS_{37000}−b−$P4VP_{16000}$ (d−f).

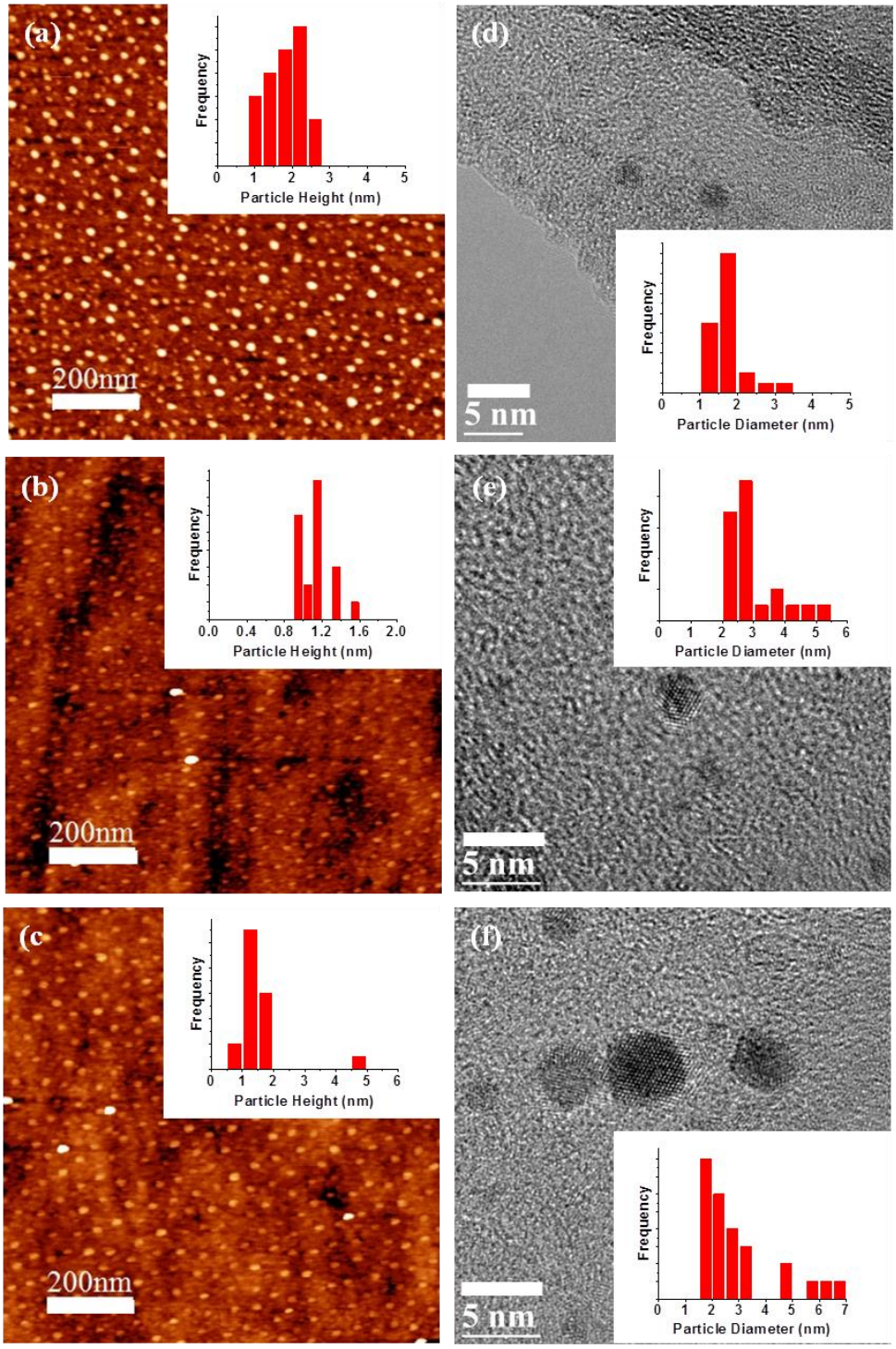

Figure 3.4: AFM (a–c) and TEM (d–f) with inset size distributions of Fe_xRh_y/Si(100) over varying compositions: $Fe_{0.25}Rh_{0.75}$/Si(100) (a, d), $Fe_{0.5}Rh_{0.5}$/Si(100) (b, e), $Fe_{0.75}Rh_{0.25}$/Si(100) (c, f).

Figure 3.5 shows the TEM images of the Fe-Rh/TiO_2 samples along with size distributions (inset). A major goal of the performing TEM on the Fe-Rh/TiO_2 catalysts, was to determine where Fe was located in relation to Rh, i. e., was a homogeneous alloy formed, did phase segregation occur resulting in a core-shell morphology, or was Fe and Rh not present in the same particle. Most of the samples had no noticeable phase segregation of Rh and Fe, but $Rh_{0.5}Fe_{0.5}/TiO_2$ may have core–shell morphology with Rh at the core and Fe as a shell. Unfortunately, a homogeneous alloy could neither be confirmed nor disproved via HRTEM. Likewise, individual Rh and Fe particles could not be confirmed. Overall, the particle size distribution is not as narrow as was originally expected for this approach. The standard deviation of the average particle size is at least 1/3 of the average size, which is not ideal for any size–selected study or studies which require specific particle size. Table 3.1 shows the results of the EDS analysis, which indicate the approximate wt% and atomic% of each sample characterized via TEM. The results indicate that the actual composition of the nanoparticles matches closely with the as-synthesized composition.

3.3.3 Electronic and atomic structure determination of Fe_xRh_y/TiO_2

The electronic character is qualitatively analyzed by comparing the XANES of the Fe-Rh bimetallic catalysts to the XANES of Fe and Rh metal and oxide standards (Fe, Rh, Fe_2O_3, FeO, Fe_3O_4, Rh_2O_3). Figure 3.6 shows the normalized XANES spectra and 1st derivative of the normalized edge region of the reduced bimetallic catalysts along with the spectra of standards for both the Fe and Rh K-edges.

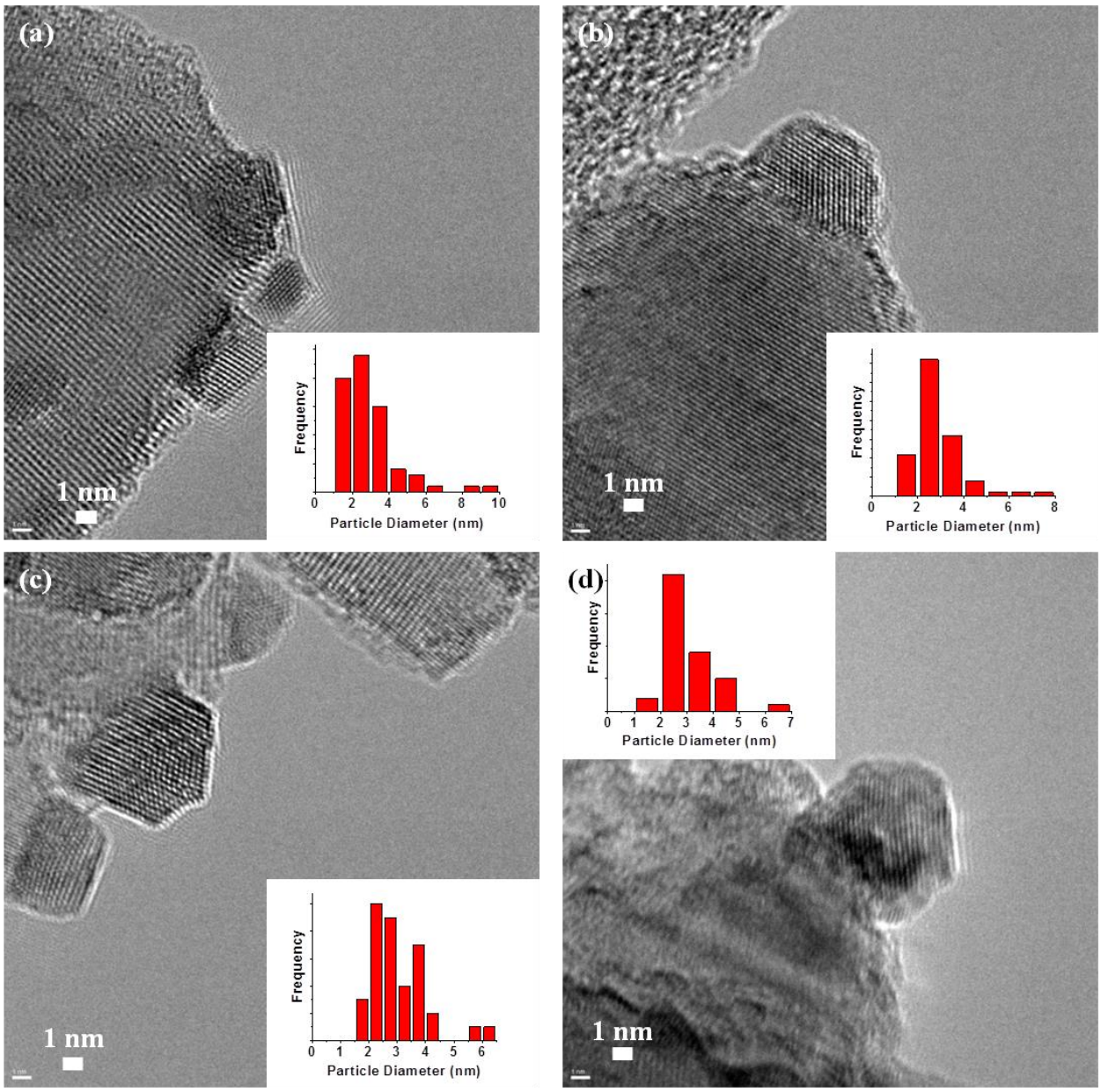

Figure 3.5: TEM micrographs of Rh/TiO_2 and Fe_xRh_y/TiO_2 prepared via the reverse micelle template process. The nanoparticles composition ranges from 100 atomic% Rh to 50 atomic%: (a) Rh/TiO_2 (2.93 nm ± 1.56 nm), (b) $Rh_{0.75}Fe_{0.25}/TiO_2$ (2.78 nm ± 1.06 nm), (c) $Rh_{0.66}Fe_{0.33}/TiO_2$ (3.02 nm ± 1.01 nm), (d) $Rh_{0.5}Fe_{0.5}/TiO_2$ (2.99 nm ± 1.01 nm).

Table 3.1: EDS analysis results of Fe_xRh_y/TiO_2 samples characterized via TEM.

Sample	Ti Atomic%	Fe Atomic%	Rh Atomic%	Ti Wt%	Fe Wt%	Rh Wt%
Rh/TiO_2	94.31	–	5.69	88.53	–	11.47
$Fe_{0.25}Rh_{0.75}/TiO_2$	92.08	1.86	6.05	85.85	2.03	12.12
$Fe_{0.33}Rh_{0.67}/TiO_2$	94.59	1.79	3.62	90.55	1.99	7.45
$Fe_{0.5}Rh_{0.5}/TiO_2$	88.29	7.10	4.62	82.92	7.77	9.31

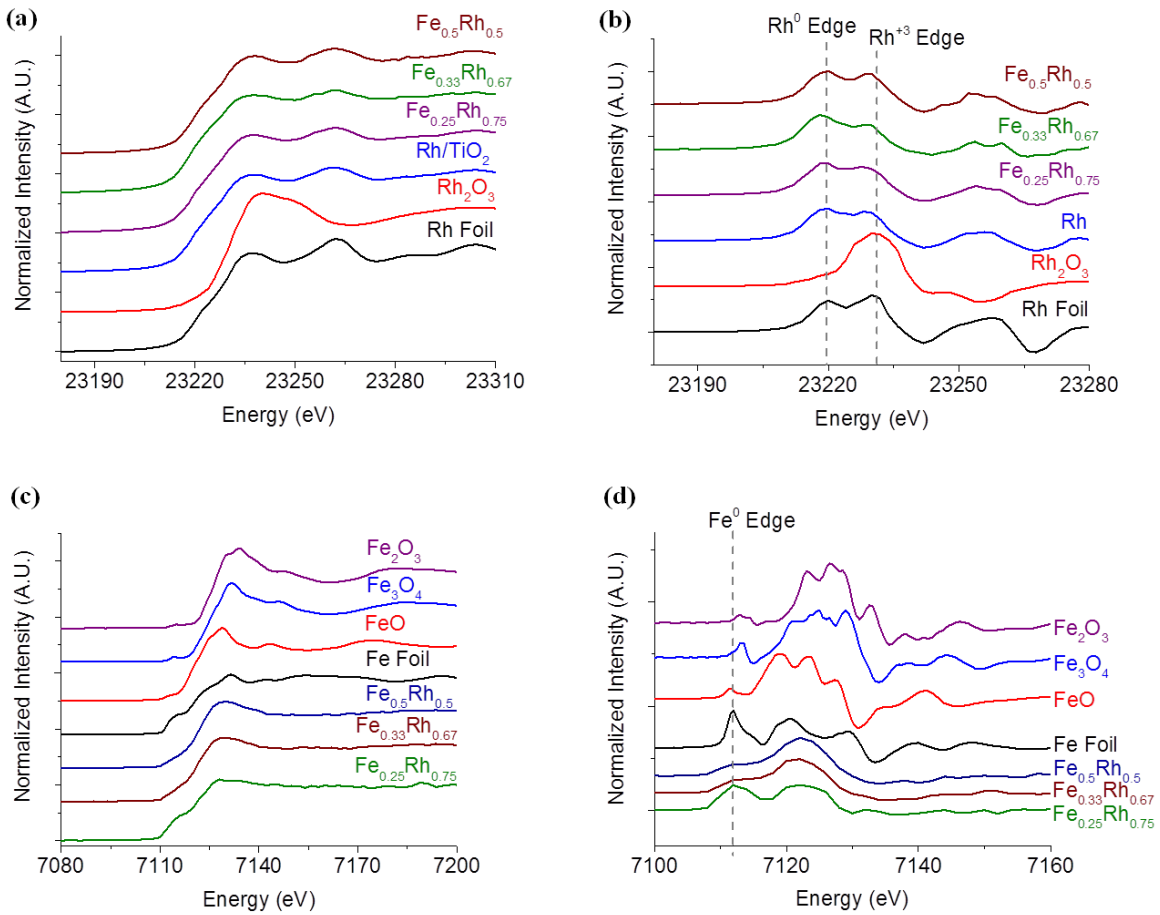

Figure 3.6: XAS spectra of bimetallic catalysts and standards of the Rh K-edge (a and b) and Fe K-edge (c and d): (a and c) XANES spectra (b and d) 1st derivative of normalized XANES.

Through the examination of the Rh K-edge data in Figure 3.6a and 3.6b, it becomes obvious that the reduced catalysts contain Rh^0, with no features that match the oxide, Rh_2O_3. The Fe K-edge data shown in Figure 3.6c and 3.6d shows that for Fe-containing catalysts, the majority of the Fe has an oxidation state of +2, but some of the Fe is metallic. This conclusion is made from the observation that the 1st derivative of the Fe K-edge of these catalysts matches closely with that of FeO, but shares some characteristics with the 1st derivative of the Fe foil XANES.

The XANES region comparison with the standard spectra leaves the general conclusion that Rh is completely reduced to the metallic state, while Fe is only partially reduced to a combination of Fe^0 and FeO. Ordinarily, it is not possible to reduce Fe_2O_3 at a temperature as low as 300 °C, and the apparent partial reduction may be assisted by intimate contact between the oxide and Rh metal. These conclusions are supported by the study of Gogate and Davis who found identical results.[10] The Rh K-edge XANES spectra of the bimetallic catalysts during CO hydrogenation are shown in Figure 3.7. The spectra exhibit negligible changes from the reduced catalysts prior to reaction, with the Rh K-edge XANES remaining consistent.

The local atomic structure of the bimetallic catalysts before and during CO hydrogenation was determined by fitting the EXAFS to a structural model. Due to the low signal-to-noise in the Fe K-edge data, the EXAFS could not be fit to a model. Therefore, only the Rh K-edge data was analyzed. The magnitude of the FT Rh K-edge EXAFS data for reduced $FeRh/TiO_2$ catalysts and catalysts under CO hydrogenation conditions is shown in Figure 3.8. The FT of the reduced catalysts matches closely with that of the Rh foil standard, with the exception of a lower intensity for the 1st shell. This suggests that the catalysts have a lower Rh–Rh coordination compared to bulk metallic Rh. During CO hydrogenation, the 1st shell of the FT appears to widen and the shoulder to the left of the main peak grows in intensity.

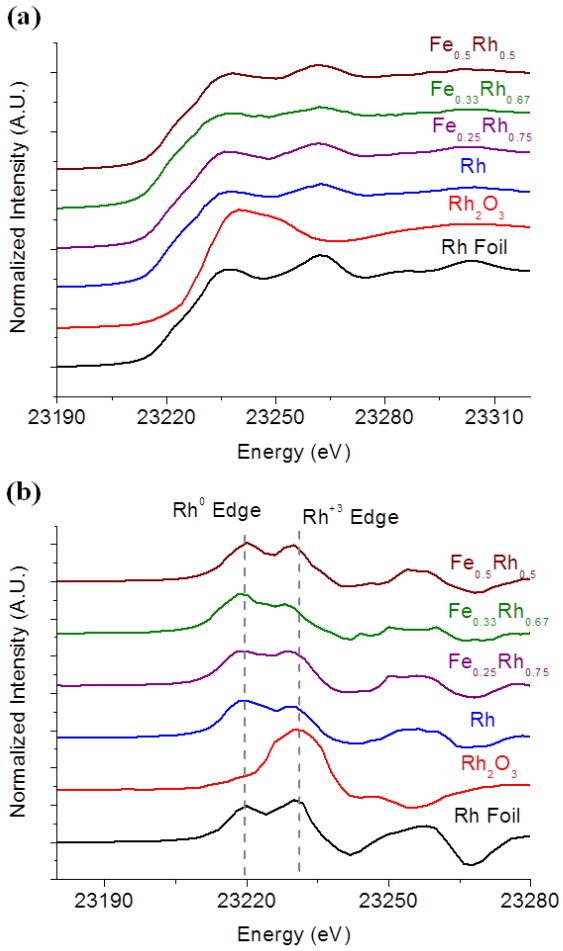

Figure 3.7: Rh K-edge XAS spectra of bimetallic catalyst during CO hydrogenation: (a) Normalized XANES (b) 1st derivative of normalized XANES.

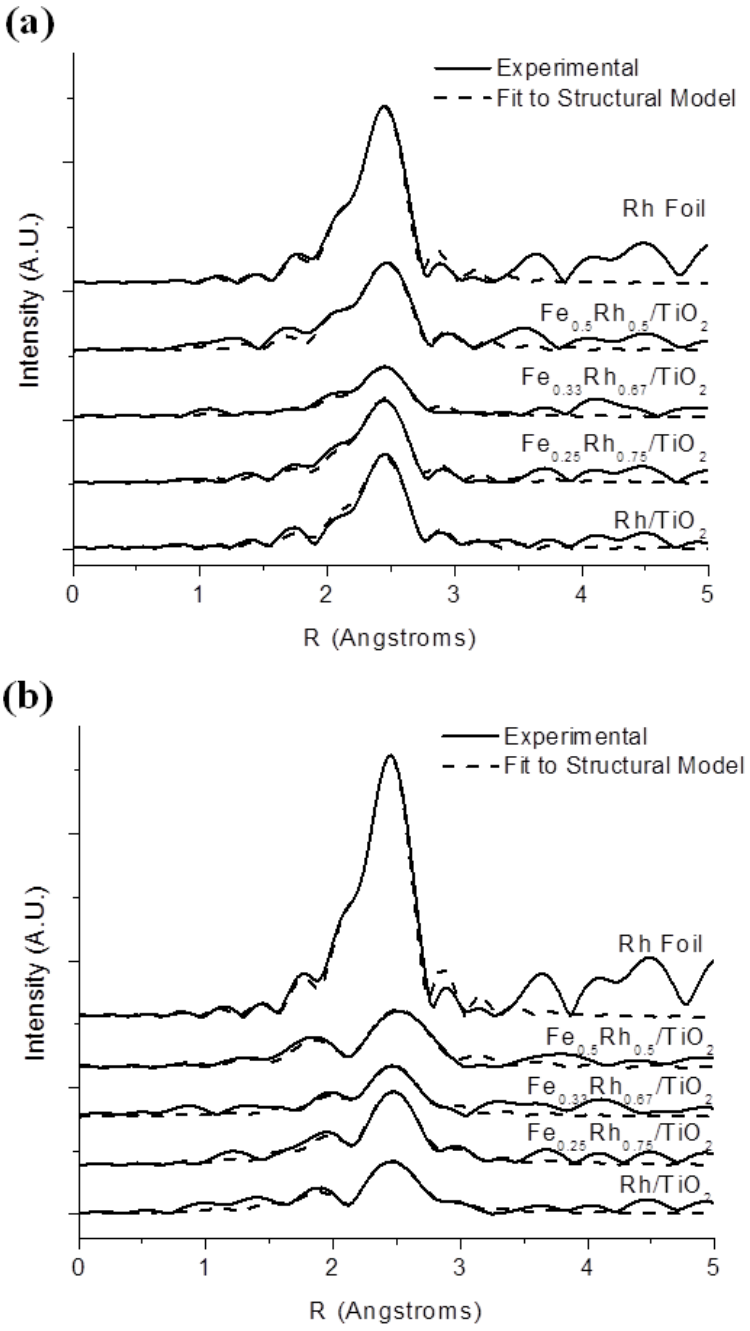

Figure 3.8: Magnitude of the k^2-weighted FT Rh K-edge EXAFS for Fe_xRh_y/TiO_2 catalyst along with fit of 1st shell to a ccp metallic Rh structural model: (a) reduced catalysts, (b) catalysts during CO hydrogenation.

In order to better evaluate the local atomic structure, the fitting results of the Rh K-edge EXAFS to a ccp metallic Rh structural model are summarized in Table 3.2. The Rh–Rh coordination for all reduced catalysts and catalysts under CO hydrogenation conditions is smaller than that of the Rh foil, which suggests Rh exists as nanoparticles. For the reduced catalysts, the Rh–Rh bond length is comparable to that of the Rh foil standard, ~2.68 Å. The only significant change that occured during CO hydrogenation is the increase in the Rh–Rh coordination and a slight shortening of the Rh–Rh bond length, which is still comparable to that of the Rh foil. The increased Rh–Rh coordination is likely due to the sintering of Rh. There was no evidence for the alloying of Rh–Fe, as the shoulder observed in the FT of the catalysts under reaction conditions could not be fit against any known intermetallic alloys of Rh and Fe. Additionally a Rh–Ti contribution was not found either, which would have suggested a strong metal support interaction (SMSI) of Rh with reduced TiO_2.

Table 3.2: Results of the EXAFS fit to Rh metal for reduced Fe_xRh_y/TiO_2 and during CO hydrogenation.

Sample	Conditions	N	r(Å)	ΔE_0(eV)	σ^2(Å^2)
Rh Foil	–	12	2.685(0.002)	3.17(0.43)	0.0037(0.0003)
Rh/TiO_2	Reduced	6.1 (0.6)	2.683 (0.004)	4.04 (0.72)	0.0035 (0.0005)
Rh/TiO_2	Reaction	7.1 (0.5)	2.649 (0.005)	2.05 (0.52)	0.0107 (0.0007)
$Fe_{0.25}Rh_{0.75}/TiO_2$	Reduced	6.0 (0.5)	2.680 (0.003)	3.73 (0.6)	0.0039 (0.0004)
$Fe_{0.25}Rh_{0.75}/TiO_2$	Reaction	7.6 (0.7)	2.670 (0.006)	2.61 (0.66)	0.0084 (0.008)
$Fe_{0.33}Rh_{0.67}/TiO_2$	Reduced	4.4 (0.4)	2.667 (0.005)	4.39 (0.41)	0.0049 (0.006)
$Fe_{0.33}Rh_{0.67}/TiO_2$	Reaction	4.6 (0.5)	2.671 (0.006)	3.31 (0.74)	0.0074 (0.008)
$Fe_{0.5}Rh_{0.5}/TiO_2$	Reduced	6.3 (1)	2.686 (0.007)	4.06 (1.25)	0.0035 (0.0009)
$Fe_{0.5}Rh_{0.5}/TiO_2$	Reaction	7.5 (0.8)	2.671 (0.008)	2.48 (0.78)	0.0091 (0.0011)

3.4 Summary

The reverse micelle template process of controlled nanoparticle deposition is concluded to have an adequate control over the nanoparticle size and composition. This deposition method has proven to be compatible with numerous supports. Any planar support compatible with toluene will produce an ordered sub–ML film of nanoparticles. Additionally, the process can be extended to deposition over powdered supports. The MW of the P4VP block has been confirmed to control the average size of the nanoparticles produced. However, the size distribution has been shown to be larger than expected of a size–selected deposition method, regardless of whether the particles are supported on planar or powdered supports. While the individual nanoparticle composition was not confirmed, the overall composition was found to be close to that of the nominal composition, where discrepancies could be attributed to uncertainty in balance measurements and loss of precursor during preparation. The structural studies found Rh to be completely reduced while Fe was only partially reduced to a combination of Fe metal and FeO. Additionally, fitting the EXAFS data to a structural model reveals that the sintering of Rh occurs that is shown by the increase in the Rh–Rh coordination. Lastly, no contribution of Rh–Fe or Rh–Ti was found in the EXAFS data, which suggests that neither a homogeneous alloy nor a SMSI state was present.

Chapter 4. The Effect of Fe-Rh Alloying on CO Hydrogenation to C_{2+} Oxygenates

This section was published in *J. Catal.*, 329, 87-94, 2015

4.1 Introduction

The need to develop alternative sources of liquid fuels has led to renewed interest in developing catalysts for the efficient conversion of synthesis or 'syngas' (CO + H_2), derived from biomass, coal, and natural gas, to simple alcohols and higher oxygenates.[2, 4-11, 38, 51-55] Currently, the only industrially applied process involves syngas conversion to methanol over a Cu-based catalyst (Cu–ZnO/Al_2O_3) at temperatures above 500 K.[51] While Cu–based catalysts are effective for methanol synthesis, they have poor performance for the production of ethanol and other C_{2+} oxygenates, which is desirable for its higher energy density, ease of handling, and non-toxicity. The search for new catalysts for higher oxygenate synthesis has taken a number of different approaches including the chemical modification of Cu–based methanol catalysts (metal promoters and doping), modified Fischer-Tropsch catalysts (Co, Ru and Fe) and promoted MoS_2 based catalysts.[2, 4]

Among the transition metals, Rh surfaces are known to promote C–C coupling, which should allow the direct conversion of syngas to ethanol and C_{2+} oxygenates, yet Rh–based catalysts primarily produce methane when used without promoters.[2, 4] Various promoters (Fe, CeO_2, V, La, Mn, Ag, Ti, Ir) have been shown to increase ethanol selectivity, with Fe being particularly effective due to its combined methane suppression and enhancement of ethanol production.[2, 4-6, 10] Studies have shown that Fe loading up to 10 % wt has increased ethanol production while suppressing methane formation for Fe–promoted Rh/Al_2O_3.[5] Metal dopants

such as Fe are thought to improve performance by increasing the barrier for methane formation and/or decreasing the barrier for CO insertion.[8] Selectivity studies performed by Haider et, al, also show that both unpromoted and Fe–promoted Rh catalysts exhibit enhanced activity and selectivity for oxygenates when the support is changed from silica to titania.[6] The authors attribute this to an increase in the number of active sites, which would be caused by increased dispersion and/or an enhanced particle-support interface. By modifying Rh –promoter and –support interactions, the activity and selectivity to alcohols can be enhanced at the expense of the least desirable product, hydrocarbons such as methane.

A recent X-ray Absorption Spectroscopy (XAS) study of titania supported FeRh catalysts during CO hydrogenation was performed by Gogate and Davis.[10] Using XANES and EXAFS they determined the principle phases to be metallic Rh and FeO when catalysts were reduced and under CO hydrogenation conditions. One important insight is that there was no change in the atomic and electronic structure when the reduced sample was exposed to syngas (H_2 + CO) at 543K at 1 bar total pressure. The EXAFS data did not conclusively indicate Fe-Rh bonding, but did show Rh bonded to Ti or lattice bound oxygen with bond lengths of 2.53 Å and 2.48 Å, respectively. This conclusion was supported by other studies that found evidence of either Rh–Ti bonding or Rh bonding to lattice bound oxygen in TiO_2.[11, 38, 52] Subsequent transmission electron microscopy (TEM) studies suggest intimate contact of Rh and Fe through the simultaneous detection of Rh and Fe in the same particles studied using spot scans of energy dispersive spectroscopy (EDS).[6] The combined results of these studies suggest that direct contact of Rh with both Fe and Ti is likely to be responsible for the enhanced activity and selectivity of these bimetallic catalysts. This could be due to an ensemble effect where Fe blocks

active sites for hydrogenation of CH_x or a ligand effect where an interaction occurs between Rh and Fe or TiO_2 that creates/increases active sites responsible for CO insertion.

In this work, we used an array of X-ray structural techniques and TEM imaging to determine the structure of FeRh bimetallic catalysts supported on titania. Bimetallic catalysts tested consisted of Rh (~2 wt %) supported on TiO_2 with various amounts of Fe (1–7 wt %). X–ray diffraction (XRD) was used to identify and quantify the amount of each phase in the catalysts (e.g., FeRh alloy, Fe carbides and oxides) and pair distribution functions provided information on local atomic structure (bond lengths and nearest neighbors) and changes in coordination between different Fe concentrations under reactive conditions. In general, these studies show that increasing Fe concentration results in the formation of Fe–rich alloys, but CO hydrogenation conditions induce a carburization (Fe_3C) and oxidation of metallic Fe in catalysts with Fe loadings > 4 wt %. Reactivity studies using a plug-flow reactor and gas chromatography for product quantification were used to correlate catalyst composition with selectivity for ethanol and methane formation from CO hydrogenation. The selectivity for ethanol peaks (~55%) at an Fe loading of ~ 4.5 wt % and closely follows the FeRh alloy content of the catalysts. The addition of Fe also suppresses methane formation and significantly lowers overall CO conversion.

4.2 Experimental Methods

Section 2.1.4 has a detailed description of the synthesis of Fe-Rh/TiO_2 catalysts via incipient wetness impregnation, but the catalysts synthesis is briefly described here. Rhodium (III) nitrate hydrate ($Rh(NO_3)_3 \cdot xH_2O$) and iron (III) nitrate nonahydrate ($Fe(NO_3)_3 \cdot 9H_2O$) are dissolved in de-ionized water and added drop-wise to P-25 titanium dioxide powder (pre-treated

at 450°C in air for 4 hours) to form a paste which is then dried at 180°C overnight and subsequently calcined at 450°C in air for 4 hours. The iron (III) nitrate nonahydrate was varied to produce iron weight percentages ranging from 1% to 8%, while rhodium (III) nitrate hydrate concentration was unchanged to produce ~2% wt Rh in the catalysts. A catalyst containing 2% wt Fe/TiO_2 was also synthesized to compare with Rh containing catalysts. The atomic compositions of the as prepared catalysts were determined by inductively coupled plasma-optical emission spectroscopy (ICP–OES) (Galbraith Laboratories). As shown in Table 4.1, the ICP–OES results indicate that Rh remains relatively constant at ~1.7% wt, while the content Fe ranges from 1.0–7.3 % wt. The different FeRh catalysts will hereon be denoted by the amount of Fe loading (1FeRh, 2FeRh, 3FeRh, 4FeRh, and 7FeRh). The catalysts morphology and composition is characterized via TEM (Tecnai G^2 F20 S–TWIN), by Jordi Llorca (collaborator), and EDS. Additionally, HRTEM was utilized to determine size distributions and crystallographic domains of selected particles.

Reactivity studies were carried out to determine selectivity towards various molecular products during CO hydrogenation. Section 2.3 describes the reactor and product detection setup. The mol % of each product in the gas feed (as determined by GC or MS) was used to calculate the selectivity (S_i) for each product using equation (1):

$$S_i = \frac{M_i \times n_i}{\sum_i M_i \times n_i} \times 100\ \% \qquad (1)$$

where, M_i is the mol % of product i detected and n_i is the number of carbons in product i. This definition of selectivity follows the work of Haider, et al. who performed reactivity studies on similar catalyst systems.[6]

Table 4.1: Results of ICP–OES elemental analysis of Rh and Fe loading (wt %) for different Fe–modified Rh/TiO_2 catalyst samples.

Sample Name	Fe Loading (wt %)	Rh Loading (wt %)
Rh	0	1.9
Fe	1.9	0
1FeRh	1.0	1.7
2FeRh	2.2	1.7
3FeRh	3.4	1.7
4FeRh	4.5	1.7
7FeRh	7.3	1.6

As a measure of the overall activity, CO conversion (%) was also calculated for each catalyst via equation (2):

$$CO\ conversion = \frac{\sum_i \mathrm{M}_i \times n_i}{\mathrm{M_{CO}}} \times 100\ \% \qquad (2)$$

where, M_{CO} is the mol % of CO detected in the gas feed.

Prior to reaction, the sample was reduced at 300°C under 9 mL/min H_2 flow at a pressure of 1 bar for 30 min (GHSV= 0.028 mL·min^{-1}·mm^{-3}). After reduction, the sample was cooled to room temperature in 9 mL/min H_2 flow and the gas switched to a 4 mL/min H_2 flow + 2 mL/min CO flow at a pressure of 1 bar (GHSV= 0.019 mL·min^{-1}·mm^{-3}). The sample temperature was then raised to 240°C to simulate CO hydrogenation reaction conditions; this temperature was chosen after performing the reaction at a range of temperatures and determining the best activity/selectivity for oxygenate production.

Section 2.4 describes the synchrotron experimental setup in detail, but it is briefly described here. The structures of the Fe-Rh/TiO_2 catalysts under different conditions were investigated by XRD and PDF at the X7B beamline at the National Synchrotron Light Source (NSLS) operating at a wavelength of 0.3196 Å. The powder diffraction pattern was collected with a Perkin Elmer amorphous silicon 2–D detector. The detector distance was changed from 400 mm for XRD to 180 mm for PDF measurements. The detector position was calibrated by measuring the diffraction from a sodium hexaboride standard at both detector positions. XRD and PDF data were collected on the as-synthesized samples and after reduction at 300°C for 30 min. under 9 mL/min H_2 flow at a pressure of 2 bar (GHSV= 0.191 mL·min^{-1}·mm^{-3}). After cooling to room temperature, XRD and PDF measurements were made on the reduced catalysts

and then under CO hydrogenation conditions of 4 mL/min H_2 + 2 mL/min CO flow at 240 °C at a total pressure of 2 bar (GHSV= 0.127 $mL \cdot min^{-1} \cdot mm^{-3}$). XRD and PDF data were also collected for the bare support under identical conditions to compare with loaded catalysts for analysis by difference PDF (dPDF) where only the contributions of Fe and Rh are observed. The analysis of the XRD and PDF/dPDF data is shown in detail by section 2.4.4.

4.3 Results and Discussion

4.3.1 Catalyst reactivity: product analysis by mass spectrometry (MS)

The reactivity of the Fe–Rh/TiO_2 catalysts for the CO hydrogenation reaction was studied via MS. Figure 4.1 shows the selectivity towards the major products in the reaction and it is summarized in Table 4.2. The reaction conditions consisted of a 2:1 H_2:CO mix at a total pressure of 1 bar and a temperature of 240 °C. The effect of Fe is immediately noticed as the ethanol selectivity increases by nearly 4–fold while methane selectivity halved. Methane selectivity is further decreased with increasing Fe loading for all Fe concentrations studied here. The ethanol selectivity peaks at an Fe loading of 3.5 wt% Fe, after which is steadily decreased as the Fe loading increases. However, the total oxygenates selectivity continues to increase, which is primarily due to the increase of the other higher oxygenates: acetaldehyde and ethyl acetate. At high Fe loading (>4 wt% Fe), acetaldehyde and ethyl acetate are formed at the expense of ethanol. This would suggest that a high Fe loading favors other C_{2+} oxygenates over ethanol.

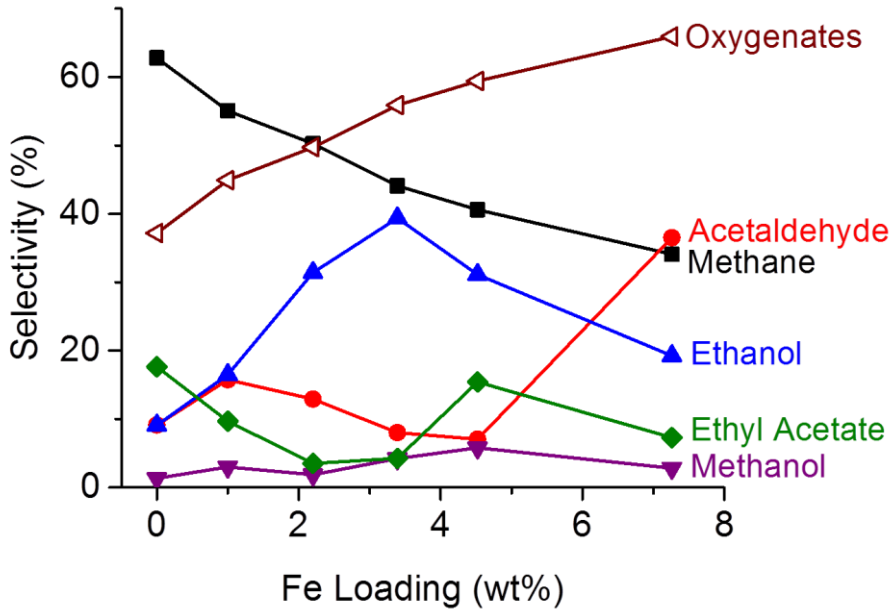

Figure 4.1: Product distribution of CO hydrogenation vs Fe loading on 2 wt% Rh/TiO_2 catalyst collected by MS. Reaction conditions: 2:1 H_2:CO gas mix at 1 bar total pressure and an operating temperature of 240°C.

Table 4.2: Summary of the product distribution during CO hydrogenation on Fe–promoted Rh/TiO_2 catalysts, calculated by MS. Reaction conditions: 2:1 H_2:CO gas mix at 1 bar total pressure and an operating temperature of 240°C.

Sample	Methane (%)	Ethanol (%)	Methanol (%)	Ethyl acetate (%)	Acetaldehyde (%)	Total Oxygenates (%)
Rh	62.8	9.1	1.3	17.6	9.1	37.1
Fe	100	0	0	0	0	0
1FeRh	55.1	16.5	3.0	9.7	15.8	45.0
2FeRh	50.3	31.4	1.9	3.5	12.9	49.7
3FeRh	44.1	39.4	4.2	4.3	8.0	55.9
4FeRh	40.6	31.1	5.8	15.4	7.1	59.4
7FeRh	34.1	19.3	2.8	7.3	36.5	65.9

The CO conversion vs Fe loading is shown in Figure 4.2. Overall, Fe loading serves to suppress CO conversion on 2 wt% Rh/TiO_2. For the Fe loading range of 2 wt% - 5 wt%, CO conversion is severely diminished. Only the 1FeRh exhibits elevated CO conversion, although the cause of is unknown, since the product distribution of 1FeRh closely follows that of the overall trend. The slight increase in CO conversion seen on the 7FeRh catalyst can be explained by the sudden spike in acetaldehyde selectivity that is observed in Figure 4.2. The cause of this sudden increase in acetaldehyde production is also relatively unknown as it does not follow the trend which was observed on the other Fe-containing catalysts.

In general, the reactivity data obtained via MS, agrees with previous literature. As was seen by Burch and Hayes for Fe–promoted Rh/Al_2O_3, methane selectivity is suppressed by the addition of Fe to Rh/TiO_2, and increasing the Fe concentration furthers methane suppression up to 7 wt% Fe.[5] In the study by Burch and Hayes, methane is suppressed by Fe, up to an Fe loading of 10 wt%. However, ethanol selectivity was enhanced up to 3.5 wt% Fe, at which point, it steadily decreased, which was due to the stabilization of acetaldehyde and ethyl acetate formation over ethanol. Haider et al, found that Fe–promotion on Rh/TiO_2 enhanced ethanol selectivity up to 2.5 wt% Fe, after which no significant ethanol enhancement was observed, but CO conversion decreased. Both the approximate peak in ethanol selectivity and the decrease in CO conversion with added Fe loading are somewhat shared with the results in this study. However, Haider et al found that the addition of Fe led to an enhancement of CO conversion, compared to the present study where Fe was found to suppress the overall activity.

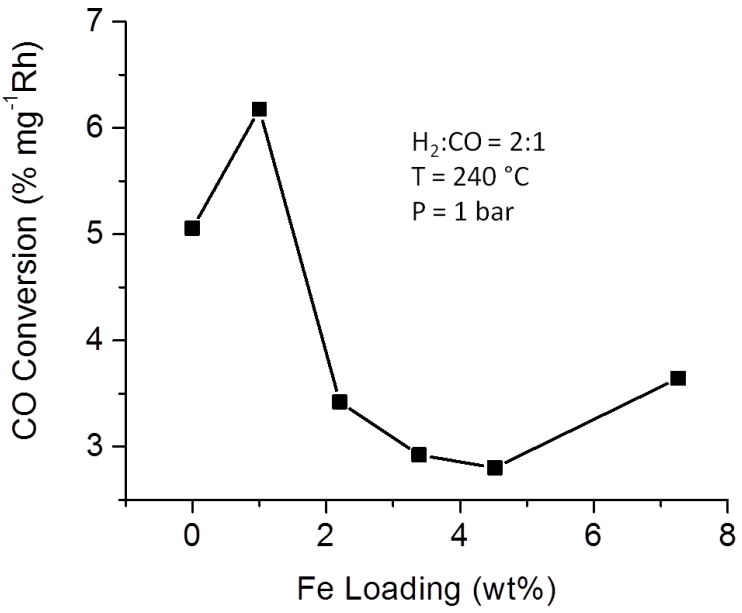

Figure 4.2: CO conversion vs Fe loading for Fe–Rh/TiO_2 catalysts obtained via MS.

While there are notable similarities of the results obtained via MS with the previous literature. There are still discrepancies found with both the selectivity and CO conversion results such as the unexplainably high CO conversion for 1FeRh, and high acetaldehyde selectivity for 7FeRh. These discrepancies are likely due to the nature of the detection method used for product analysis: MS. As was described in the experimental section, many of the products studied in this reaction share common fragments. Additionally, hydrocarbons are notoriously difficult to quantify via MS due to the massive number of fragments seen in the mass spectra. Many of these hydrocarbon fragments can easily contribute to the other products studied here. This can lead to overestimations in product selectivity or CO conversion. For this reason, the reactivity results are repeated with GC detection to ensure that the results found are legitimate.

4.3.2 Catalyst reactivity: product analysis by gas chromatography

The selectivity for various oxygenate products from CO hydrogenation over $FeRh/TiO_2$ catalysts as a function of Fe content using GC product detection are shown in Figure 4.3 and summarized in Table 4.3. These data were taken under the same reaction conditions as the reactivity study performed via MS. The results show that the initial loading of Fe increases the selectivity towards ethanol by a factor of six, while for the most prominent hydrocarbons (methane, propane) the selectivities are greatly reduced. The maximum ethanol selectivity (~55 %) occurs at a loading of ~4.5 % wt Fe, whereas methane is less than half its initial value for the pure Rh catalyst. The decrease in selectivity for ethanol at even higher Fe loading (7 wt %) is accompanied by a slight increase in the hydrocarbon products.

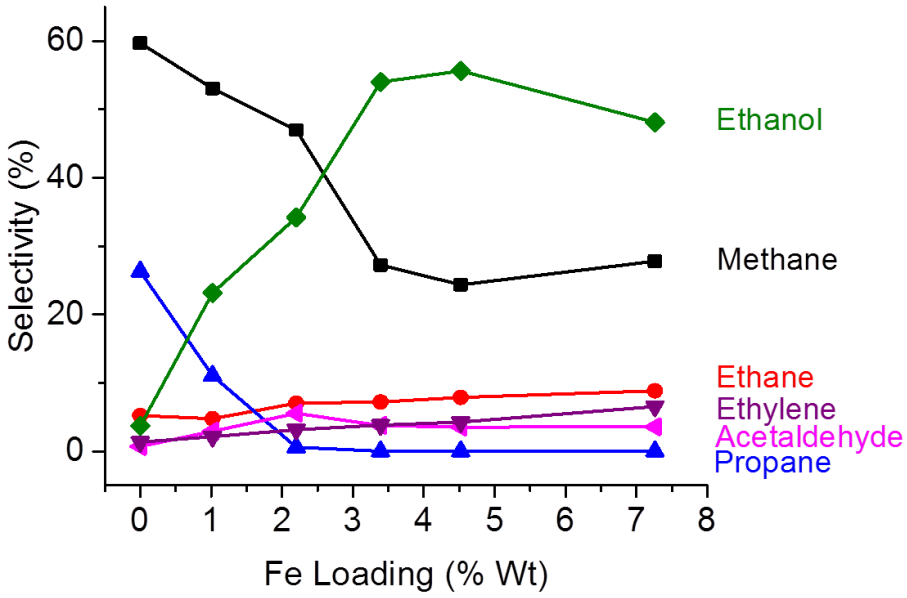

Figure 4.3: Selectivity for various reaction products from CO hydrogenation versus Fe-loading for ~2% wt Rh/TiO_2 catalyst samples obtained via GC. Reaction conditions: 2:1 H_2:CO gas mix at 1 bar total pressure and an operating temperature of 240°C.

Table 4.3: Conversion and selectivity for various products (%) from the CO hydrogenation reaction on the Fe-modified Rh/TiO_2 catalyst samples (listed in Table 1) obtained via GC. Selectivity calculations based on equation (1) in the text. Conversion calculated from equation (2) in the text.

Sample	Methane (%)	Ethane (%)	Ethylene (%)	Propane (%)	Methanol (%)	Ethanol (%)	Acetaldehyde (%)	Conversion (%)
Rh	59.7	5.2	1.3	26.3	0.4	3.7	0.7	11.18
Fe	-	100	-	-	-	-	-	0.03
1FeRh	53.1	4.8	2.1	11.0	1.3	23.1	2.9	4.34
2FeRh	47.0	7.0	3.1	0.3	1.7	34.2	5.5	2.80
3FeRh	27.2	7.2	3.8	-	4.0	54.0	3.8	1.52
4FeRh	24.3	7.9	4.2	-	4.4	55.6	3.5	1.25
7FeRh	27.8	8.8	6.5	-	4.8	48.1	3.5	1.59

.

The conversion of CO, as defined by equation (2), is shown in Figure 4.4 as a function of Fe content. The results show that CO conversion drops significantly with the addition of Fe to the catalysts, which according to Figure 4.3 is also associated with higher ethanol and lower methane selectivity. Under the reaction conditions used here, the Rh–only catalyst exhibits far greater CO conversion than the Fe–only catalyst (Table 4.3), although both produce mostly hydrocarbon products. The fact that mixing the two metals results in a significant shift in product distributions and a large drop in CO conversion indicates that the Fe and Rh components do not act independently, i.e., segregated particles, but their admixture leads to reactive sites which are modified relative to the single metal catalysts. In general, the observed trends in methane and oxygenate selectivity versus Fe-loading are consistent with those found in previous studies of CO hydrogenation on similar bimetallic Fe–Rh supported catalysts.[5, 6] Burch and Hayes found that the ethanol selectivity increases up to 10 wt % Fe loading for Rh/Al_2O_3 supported catalysts with a small but concurrent increase in CO conversion using a reaction pressure of 10 bar and a 1:1 feed of H_2:CO.[5] More recently, Haider, et al. reported that changing the support from SiO_2 to TiO_2 dramatically increases oxygenate selectivity with a maximum (~37 %) occurring for Fe-loadings of 5 wt %.[6] Moreover, they found that CO conversion at a reaction pressure of 20 bar (1:1 H_2:CO) decreased for titania supported catalysts with Fe loadings higher than 2.5 wt %. Our results in Figures 4.3 and 4.4 are generally in agreement with these previous studies using titania as a support, where Fe addition leads to enhanced ethanol selectivity and the suppression of methane. However, Fe addition does not enhance CO conversion at any of the concentrations reported here. Instead, the addition of Fe significantly lowers the overall activity of the catalysts, with the largest percentage drop occurring at the smallest Fe loadings tested.

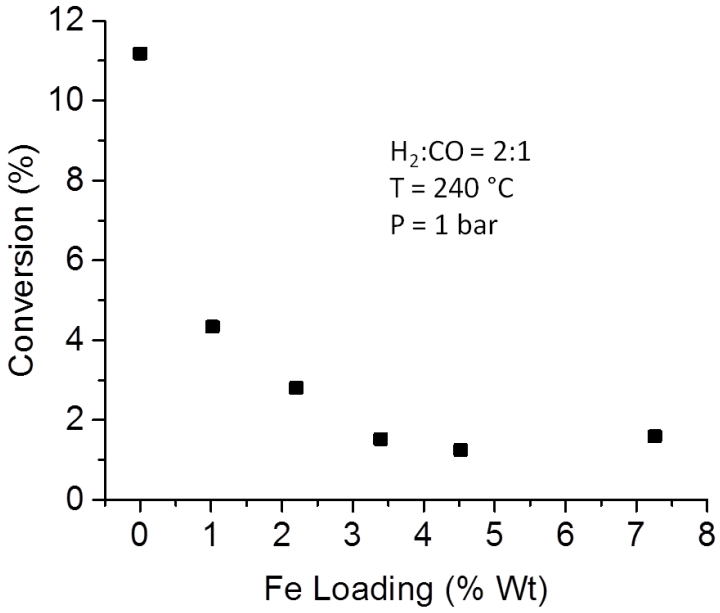

Figure 4.4: Total conversion of CO versus Fe-loading for ~2% wt Rh/TiO_2 catalyst samples. Reaction conditions: 2:1 H_2:CO gas mix at 1 bar total pressure and an operating temperature of 240°C.

A possible cause for the differences in conversion versus Fe addition obtained in this work may be due to the lower reaction pressure (1 bar) compared with that used in previous studies (10–20 bar).[5, 6]

The reactivity results obtained via GC are similar to that of those obtained with MS, but with the absence of discrepancies in the results that contradict the observed trends in reactivity with Fe loading. Firstly, the CO conversion on the Rh–only catalyst was underestimated by MS, due to the lack of detecting various hydrocarbons: Propane, ethane, ethylene. The CO conversion on Rh/TiO_2 was therefore significantly higher in the results obtained via GC. Additionally, the trend in ethanol selectivity vs Fe loading was altered, where a peak in ethanol selectivity followed by a gradual, yet significant drop was no longer observed at 3.5 wt% Fe. Instead, after 3.5 wt% Fe loading, the ethanol selectivity was relatively constant in comparison to the lower Fe loadings. Likewise, the methane selectivity was relatively stabilized in the same Fe loading range. Lastly, no unusual spike in acetaldehyde selectivity was observed on the 7FeRh catalyst like in the MS data. In the GC data, the selectivity of all the products followed the trend observed by the other Fe loadings. Due to the higher quality and reproducibility of the GC data, the reactivity obtained here was used to later compare with the structure determination results.

4.3.3 Catalyst morphology: ex situ TEM

The morphology and atomic composition of the $Fe–Rh/TiO_2$ catalyst particles used in the above reactivity studies were characterized by HRTEM and EDS, respectively. Figure 4.5 shows the combined microscopy results for a reduced and post–reacted Fe–Rh catalyst (2FeRh) which exhibits enhanced activity for ethanol synthesis (see Figure 4.3). The particles show an average

particle diameter of 1.8 ± 0.2 nm, but more importantly, Rh and Fe were always found together in single particle scans with EDS, indicating close contact between Rh and Fe. Moreover, lattice fringe analyses show crystalline particles with a lattice spacing of 2.11 Å. This spacing is consistent with the (110) plane of a FeRh alloy with a space group of pm-3m.[24, 25] Given that HRTEM is heavily dependent on crystal orientation, not observing lattice fringes due to metallic Rh, does not rule out the possibility of its existence. It is possible that a crystallite of Rh was not found in the proper orientation or that Rh was not crystalline at all. The only changes which are evident in the post reaction catalyst is a slight sintering of the particles to a diameter of 2.0 ± 0.2 nm and a small amount of carbon deposition. The minor increase in particle diameter and narrow size distribution observed in the post reaction catalysts indicate that these particles are robust and relatively resistant to sintering under reaction conditions. Figure 4.6 shows HRTEM, EDS, and the size distribution of the reduced and post–reacted 7FeRh catalyst, where the particles with a larger Fe loading are found to have a similar average particle diameter of 1.9 nm ± 0.2 nm and EDS gives an Fe:Rh ratio approximately 4-5 times higher. Observed lattice fringes decrease to 2.08 Å, which is consistent with an increase in Fe concentration of the alloy. The changes that occur in 7FeRh during the reaction are similar to 2FeRh, a slight sintering of the particles and carbon deposition.

The EDS and lattice fringe analyses provide evidence for the presence of FeRh alloy particles, or at least a surface FeRh alloy on Rh metal nanoparticles, in both the reduced and post reaction catalysts. FeO_x is likely to be present due to Fe's high oxidation potential and the detection of carbon in the post reaction samples may also indicate the presence of Fe carbide. We attribute the lack of visualizing the Fe oxides and/or carbides to the high dispersion of the phases and poor contrast from the titania support which greatly reduces their visibility in TEM.

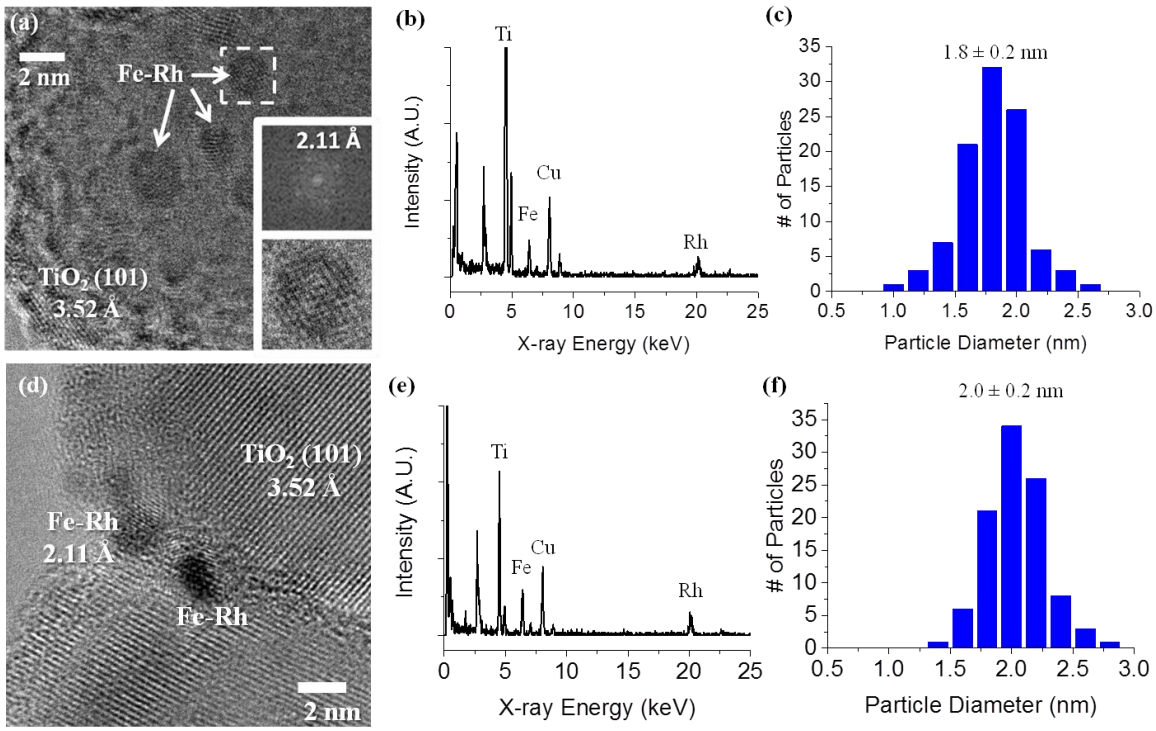

Figure 4.5: Transmission electron microscopy results for the 2FeRh catalyst sample (see Table 1) following reduction (a–c) and reaction (d–f): (a) HRTEM of Fe–Rh nanoparticles with FT of image and lattice fringe spacing assignment (b) Single particle EDS of Fe–Rh nanoparticle showing Fe and Rh together (c) Size distribution of particle diameter (d) HRTEM of post–reaction Fe–Rh nanoparticles (e) Single particle EDS of Fe–Rh nanoparticle (f) Size distribution of particle diameter after reaction. (Performed by Jordi Llorca)

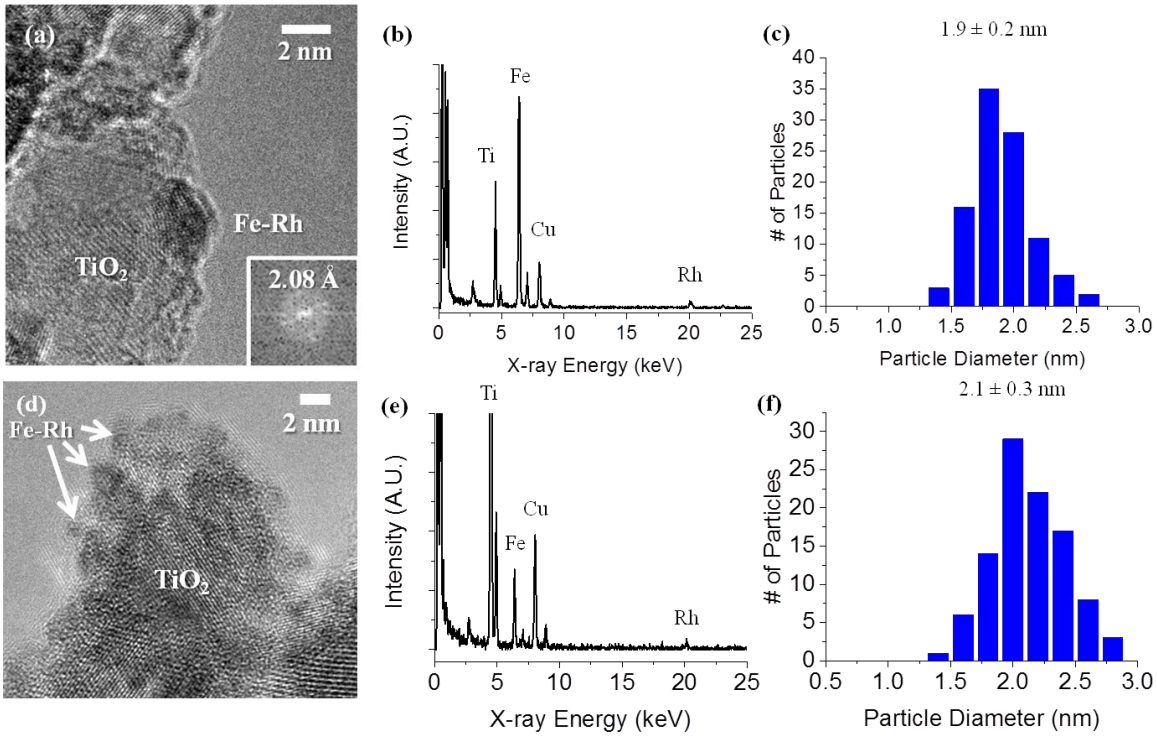

Figure 4.6: Transmission electron microscopy results for the 7FeRh catalyst sample (see Table 1) following reduction (a–c) and reaction (d–f): (a) HRTEM of Fe–Rh nanoparticles with FT of image and lattice fringe spacing assignment (b) Single particle EDS of Fe–Rh nanoparticle showing Fe and Rh together (c) Size distribution of particle diameter (d) HRTEM of post–reaction Fe–Rh nanoparticles (e) Single particle EDS of Fe–Rh nanoparticle (f) Size distribution of particle diameter after reaction. (Performed by Jordi Llorca)

A more detailed structural and phase analysis of the Fe-Rh/TiO_2 catalysts under reaction conditions is presented below.

4.3.4 Catalyst structure under reaction conditions: in situ XRD and dPDF

Reactivity studies discussed above confirm that Fe addition enhances selectivity towards ethanol and suppresses methane selectivity. Previous structural studies concluded that the Fe modification is due to intimate contact between Fe, Rh, and TiO_2, but the nature of interaction of Rh and Fe is still unclear.[9, 10] The XRD of the catalysts studied here are shown in Figure 4.7. In order to better understand the Fe and Rh phases in the catalysts, we focus mostly on the regions of the XRD patterns associated with Fe metal diffraction shown in the inset of Figure 4.8. The assignments of the diffraction features are based on quantitative results obtained from Rietveld refinements of the XRD data. All known alloy structures of Rh and Fe were considered and refinement was attempted on each, but only FeRh and Fe0.7Rh0.3 were plausible based on peak positions and intensity ratios.[24, 25] For the catalysts under CO hydrogenation, the presence of Fe oxide and carbide phases were also included in the refinement.

Figure 4.7a shows XRD for the reduced catalysts in the range where diffraction features from Fe and FeRh alloying are expected to appear. The Rh-only sample is not included, because the diffraction peaks due to metallic or oxidized Rh are overlapped by diffraction from the TiO_2 support. The Fe-only sample exhibits a broad shoulder centered at 9° (2θ) which is attributable to the (110) reflection of metallic Fe.[26] The FeRh bimetallic catalysts show a different shoulder which starts at 8.67° and shifts to slightly higher 2θ with increasing Fe content. This new feature is due to the alloying of Rh and Fe and the shift to higher 2θ is from the formation of more Fe-

rich alloys, as would be expected from the change in Fe:Rh ratio.[24, 25] The refinement data for the reduced catalysts (Table 4.4) show that the introduction of Fe results in the formation of the 1:1 FeRh alloy, which is accompanied by Fe0.7Rh0.3 at higher Fe-loading. The latter is not unexpected, but the Fe-content in the alloy is clearly limited as can be seen by the appearance of metallic Fe at the highest loadings (4FeRh, 7FeRh), where lower loadings only show metallic Fe alloyed with Rh. The latter is not unexpected, but the Fe-content in the alloy is clearly limited as can be seen by the appearance of metallic Fe at the highest loadings (4FeRh, 7FeRh), where lower loadings only show metallic Fe alloyed with Rh.

The XRD patterns for catalysts under CO hydrogenation reaction conditions are shown in Figure 4.7b. For the (1-3)FeRh catalysts, the composition is seen to be unchanged from their reduced state prior to reaction. The XRD patterns for catalysts at higher Fe content (4FeRh, 7FeRh) show a shift in scattering intensity from higher to lower 2θ with a definitive shoulder appearing at 8.7°. At first glance, this shift appears to be from the increase in the FeRh alloy. However, this shift can also be accounted for by the introduction of a carbide phase into the Rietveld refinement. Multiple iron carbides were considered (Fe_5C_2, Fe_2C, and Fe_3C), but the refinement resulted in the addition of only the Fe_3C phase. According to the refinement results summarized in Table 4.4, the Fe metal content is reduced at the expense of Fe_3C formation. Carburization of Fe is not unexpected as the reaction conditions for CO hydrogenation are very similar to Fischer-Tropsch synthesis (FTS) where Fe carbides are formed regardless of the initial phase of the catalyst.[31, 33, 34] Fe_3C is generally accepted as a spectator or deactivation phase and, therefore, its contribution in the CO conversion and product distribution is not expected to be substantial.[34, 56, 57]

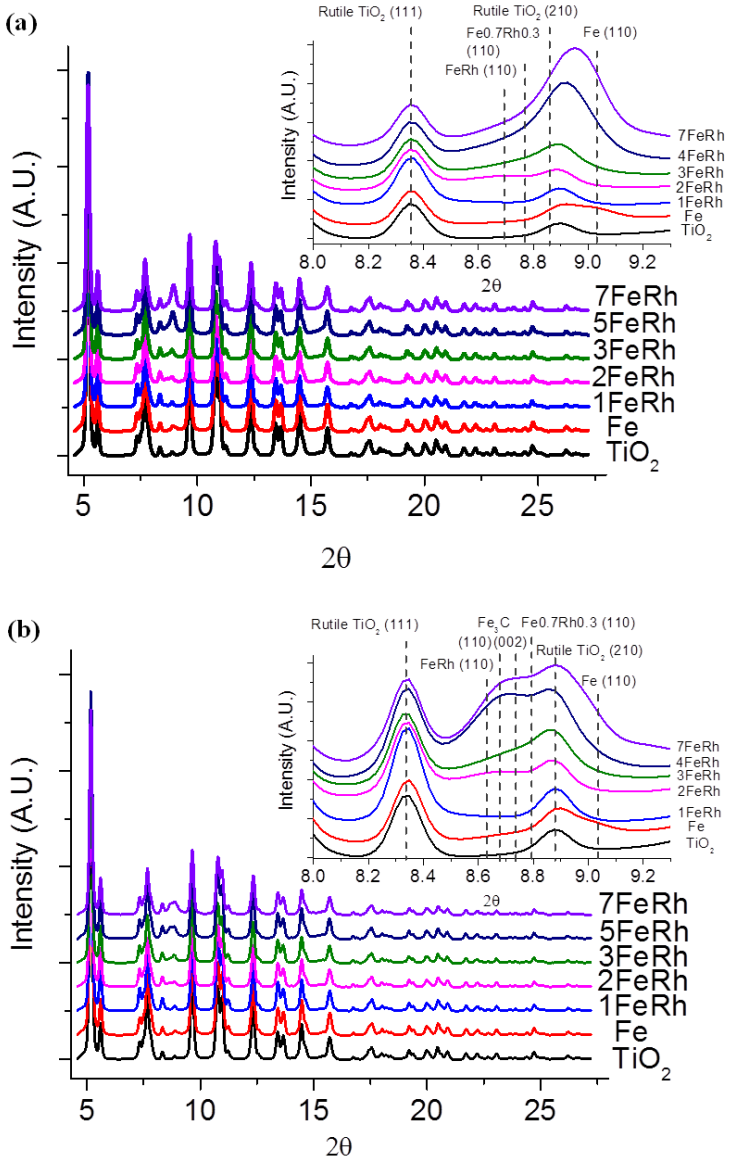

Figure 4.7: Powder x-ray diffraction (XRD) curves for various Fe–modified Rh/TiO_2 catalysts (see Table 4.1 for definition of labels) : (a) after reduction in H_2 at 300°C; (b) during CO hydrogenation reaction conditions using a 2:1 H2:CO gas mix at 1 bar total pressure and an operating temperature of 240°C. Insets show range of XRD where metallic Fe and Fe–Rh alloy appear.

Table 4.4: Quantification of the Fe phase composition (wt%) derived from Rietveld refinements of the XRD data for the Fe-modified Rh/TiO_2 catalysts (listed in Table 1) after reduction in H_2 and under CO hydrogenation reaction conditions. Errors from the Rietveld refinements are shown in parentheses.

Sample	Fe/metal Reduced	Fe/metal Reaction	Fe/alloy Reduced	Fe/alloy Reaction	Fe/Fe_3C Reaction
1FeRh	-	-	0.5 (2)	0.5 (2)	-
2FeRh	-	-	0.75 (9)	0.65 (9)	-
3FeRh	-	-	1.1 (3)	1.0 (4)	-
4FeRh	1.5 (3)	-	1.3 (3)	1.3 (4)	0.9 (2)
7FeRh	3.0 (4)	1.6 (3)	1.0 (3)	1.0 (4)	0.9 (2)

The Fe phase composition of the Fe-Rh catalysts obtained by Rietveld refinement of the XRD data are shown in Figure 4.8 following H_2 reduction and under reaction conditions. For the reduced catalysts (Figure 4.8a), the amount of Fe incorporated into Fe-Rh alloys increases to a maximum near ~4.5 wt % Fe, beyond which the alloyed fraction of Fe decreases. Moreover, the metallic Fe content in the reduced samples increases sharply at higher Fe loadings suggesting that Fe metal segregation occurs which limits the amount of Fe that is incorporated into the Fe-Rh alloy. Under reaction conditions (Figure 4.8b) the amount of Fe-Rh alloy is essentially unchanged, whereas part of the metallic Fe content is apparently transformed to the Fe_3C carbide phase. Overall, the Fe content accounted for by metallic Fe, Fe-Rh alloy, and Fe_3C phases is still less than that determined by elemental analysis. The unaccounted for Fe content could be present as a FeO_x phase, which is not observed via XRD for a similar reason as with TEM, i.e., high dispersion, and low crystallinity. [58, 59]

Assuming all the unaccounted for Fe is present as an oxide, estimates of the FeO_x content were obtained by subtracting the total Fe content obtained by XRD refinement (metallic, alloy, carbide) from the total Fe loading obtained from ICP analyses. The FeO_x content obtained in this way for each catalyst is included in Figure 4.8. For the reduced catalysts (Figure 4.9a), the FeO_x content may be overestimated at low Fe loadings (< 3 wt %) due to difficulties in isolating the metallic Fe phase in the XRD refinements for those samples, but at higher Fe content, the oxide is apparently converted to Fe metal by hydrogen reduction. By comparison, FeO_x is the major Fe phase for all catalysts under CO hydrogenation conditions (Figure 4.8b). The sharp rise in FeO_x at the highest Fe loading (7 wt %) is likely due to oxidation of the relatively large fraction of metallic Fe in the reduced 7FeRh sample prior to reaction (Figure 4.8a).

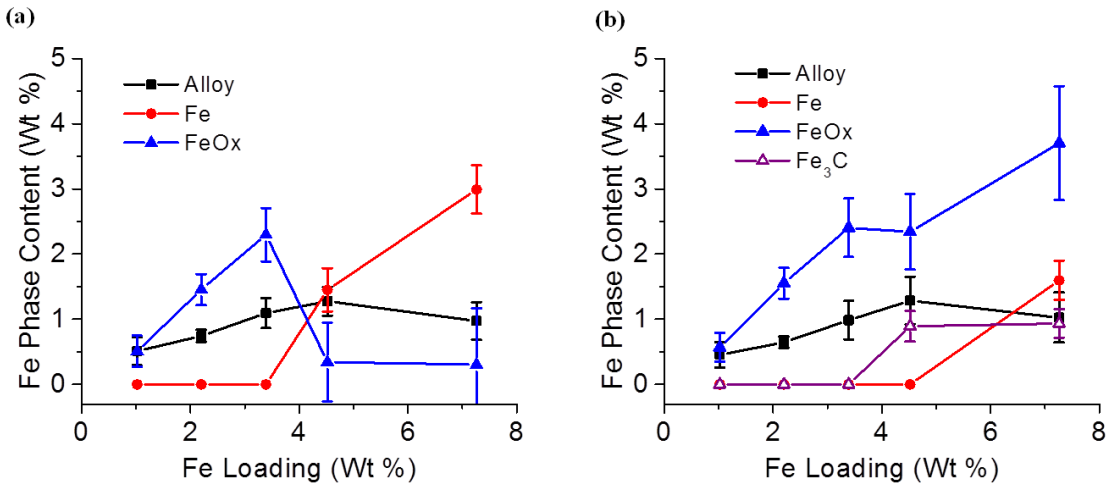

Figure 4.8: A comparison of the amount of different Fe phases versus the total Fe loading for ~2% wt Rh/TiO_2 catalyst samples after (a) H_2 reduction and (b) under CO hydrogenation reaction conditions.

Hence, both the Fe oxide and carbide phase content under reaction conditions appears to be primarily a result of transformation of metallic Fe in the catalysts prior to reaction.

While XRD identifies the phase composition and long range ordering of the catalysts, it provides little information about the local atomic structure of the active phases in the catalysts. PDF has the benefit of resolving the local structure and the further implementation of dPDF allows us to examine only the supported metals deposited which are believed to be the active components of the catalysts. The dPDF of the reduced catalysts are shown in Figure 4.9a. Based on previous studies, the first shell peak at 2.76 Å in the Rh-only data can be assigned to the Rh-Rh bond.[55, 60-62]. With the addition of Fe, this peak begins to broaden and eventually splits into two distinct peaks at 2.53 Å and 2.79 Å at the highest Fe loading. The 2.53 Å distance is indicative of a Fe-Rh or Fe-Fe bond, whereas the peak at 2.79 Å can be attributed to Rh-Rh in the FeRh alloy or a second nearest neighbor of Fe in metallic Fe.[63] The appearance of these two features at higher Fe loading confirms that Fe is being incorporated into a Fe-Rh alloy, and in the case of Fe loading >3 wt %, also forming metallic Fe. A peak due to Fe-O can be observed at ~2 Å, but a distinct modulation in intensity or distance is not observed. However, it is clear that only Fe containing catalysts exhibit a significant peak consistent with a metal-oxygen bond distance. The increase in the area of the peaks associated with metal-metal bonding (2.5-2.9 Å) also signifies that the coordination of Rh and Fe is growing as well. From the Rietveld refinement results in Table 4.4, changes in coordination can be associated with the growth of both Fe-Rh and Fe-Fe domains. Overall, these observations are consistent with the XRD data which also show the Fe-Rh/Fe-Fe contribution increasing with higher Fe-loading. One notable difference between the dPDF and XRD data is the observation of metallic Rh-Rh bonds suggesting isolated domains of metallic Rh.

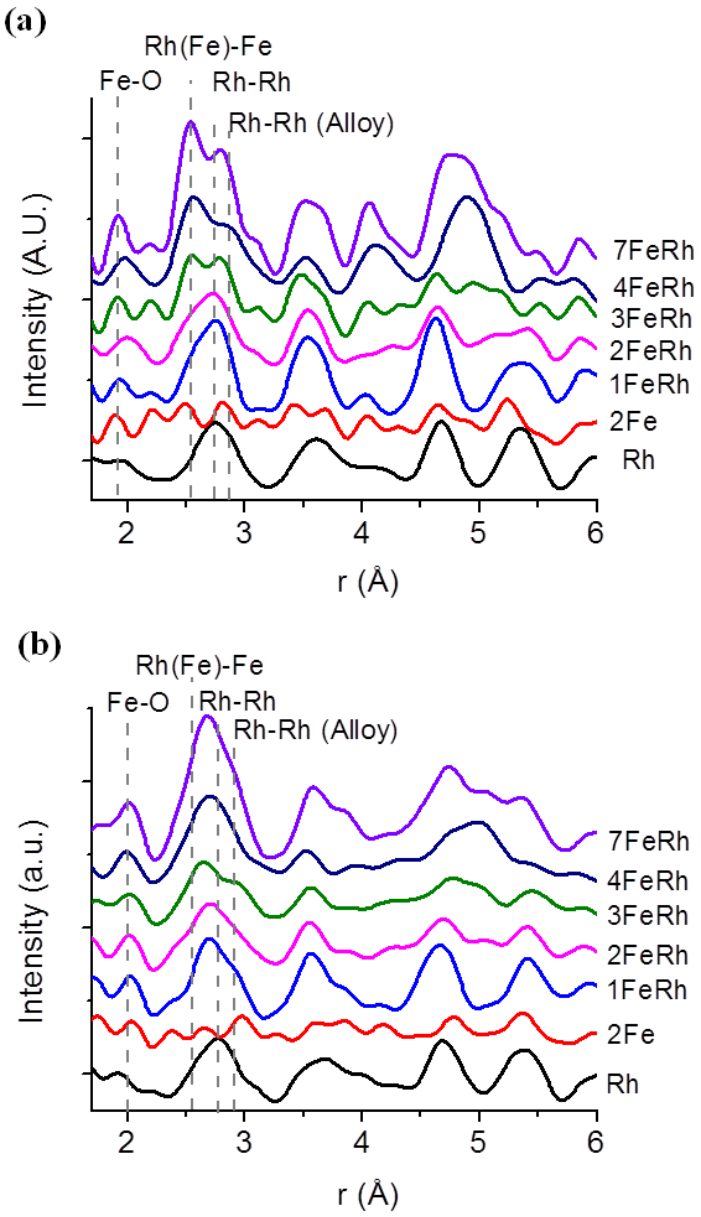

Figure 4.9: Differential pair distribution functions (dPDF) after removal of the TiO_2 contributions for different $FeRh/TiO_2$ catalysts (see Table 1 for definition of labels) for different treatment conditions: (a) after reduction in H_2 at 300°C; (b) during CO hydrogenation reaction conditions using a 2:1 H_2:CO gas mix at 1 bar total pressure and an operating temperature of 240°C.

The latter could be explained by core-shell particles with Fe-Rh alloys in the near surface region and internal cores of metallic Rh. This is consistent with the theoretical work by Yang and Liu where Fe was expected to segregate to the surface of Rh, and the EXAFS study of Ichikawa and Fukishima where the majority of Fe exists in the oxide phase at the interface between Rh and the support, while Fe^0 exist on the surface of the Rh nanoparticles.[8, 9]

Figure 4.9b shows the dPDF curves for the same catalysts under CO hydrogenation conditions (240 °C, 2:1 H_2:CO ratio @ 6 mL/min). The most apparent change compared to the reduced catalysts is that the first shell peak has shifted closer to Rh-Rh bond distances and has increased in width, indicative of a decrease in the Fe-Rh and Fe-Fe coordination with respect to Rh-Rh. At the highest Fe loadings, the first shell peak is broad and centered at an intermediate metal-metal bond distance of 2.66 Å. This suggests multiple components with a range of Rh-Rh and Fe-Rh distances and coordination environments. From the XRD results, we know that Fe metal formed during the reduction at high Fe loadings (> 4 wt %) is lost to carburization and oxidation. This would lead to a loss of coordination in the Fe-Fe peak and a decrease in the intensity of the peak at 2.53 Å. Hence, the first shell peak is mostly representative of Rh-Rh coordination. Overall, the changes in the peak intensities and positions are consistent with the trends observed in XRD. Again, there is no noticeable change in the feature attributed to Fe-O, but the dPDF data suggests that FeO_x is present for all Fe loadings.

As described above and shown in Figures 4.8 and 4.9, the compositions of the Fe and Rh metal phases change significantly with Fe-loading and under reaction conditions. To see how this correlates with selectivity of the catalysts, the selectivity data for ethanol and methane formation are plotted in Figure 4.10 along with the Fe alloy, metal, carbide, and oxide phase compositions for all the catalysts studied. As seen in Figure 4.10a, the ethanol selectivity closely correlates

with the FeRh alloy content, but not the Fe_3C carbide phase, which is only seen at the highest Fe loadings studied (4FeRh and 7FeRh). The FeO_x content also follows ethanol selectivity except at higher Fe loading where the selectivity decreases but the oxide content continues to increase. The latter is most likely due to the increase in metallic Fe content in the reduced catalysts at higher Fe loading (4FeRh and 7FeRh) which is oxidized to FeO_x under reaction conditions. The concomitant decrease in methane selectivity also correlates with FeRh alloy and Fe oxide phase content as shown in Figure 4.10b. These comparisons suggest that the presence of FeRh alloys enhance ethanol selectivity and simultaneously suppress methane, whereas Fe_3C formation does not appear to have a significant effect on product distribution. This is consistent with the role of Fe_3C in FTS, which is thought to be a spectator or deactivator phase.[34, 56, 57] The importance of FeO_x in influencing selectivity is less clear, but its presence under reaction conditions (Figure 4.9b) suggests that it is acting synergistically with the Fe-Rh alloy (or pure Rh), as the Fe-only sample shows essentially no ethanol formation under these reaction conditions. The interface of FeO_x could influence product selectivity by modifying or blocking sites on the Rh active phase and more generally act to enhance selectivity similar to changing the Rh support from SiO_2 to TiO_2.

Overall, these data support the general conclusion that Fe-Rh alloys enhance ethanol selectivity, while simultaneously suppressing methane. Due to the intimate Fe-Rh contact in the alloy fractions, the Fe is likely altering both the number and nature of active Rh sites, which allows ethanol synthesis to compete with methane formation.

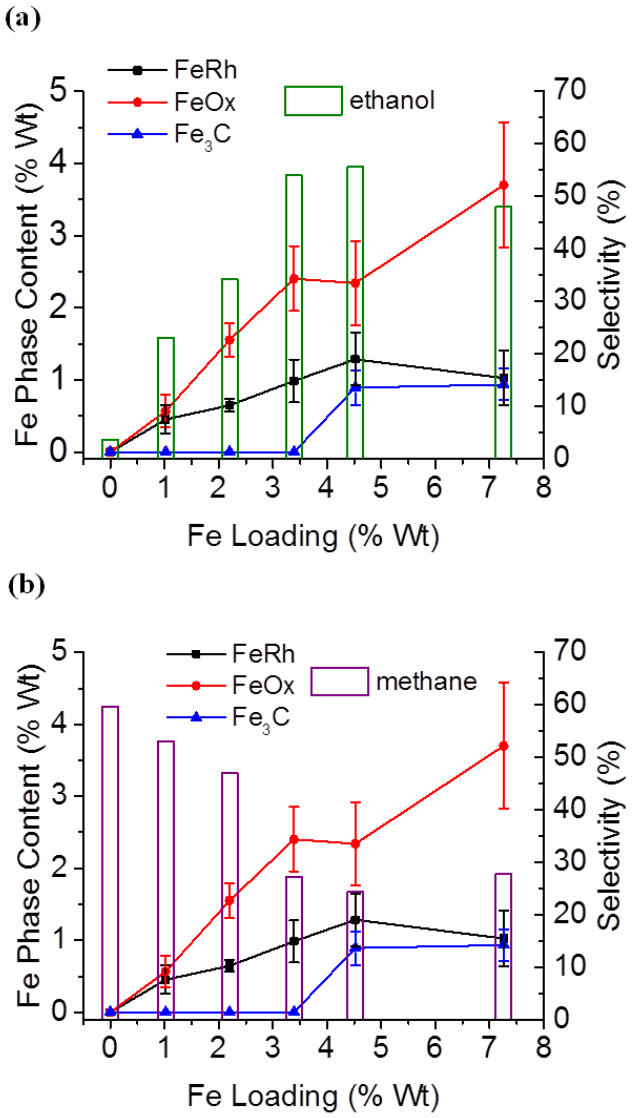

Figure 4.10: Comparisons of product selectivity for CO hydrogenation with the Fe phase content of $FeRh/TiO_2$ catalysts as a function of Fe-loading; (a) selectivity for total oxygenates and ethanol production and Fe content in alloy and oxide phases; (b) selectivity for methane production and Fe content in alloy and oxide phases. Reaction conditions: 2:1 H_2:CO gas mix at 1 bar total pressure and an operating temperature of 240°C.

Density functional theory (DFT) calculations and kinetic Monte Carlo (KMC) simulations suggest that the key factors determining the selectivity of Fe-doped Rh surfaces for ethanol formation are the relative barriers for methyl hydrogenation, $CH_{3(a)} + H_{(a)} \rightarrow CH_{4(g)}$, and CO insertion, $CH_{3(a)} + CO_{(a)} \rightarrow CH_3CO_{(g)}$.[7, 8] The latter reaction leads to ethanol after subsequent hydrogenation steps. According to the calculations, Fe addition lowers the barrier to the CO insertion step and thereby increases selectivity of ethanol relative to methane.[8] Our conclusion that a surface Fe-Rh alloy contributes to the improved ethanol selectivity is consistent with the main findings of these calculations, which were based on Fe-doped Rh surfaces with both metals participating. This also explains the slight decrease in ethanol selectivity at the highest Fe loading where phases other than the Fe-Rh alloy (Fe metal, FeO_x, and Fe_3C) become more prevalent.

4.4 Summary

The combined results from TEM, XRD, and dPDF provide clear evidence for the presence of FeRh alloy in mixed Fe and Rh catalysts following reduction and during CO hydrogenation. Specifically, the presence of Fe-Rh alloy observed in TEM is supported by the Rietveld refinements of the XRD data and trends in the dPDF data, all of which show that the alloy concentration increases with increasing Fe content. Furthermore, the XRD results indicate that a substantial fraction of metallic Fe is both carburized and oxidized during CO hydrogenation. The dPDF data also points to the presence of a pure Rh phase, which becomes more pronounced during CO hydrogenation conditions. The latter may suggest that Fe and Rh form a surface alloy, with the core of the particle being pure Rh.

The overall picture to emerge is that at low Fe loadings, the Fe is partially incorporated into the Rh nanoparticles as a surface Fe-Rh alloy. The remaining amount of Fe is tied up in oxide formation which could be located near the Rh nanoparticles or on the TiO_2 support. The amount of surface alloy increases with increasing Fe-loading up to ~4 wt %, beyond which segregation to metallic Fe becomes favored over Fe-Rh alloy formation. During CO hydrogenation conditions, the metallic Fe deposits and some of the Fe in the surface alloy are converted to both oxide and carbide phases. Although Fe_3C is present on high Fe loading catalysts (4FeRh, 7FeRh), no substantial correlation is found with conversion or product distribution. This could be related to the fact that Fe_3C is suspected as a spectator/deactivator phase in FTS.

The combined correlation (Figure 4.10) of Fe-Rh alloy and FeO_x content with increases in ethanol selectivity and methane suppression suggests that FeO_x may also play a role in ethanol synthesis. The fact that the CO conversion is a minimum for the highest ethanol selectivity and lowest methane selectivity (Figures 4.3 and 4.4) also suggests that the enhancement role of Fe-Rh alloy and FeO_x is the modification and/or blocking of Rh sites responsible for methane and/or other side reactions. These findings are consistent with the conclusions of early studies that the interface between Rh and Fe is responsible for suppression of catalytic activity due to the blocking of active sites.[5, 10]

Chapter 5. The Effects of Oxide Support on the Performance of Fe–promoted Rh Catalysts for CO Hydrogenation

5.1 Introduction

In the past few decades, alcohol synthesis from syngas has received a significant spike in interest due to their high energy density, relatively cleaner emissions and their compatibility with the current fuel delivery and storage infrastructure. The current commercial process for alcohol synthesis via syngas conversion is the production of methanol over a Cu–ZnO/Al_2O_3 catalyst.[1] While this catalyst proves to be both highly active and selective towards methanol, it shows low selectivity towards higher oxygenates, such as ethanol, which are desired for their low toxicity and even higher energy density. Rh–Fe bi-metallic catalysts are among one of the few catalysts capable of providing a high selectivity towards ethanol, while simultaneously suppressing methane formation.[2, 5, 6, 64]

Although it has been well established that ethanol selectivity is dependent upon the Fe concentration, as was observed by the results described in chapter 4, a relatively new finding is that changing the support of Rh–Fe bi-metallic catalysts can have a significant effect on both CO conversion and the overall product distribution.[6, 64] Haider *et al.*, discovered that changing the support of Fe–promoted Rh catalysts from SiO_2 to a more reducible metal oxide, TiO_2, enhanced both the activity and selectivity towards oxygenates.[6] A high selectivity towards ethanol over Fe–promoted Rh/TiO_2 was also observed by the earlier work in our group.[64] This enhanced selectivity is thought to be linked to the reducibility of the support by the availability of its oxygen vacancies. In fact, Gogate and Davis' results from an *in situ* XAS study on a Fe–Rh/TiO_2 catalyst indicate that the enhanced activity and selectivity towards oxygenates were due to the

interaction of Rh with the reduced Fe and Ti oxides.[10] It is believed that changing the support to a metal oxide which possesses a higher degree of reducibility would result in an even greater enhancement of activity and selectivity towards higher oxygenates such as ethanol. For this reason, CeO_2 is chosen as it is already known to be a promoter for enhancing activity and selectivity towards ethanol production.[3]

In this study, XRD was used to determine the structure of Fe–Rh bimetallic nanoparticles supported on CeO_2. All catalysts tested contained 2 wt% Rh with an Fe loading varying from 0–8 wt%. XRD was used for phase identification and quantitative composition (e.g. determining amount of Fe metal, Fe_xRh_y, Fe_xC_y, FeO_x). The content of the Fe–Rh alloy fraction is found to be higher at low Fe loadings on CeO_2 than TiO_2. Under reaction conditions, a significant portion of the Fe in the Fe–Rh alloy on CeO_2 is carburized. Reactivity studies were also performed on all catalysts studied via XRD in an attempt to correlate catalytic activity/selectivity with the catalysts structure and composition. The peak ethanol selectivity (~ 52%) on Fe-Rh/CeO_2 is found to be similar to that on TiO_2 but at a somewhat smaller Fe loading of 2.5 wt%. Additionally, ethylene selectivity is enhanced by increasing the Fe loading on Fe-Rh/CeO_2.

5.2 Experimental Methods

\ The CeO_2 supported Fe–Rh bimetallic catalysts were prepared via the incipient wetness impregnation method described in the literature and section 2.1.4 in detail.[64] Rhodium (III) nitrate hydrate and iron (III) nitrate nonahydrate are dissolved in de–ionized water. The Rh and Fe precursors are varied to produce a constant 2 wt% Rh and 0–8 wt% Fe sample. The aqueous

solution is added drop–wise to nanoparticulate CeO_2 until a paste is formed. The paste is dried at 120 °C overnight and then calcined in air at 450°C for 4 hours.

Reactivity studies were carried out in the same manner as previously reported by our group, using GC as the detection method.[64] The sample is reduced at 300 °C under a 9 mL/min flow of pure H_2 (GHSV= 0.028 $mL \cdot min^{-1} \cdot mm^{-3}$) at a pressure of 1 bar for 30 min. The sample is then cooled to room temperature and the reactant flow is switched to 4 mL/min H_2 + 2 mL/min CO (GHSV= 0.019 $mL \cdot min^{-1} \cdot mm^{-3}$) at a total pressure of 1 bar. The sample temperature is then sequentially raised from 240 °C to 270 °C every 3 hours to study the effect of temperature on catalytic activity and selectivity. The CO conversion and normalized selectivity is determined in the same manner as described in sections 2.3 and 4.2.

The XRD of Fe–Rh/CeO_2 catalysts under reducing and reaction conditions were conducted at the 11-ID-B beamline of the APS operating at a wavelength of 0.2124 Å and X7B of the NSLS operating at a wavelength of 0.3196 Å. An amorphous silicon 2–D detector (Perkin Elmer) was used to collect the powder diffraction pattern. A sample to detector distance of 900 mm or 400 mm at the APS or NSLS, respectively, was used to collect XRD. The detector position was calibrated by the measuring the diffraction from a sodium hexaboride or CeO_2 standard. A detailed description of the experimental setup for the *in situ* XRD is found in section 2.4.4. The catalysts were reduced at 300 °C under 9 mL/min H_2 flow at a pressure of 2 bar (GHSV= 0.191 $mL \cdot min^{-1} \cdot mm^{-3}$) for 30 min and XRD was collected after cooling to room temperature. The reactant flow was changed to 4 mL/min H_2 + 2 mL/min CO at a total pressure of 2 bar (GHSV= 0.127 $mL \cdot min^{-1} \cdot mm^{-3}$). The temperature was increased to 240 °C just as in the reactivity studies and the *in situ* XRD is collected on the catalysts during CO hydrogenation. The

method of XRD data analysis has been previously reported and is described in described in detail by section 2.4.4.[64]

5.3 Results and Discussion

5.3.1 Reactivity Studies

The CO conversion for Fe–Rh/CeO_2 vs Fe loading for temperatures ranging from 240 °C to 270 °C is shown in Figure 5.1. Due to the unusually low CO conversion on the Rh–only catalysts at 240 °C, the reactivity of each catalyst was studied at higher temperatures. For all catalysts, increasing the reaction temperature increased the CO conversion. However, changing the reaction temperature had no effect on the overall trend of CO conversion vs. Fe loading, which only experienced an initial increase with the addition of Fe and a subsequent decrease followed by a leveling off with increased Fe loading . What is peculiar is the fact that Rh by itself exhibits a CO conversion less than 1 %. This is in great contrast with the previous literature (even results previously reported by our group) of Rh supported on other metal oxides, such as TiO_2, SiO_2, and Al_2O_3, where Rh exhibits a CO conversion comparable to or higher than Fe–promoted Rh catalysts.[5, 6, 10, 64] However, the results by Li *et al.* on 1 wt% Rh/TiO_2 with 0− 10 wt% CeO_2 loading show that, while the addition of CeO_2 enhances ethanol selectivity and CO conversion, increased CeO_2 loading serves to decrease the CO conversion. They attribute the increase in reactivity to the appearance of a new active site on the Rh-CeO_2 interface which is determined from a new medium temperature CO desorption peak in the CO-TPD that reaches a maximum at 1 wt% CeO_2 loading. They simultaneously observe that CO adsorption on Rh is suppressed as CeO_2 loading increases. Once the new desorption peak disappears at high CeO_2 loading (> 2 wt% CeO_2), the CO conversion experiences a significant drop.

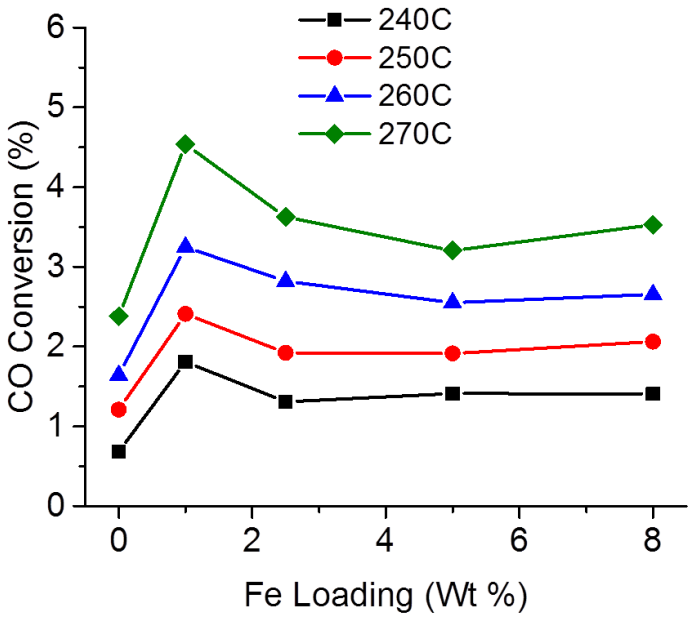

Figure 5.1: CO conversion of Fe–Rh/CeO_2 catalysts vs Fe loading at temperatures ranging from 240 °C to 270 °C.

They conclude that an appropriate ratio of Rh:CeO_2 is crucial for the enhancement of ethanol production and overall CO conversion. We believe that the suppressed CO conversion observed on Rh/CeO_2 is due to the high Rh:CeO_2 in the catalyst, which is the result of the excessively strong interaction of Rh and CeO_2 at this ratio. The Overall, CO conversion is nearly independent of Fe loading outside of the initial increase seen upon the addition Fe at 1% wt.

The methane selectivity vs. Fe loading for the same temperature range is shown in Figure 5.2. Methane selectivity decreases sharply with Fe loading until 2.5 wt% Fe, above which the methane selectivity begins to slowly increase. Similar to the CO conversion, the reaction temperature does not change the overall trend of methane selectivity vs. Fe loading, however, increased temperatures lead to significantly higher methane selectivity.

The ethanol selectivity vs. Fe loading for Fe–Rh/CeO_2 at temperatures ranging from 240 °C to 270°C is shown in Figure 5.3. The relationship between ethanol selectivity and Fe loading is the inverse of the methane selectivity and Fe loading. More specifically, increasing Fe loading increases ethanol selectivity to a maximum at 2.5 wt% Fe, above which decreases the ethanol selectivity. Increasing the reaction temperature causes the ethanol selectivity to decrease, while methane selectivity increases, as observed in Figure 5.2. This suggests increased temperature favors methane at the expense of ethanol. As with CO conversion and methane selectivity, reaction temperature does not affect the trend observed with changing Fe loading on ethanol selectivity.

Another notable result from the reactivity study of Fe–Rh/CeO_2 is that Fe stabilizes the formation of another hydrocarbon, ethylene. Figure 5.4 shows the ethylene selectivity as a function of Fe loading on Fe–Rh/CeO_2 catalysts from 240 °C to 270°C.

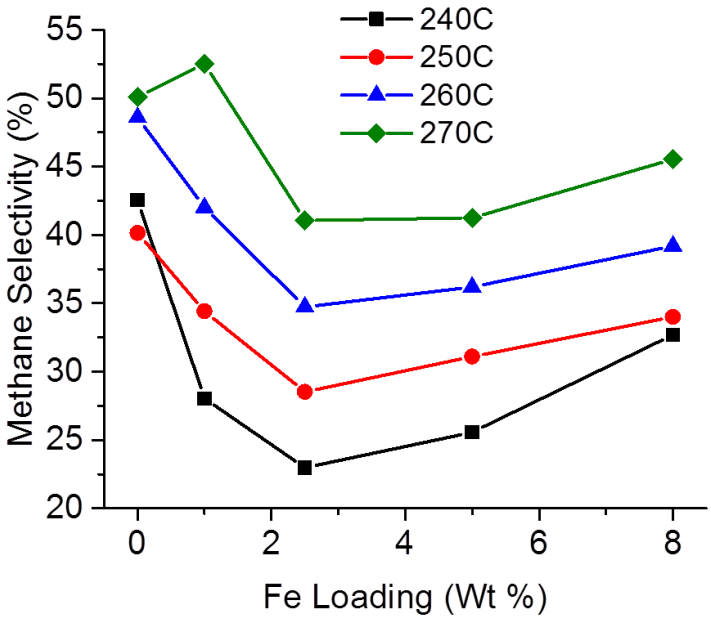

Figure 5.2: Methane selectivity vs Fe loading for Fe–Rh/CeO_2 at temperatures ranging from 240 °C to 270 °C.

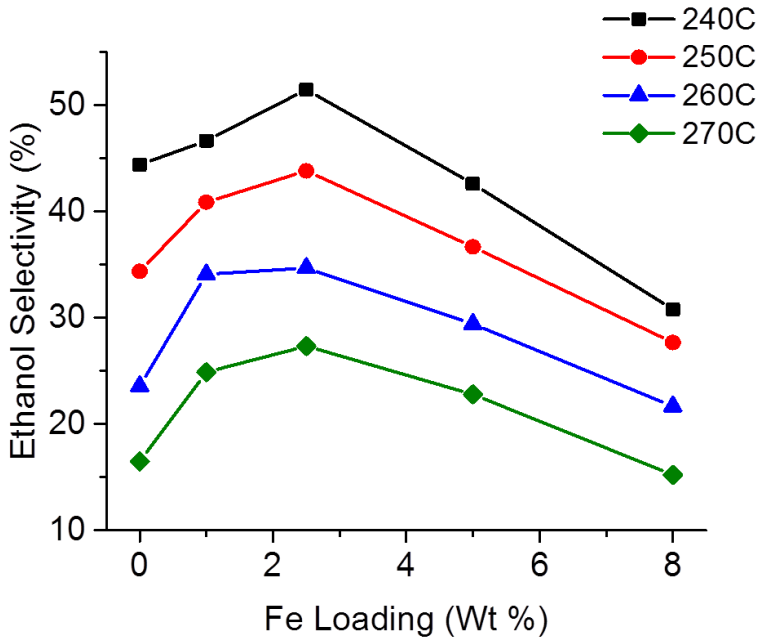

Figure 5.3: Ethanol selectivity vs Fe loading for Fe–Rh/CeO_2 catalysts at temperatures ranging from 240 °C to 270 °C.

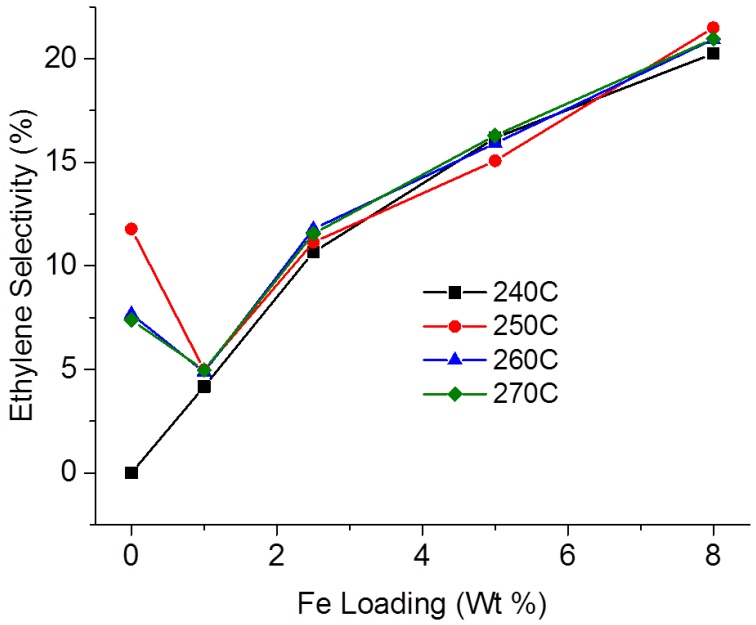

Figure 5.4: Ethylene selectivity vs Fe loading for Fe–Rh/CeO_2 catalysts at temperatures ranging from 240 °C to 270 °C.

Ethylene selectivity shows a positive correlation with Fe loading for all Fe loadings studied here. However, reaction temperature appears to have no effect on ethylene selectivity, which is in contrast with the other major products, methane and ethanol. Additionally, the stabilization of ethylene production by Fe was not observed in our previously reported study of Fe–Rh/TiO_2.[64]

In general, increasing the reaction temperature did not affect the dependence of reactivity on Fe loading. Instead, the product distribution and CO conversion of each catalysts was affected in the same manner. In particular, increasing the reaction temperature raises the CO conversion, but also results in a shift in the product distribution where methane and ethylene selectivity is increased while ethanol selectivity goes down. Overall, CO conversion increases 4 fold with a temperature increase from 240 °C to 270 °C, but the ethanol selectivity drops by almost half. This suggests that a major cause for the increased conversion is due to an increase methane production. However, despite the reduced ethanol selectivity, increasing the reaction temperature does produce more ethanol. Reaction temperature has no effect on ethylene selectivity, which suggests that its intermediate does not compete with any of the other products formed in the reaction. Also, since Fe–promotion is seen to enhance ethylene formation only on CeO_2, it is possible that Fe forms an interface with CeO_2 that creates or increases new active sites that facilitate ethylene formation.

There are a number of significant differences between the CO hydrogenation reactivity on Fe–Rh/CeO_2 and Fe–Rh/TiO_2. Table 5.1 shows a comparison of CO hydrogenation reactivity results for Fe–Rh/CeO_2 and Fe–Rh/TiO_2. In comparison to Fe-Rh particles supported on TiO_2, particles supported on CeO_2 exhibit similar ethanol selectivity, except for that of Rh/CeO_2, which has an ethanol selectivity greater than 40 %.

Table 5.1: Comparison of CO hydrogenation reactivity on Fe–Rh/CeO_2 with Fe–Rh/TiO_2 (2:1 H_2:CO, 1 bar, 240 °C). *a data taken from [64].

Fe Loading (wt%)	Support	CO Conversion (%)	Methane Selectivity (%)	Ethane Selectivity (%)	Ethylene Selectivity (%)	Propane Selectivity (%)	Ethanol Selectivity (%)
0	TiO_2	[a]11.2	[a]59.7	[a]5.2	[a]1.3	[a]26.3	[a]3.7
0	CeO_2	0.7	42.5	9.4	0	0	44.4
[a]1	TiO_2	[a]4.3	[a]53.1	[a]4.8	[a]2.1	[a]11.0	[a]23.1
1	CeO_2	1.8	28.0	4.6	4.2	0	46.6
[a]2.2	TiO_2	[a]2.8	[a]47.0	[a]7.0	[a]3.1	[a]0.6	[a]34.2
2.5	CeO_2	1.3	23.0	6.3	10.7	0	51.5
[a]4.5	TiO_2	[a]1.3	[a]24.3	[a]7.9	[a]4.2	[a]0	[a]55.6
5	CeO_2	1.4	25.6	6.7	16.2	0	42.6
[a]7	TiO_2	[a]1.6	[a]27.8	[a]8.8	[a]6.5	[a]0	[a]48.1
8	CeO_2	1.4	32.7	7.8	20.3	0	30.8

However, the CO conversion on CeO_2 supported catalysts is low on all catalysts studied, especially that of unpromoted Rh/CeO_2 (< 1 %) which is much lower than on Rh/TiO_2 (> 10 %). The reasons for such low CO conversions on ceria catalysts are attributed to a strong interaction between Rh and CeO_2, which blocks active sites, as seen by the suppressed CO adsorption by Li *et al.* in their CO-TPD results. Additionally, CeO_2 supported catalysts exhibit a greater promotion of total hydrocarbons than those supported on TiO_2. For CeO_2 supported catalysts, the ethanol selectivity also reaches a maximum at a lower Fe loading on than on TiO_2. For CeO_2 supported catalysts, the ethanol selectivity reaches a maximum at a lower Fe loading on than on TiO_2. Nonetheless, the catalysts exhibiting the highest ethanol selectivity for both supports (outlined in red on Table 5.1) show similar catalytic performance, i.e., similar CO conversions, and ethanol and methane selectivities. Hence, neither support shows significant advantages in performance for Fe-promoted Rh catalysts when optimized for Fe loading and operating conditions, e.g., temperature.

5.3.2 X-ray Diffraction Studies

The reactivity results indicate that Fe–promoted Rh behaves slightly different on CeO_2 in comparison to TiO_2. XRD was performed in order to determine if the structure of Fe–Rh is any different when supported on CeO_2. Figure 5.5 shows the XRD of reduced and *in situ* Fe–Rh supported on CeO_2. The catalysts with an Fe loading of 1, 2.5, and 8 wt% Fe were measured at the APS and are consequently grouped together, while the catalysts consisting of 5 wt% Fe was measured at the NSLS and, therefore, appears alone due to the difference in sample to detector distance. All XRD diffractograms show an inset of the region of diffraction due to Fe–Rh. A visual examination of the reduced XRD (Figure 5a and 5c) reveals that peaks due to $Fe_{0.7}Rh_{0.3}$ grow in intensity as the Fe loading is increased. Additionally, no significant shift in peak position

is observed from the increased Fe composition, indicating that the Fe:Rh ratio is relatively constant. During CO hydrogenation (Figure 5b and 5d), the peaks due to $Fe_{0.7}Rh_{0.3}$ are diminished, while peaks due to Fe_3C appear in the 'high' Fe loading catalysts (≥ 5 wt% Fe) indicating that at a portion of Fe in Fe–Rh is carburized.

There are a number of similarities and differences of Fe–Rh/CeO_2 with Fe–Rh/TiO_2. The Fe–Rh alloy increases with Fe loading regardless of which support is used. However, metallic Fe is stabilized on Fe loadings > 4 wt% Fe when supported on TiO_2, while metallic Fe was not detectable on CeO_2. Additionally, only one phase of Fe–Rh alloy is formed on CeO_2, while the Fe:Rh ratio increases with Fe loading on TiO_2. Both supports have Fe_3C stabilized during CO hydrogenation at the expense of Fe in the Fe–Rh alloy. A common occurrence on both supports is the absence of peaks due to metallic Rh; the latter is due to all the Rh being tied up in the FeRh alloy or highly dispersed Rh^0 nanoparticles, which are not visible by XRD.

Rietveld refinements were performed on the XRD data for FeRh/CeO_2 catalysts to quantify the amounts of each phase identified. The results are shown in Figure 5.6. The alloyed Fe content increases with the increase in Fe loading. However, the alloyed Fe concentration begins to level off at higher Fe loadings, suggesting that the alloying of Fe and Rh is limited and Fe in other phases (e.g., oxide) may be formed at higher Fe loading. Similar to what was seen in the XRD pattern, Fe loadings ≥ 5 wt% show the formation Fe_3C and loss of alloyed Fe. The amount of Fe_3C does not appear to depend on Fe loading, but an unusually high error for carburized Fe is seen in the measurement on the 5 wt% Fe catalysts. This high error makes a correlation between Fe loading and carburized Fe difficult, and so the only conclusion that can be made is that Fe loading ≥ 5 wt% Fe results in the carburization of Fe in the Fe–Rh alloy.

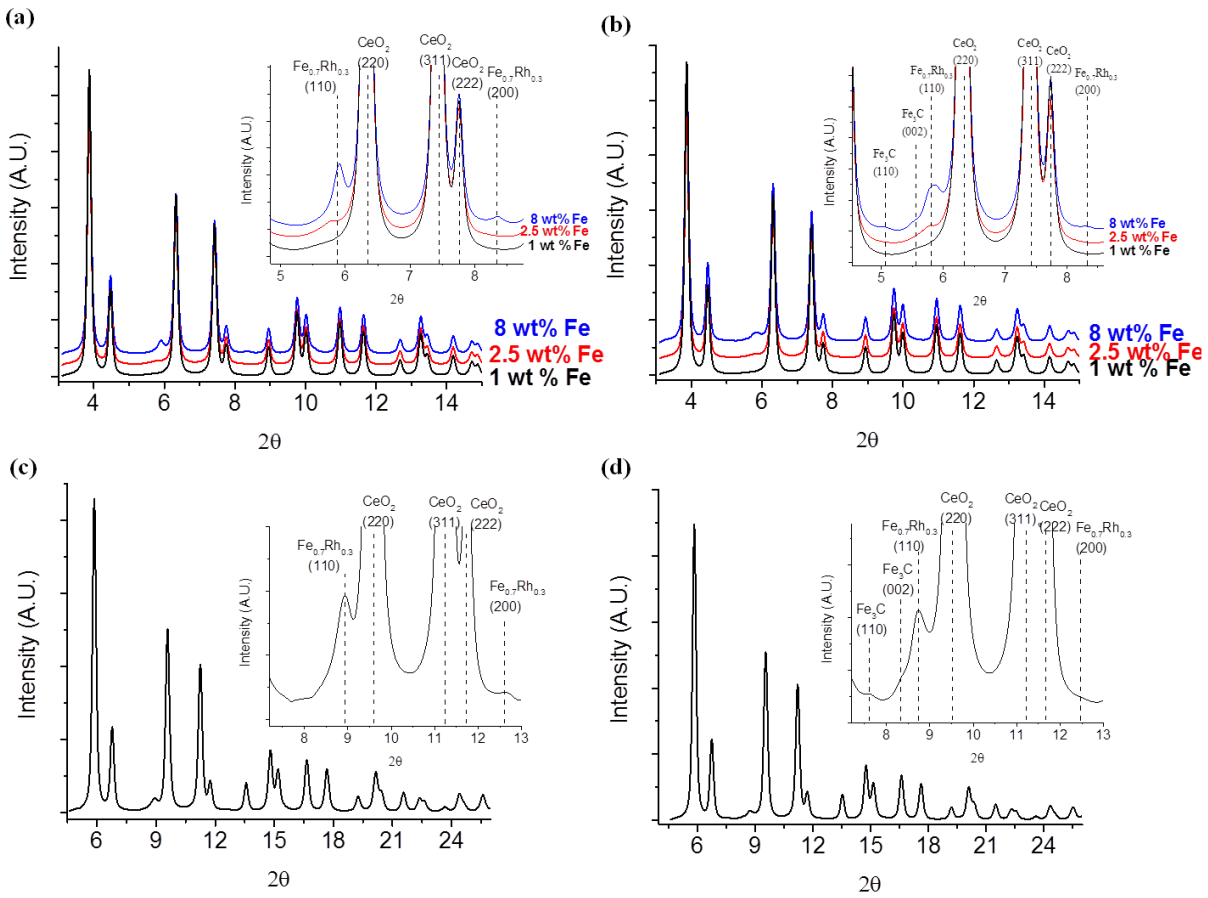

Figure 5.5: XRD of reduced (a, c) and *in situ* (b, d) Fe–promoted Rh/CeO_2 with inset of labeled Fe region: (a) Reduced 1, 2.5, and 8 wt%Fe catalysts, (b) *in situ* 1, 2.5, and 8 wt% Fe catalysts, (c) reduced 5 wt% Fe catalyst, and (d) *in situ* 5 wt% Fe catalyst.

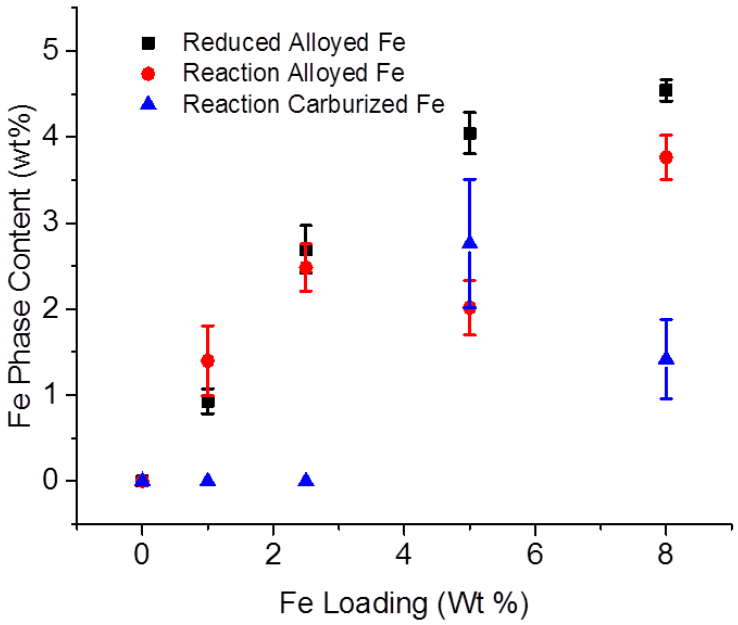

Figure 5.6: Fe Phase content vs Fe loading of reduced and *in situ* Fe–Rh/CeO_2 catalysts.

What can also be observed is that a larger decrease in alloyed Fe is seen in the 5 wt% Fe catalysts, which consequently has a larger carburized Fe content. This further strengthens the argument that Fe in the Fe–Rh alloy is carburized to form Fe_3C.

In order to discern the structural differences between CeO_2– and TiO_2–supported catalysts, the comparison of the Rietveld refinement results is summarized in Table 5.2. It becomes obvious that CeO_2 promotes the alloying of Fe and Rh, as the amount of alloyed Fe is 2 to 4 times as large on CeO_2 as is seen on TiO_2. The same can be said of carburized Fe, whose concentration is almost entirely due to the loss of alloyed Fe during the reaction. Overall, supporting Fe−Rh on CeO_2 serves to stabilize the Fe–Rh alloy[64] with the concentration reaching 4.5 wt% before beginning to level off. The susceptibility to carburization is similar to TiO_2−supported catalysts, as Fe_3C is seen at approximately the same Fe loading for either support.

Correlations between Fe phase content of the FeRh/CeO_2 catalysts with product selectivity for CO hydrogenation are plotted in Figure 5.7. As can be seen by Figure 5.7a, ethanol selectivity follows changes in alloyed Fe fraction with increasing Fe loading up to 5 wt%, but falls off at 8 wt% Fe loading despite an apparent increase in the Fe alloy fraction. By comparison, the methane selectivity in Figure 5.7b follows the opposite trend with alloyed Fe concentration. It can therefore be concluded that Fe–Rh alloy promotes ethanol selectivity while simultaneously suppressing methane up to ~ 5 wt% alloyed Fe, but any further increase in alloying may reduce Rh active sites that are necessary for the formation of ethanol. This result is similar to FeRh/TiO_2 where the FeRh alloys were identified as the active phase for high ethanol selectivity, albeit at higher Fe loading.

Table 5.2: Comparison of Rietveld refinement results of Fe–Rh/CeO_2 with Fe–Rh/TiO_2. *a data taken from [64].

Fe Loading (wt%)	Support	Fe/metal Reduced	Fe/metal Reaction	Fe/alloy Reduced	Fe/alloy Reaction	Fe/Fe_3C Reaction
[a]1	TiO_2	[a]-	[a]-	[a]0.5(2)	[a]0.5(2)	[a]-
1	CeO_2	-	-	0.9(1)	1.4(4)	-
[a]2.2	TiO_2	[a]-	[a]-	[a]0.75(9)	[a]0.65(9)	[a]-
2.5	CeO_2	-	-	2.7(3)	2.5(3)	-
[a]4.5	TiO_2	[a]1.5(3)	[a]-	[a]1.3(4)	[a]1.3(3)	[a]0.9(2)
5	CeO_2	-	-	4.0(2)	2.0(3)	2.8(7)
[a]7	TiO_2	[a]3.0(4)	[a]1.6(3)	[a]1.0(4)	[a]1.0(4)	[a]0.9(2)
8	CeO_2	-	-	4.5(1)	3.8(3)	1.4(5)

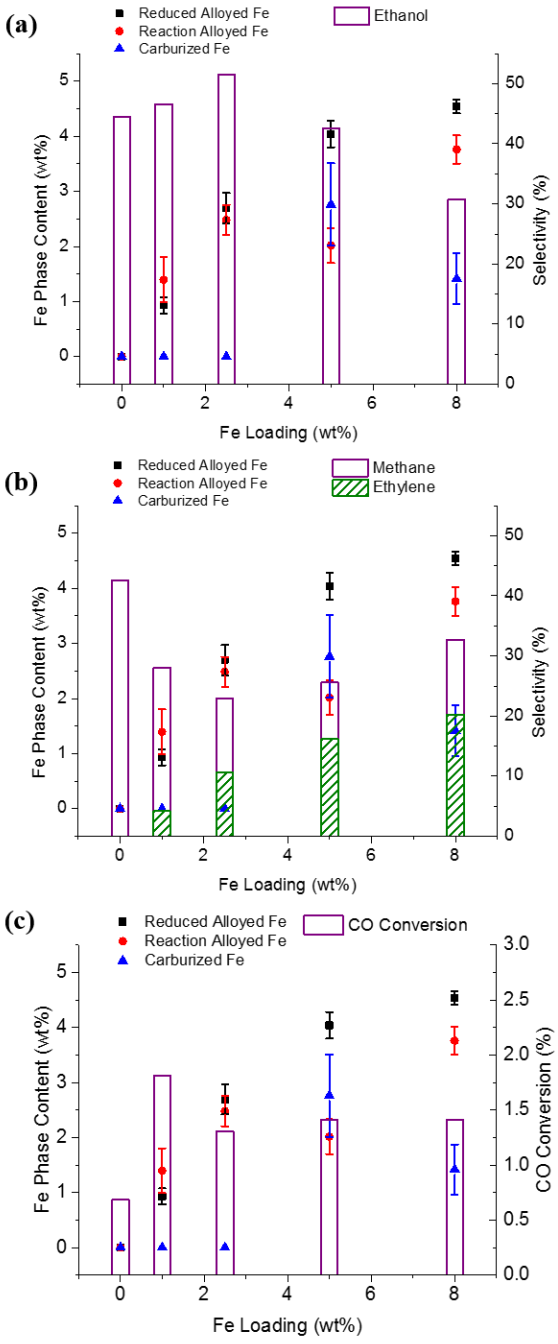

Figure 5.7: Fe phase content vs reactivity results: (a) ethanol selectivity, (b) methane + ethylene selectivity, (c) CO conversion.

Also similar to FeRh/TiO_2 catalysts, the Fe_3C content does not appear to have a major effect on either methane or ethanol selectivity, especially considering the large Fe_3C concentrations which are formed at higher Fe loadings (≥ 5%wt).

Ethylene selectivity was shown to increase with increased Fe loading and Figure 5.7b demonstrates the effect that Fe–Rh alloying has on ethylene selectivity. While, ethylene selectivity shows a near linear dependence on the reduced alloyed Fe concentration, the relationship with the *in situ* alloyed Fe concentration is less obvious. The *in situ* alloyed Fe concentration decreases on the 5 wt% Fe catalyst, but ethylene selectivity still increases. Since neither FeRh nor Fe_3C has exclusive control over ethylene selectivity, the current results of this study cannot conclude the cause of the enhanced ethylene selectivity. The refinement results are also compared to the CO conversion calculated in the reactivity study in Figure 5.7c. As was observed with the overall Fe loading, there does not appear to be any dependence of alloyed or carburized Fe on CO conversion.

5.4 Summary

Overall, changing the support for Fe–promoted Rh from TiO_2 to CeO_2 has little effect on the final CO conversion and product distributions. However, subtle changes could be seen in the trends for both the reactivity and structure of the catalysts with Fe loading. Specifically, the peak ethanol selectivity for the CeO_2 support is observed at a lower Fe loading than that for TiO_2. This appears to be correlated with higher levels of FeRh alloy formation at lower Fe loadings on the CeO_2 support. Alloyed Fe concentrations exceeding 3 wt% were also found to have a negative impact on ethanol selectivity and also led to an increase in methane selectivity. Therefore, having a large Fe–Rh interface may limit the number of active Rh sites necessary for ethanol production. Additionally, CO hydrogenation on Fe-Rh/CeO_2 catalysts also led to measureable production of

ethylene, but did not appear to be dependent on the presence of either the FeRh alloy or Fe_3C carbide. At present, we are unsure of what is responsible for the promotion of ethylene. Similar to results obtained for the TiO_2–supported catalysts, the Fe_3C carbide phase formed under reaction conditions at high Fe loadings has a minimal effect on CO conversion or product distributions, supporting our earlier conclusion that it is only a spectator in CO hydrogenation. Lastly, changing the support of Rh from TiO_2 to CeO_2 enhances the ethanol selectivity of Rh only catalysts, but also drives down the CO conversion to a fraction of that found for Rh/TiO_2. Both of these effects have been attributed to a strong interface between Rh and CeO_2, similar to that observed by Li *et al.*, where large CeO_2 loadings (>2 wt% CeO_2) decreased the enhancement observed from CeO_2 promotion on Rh/TiO_2.[3]

Chapter 6. Conclusions and Future Directions

The novel results reported in this dissertation indicate that Fe promotion of Rh nanocatalysts for the catalytic hydrogenation of CO to ethanol leads to a suppression of methane at the expense of CO conversion. The structural studies performed by XRD and PDF determined that both the enhancement of ethanol selectivity and suppression of methane and other hydrocarbons (propane, ethane, and butane) is attributed to the alloying of Fe and Rh (FeRh and $Fe_{0.7}Rh_{0.3}$). When TiO_2 is the catalyst support, a large FeOx phase is formed at all Fe loading and metallic Fe deposits are observed in catalysts with Fe loading greater than 4 wt% Fe. During CO hydrogenation, these metallic Fe deposits are carburized and oxidized to Fe_3C and FeOx, respectively. The introduction of Fe_3C does not result in a significant change in product distribution and overall CO conversion, whereas FeOx is suspected to work synergistically with the Fe–Rh alloy to enhance ethanol selectivity and suppress methane formation. Changing the catalyst support to CeO_2 (a more reducible metal oxide) results in a strong metal support interaction between Rh and CeO_2 that leads to the suspected encapsulation of Rh nanoparticles. This encapsulation causes a suppression of CO conversion on the unpromoted Rh catalysts. However, the more reducible CeO_2 appears to promote the reduction of FeOx to metallic Fe that can be alloyed with Rh. This results in an increased Fe–Rh alloy concentration and Fe:Rh ratio in the alloy. This is consistent with the observation of only the Fe-rich alloy, $Fe_{0.7}Rh_{0.3}$, on CeO_2 supported catalysts. Additionally, the promotional effect of Fe−Rh alloy experiences a maximum, where catalysts whose Fe:Rh atomic ratio exceeds 7:3 begin to behave like Fischer-Tropsch catalysts and promote hydrocarbon formation. The suppression of CO conversion and Fischer-Tropsch character at high alloy concentrations is attributed to a change in the ensemble size of Rh active sites, which both decrease CO adsorption and cause the catalysts to behave

more like Fe metal. The overall picture to emerge is that while Fe−Rh alloying can enhance ethanol selectivity, it induces a severe suppression on CO conversion. This suppression of CO conversion prohibits the commercial viability of these catalysts. For this reason, future catalyst design should focus on increasing CO conversion, while maintaining this enhanced ethanol selectivity.

Multiple approaches can lead to a possible increase of CO conversion. Increasing the apparent size of the Rh particles may lead to an enhanced CO conversion that would eventually be suppressed to an appropriate level upon alloying with Rh.[6, 65] This would solve the issue of CO conversion, but would also reduce the viability of the catalyst due to the increased cost. This can be remedied by simulating a larger Rh particle by a core-shell structure consisting of a less expensive core (e.g. Au) and a Rh outer shell. A metal promoter such as Fe could then be added to this catalyst, which will induce an alloying of Fe with the Rh outer shell. A possible complication in this approach is maintaining an outer shell of Rh and Fe during the course of CO hydrogenation, which is a very reducing atmosphere. Alternatively, the catalysts can be completely modified by changing the promoter. Co, Mn, Li, and V enhance CO hydrogenation to ethanol reactivity on supported Rh catalysts.[2, 66-70] Recent studies show that CuCo bimetallic catalysts and K-MoS_2 catalysts have also exhibit high ethanol selectivity and CO conversion.[71, 72] These catalysts may prove to be viable than Rh-based catalysts due to their increased abundance.

In order to understand the intricate details of the ethanol enhancement from Fe−Rh alloying, the study of a model catalyst that represents this system may be required. While the diblock copolymer micelle approach proved incompatible with producing catalysts for use in high-pressure synchrotron studies, it is capable of fabricating a model catalyst system that

represents the complex catalysts studied in chapters 4 and 5 of this dissertation. Surface science techniques such as ambient pressure X-ray photoelectron spectroscopy, temperature programmed desorption and reaction, and ambient pressure scanning tunneling microscopy could be used to provide a more atomistic foundation for the conclusions made from the studies in chapters 4 and 5 as well as study the effects of the catalyst modifications described in the previous paragraph. By combining the results of high-pressure synchrotron structural studies of 'real' catalysts, theoretical calculations, and surface science studies of model bimetallic catalysts, the rational design of catalysts for CO hydrogenation to ethanol can be improved upon.

References

1. **Behrens, M., et al.,** ***The Active Site of Methanol Synthesis over Cu/ZnO/Al2O3 Industrial Catalysts.*** **Science, 2012. 336(6083): p. 893-897.**
2. **Spivey, J.J. and A. Egbebi,** ***Heterogeneous catalytic synthesis of ethanol from biomass-derived syngas.*** **Chemical Society Reviews, 2007. 36(9): p. 1514-1528.**
3. **Li, C.M., et al.,** ***Ce-Promoted Rh/TiO2 Heterogeneous Catalysts Towards Ethanol Production from Syngas.*** **Catalysis Letters, 2013. 143(11): p. 1247-1254.**
4. **Subramani, V. and S.K. Gangwal,** ***A Review of Recent Literature to Search for an Efficient Catalytic Process for the Conversion of Syngas to Ethanol.*** **Energy & Fuels, 2008. 22(2): p. 814-839.**
5. **Burch, R. and M.J. Hayes,** ***The Preparation and Characterisation of Fe-Promoted Al2O3-Supported Rh Catalysts for the Selective Production of Ethanol from Syngas.*** **Journal of Catalysis, 1997. 165(2): p. 249-261.**
6. **Haider, M.A., M.R. Gogate, and R.J. Davis,** ***Fe-promotion of supported Rh catalysts for direct conversion of syngas to ethanol.*** **Journal of Catalysis, 2009. 261(1): p. 9-16.**
7. **Choi, Y. and P. Liu,** ***Mechanism of Ethanol Synthesis from Syngas on Rh(111).*** **Journal of the American Chemical Society, 2009. 131(36): p. 13054-13061.**
8. **Yang, L. and P. Liu,** ***Ethanol Synthesis from Syngas on Transition Metal-Doped Rh(111) Surfaces: A Density Functional Kinetic Monte Carlo Study.*** **Topics in Catalysis, 2014. 57(1-4): p. 125-134.**
9. **Ichikawa, M., et al.,** ***EXAFS evidence for direct rhodium-iron bonding in silica-supported rhodium-iron bimetallic catalysts.*** **The Journal of Physical Chemistry, 1986. 90(7): p. 1222-1224.**
10. **Gogate, M.R. and R.J. Davis,** ***X-ray Absorption Spectroscopy of an Fe-Promoted Rh/TiO2 Catalyst for Synthesis of Ethanol from Synthesis Gas.*** **ChemCatChem, 2009. 1(2): p. 295-303.**
11. **Resasco, D.E., et al.,** ***X-ray absorption near-edge structure evidence for direct metal-metal bonding and electron transfer in reduced rhodium/titania catalysts.*** **The Journal of Physical Chemistry, 1988. 92(1): p. 189-193.**
12. **Tauster, S.J., S.C. Fung, and R.L. Garten,** ***Strong metal-support interactions. Group 8 noble metals supported on titanium dioxide.*** **Journal of the American Chemical Society, 1978. 100(1): p. 170-175.**
13. **Roman, G., M. Martin, and P.S. Joachim,** ***Block copolymer micelle nanolithography.*** **Nanotechnology, 2003. 14(10): p. 1153.**
14. **Cuenya, B.R., et al.,** ***Size- and Support-Dependent Electronic and Catalytic Properties of Au0/Au3+ Nanoparticles Synthesized from Block Copolymer Micelles.*** **Journal of the American Chemical Society, 2003. 125(42): p. 12928-12934.**
15. **Spatz, J.P., et al.,** ***Ordered Deposition of Inorganic Clusters from Micellar Block Copolymer Films.*** **Langmuir, 2000. 16(2): p. 407-415.**
16. **Chupas, P.J., et al.,** ***A versatile sample-environment cell for non-ambient X-ray scattering experiments.*** **Journal of Applied Crystallography, 2008. 41(4): p. 822-824.**
17. **Langford, J.I. and D. Louër,** ***Powder diffraction.*** **Reports on Progress in Physics, 1996. 59(2): p. 131.**
18. **Etter, M. and R.E. Dinnebier,** ***A Century of Powder Diffraction: a Brief History.*** **Zeitschrift Fur Anorganische Und Allgemeine Chemie, 2014. 640(15): p. 3015-3028.**

19. **Proffen, T., et al.,** ***Structural analysis of complex materials using the atomic pair distribution function - a practical guide.*** **Zeitschrift Fur Kristallographie, 2003. 218(2): p. 132-143.**
20. **Juhas, P., et al.,** ***PDFgetX3: a rapid and highly automatable program for processing powder diffraction data into total scattering pair distribution functions.*** **Journal of Applied Crystallography, 2013. 46: p. 560-566.**
21. **Hammersley, A.P., et al.,** ***Two-dimensional detector software: From real detector to idealised image or two-theta scan.*** **High Pressure Research, 1996. 14(4-6): p. 235-248.**
22. **Larson, A.C. and R.B. Von Dreele,** ***General Structure Analysis System (GSAS).*** **Los Alamos Laboratory Report LAUR 86-748, 2004.**
23. **Toby, B.,** ***EXPGUI, a graphical user interface for GSAS.*** **Journal of Applied Crystallography, 2001. 34(2): p. 210-213.**
24. **Ohtani, Y. and I. Hatakeyama,** ***Antiferro-ferromagnetic transition and microstructural properties in a sputter deposited FeRh thin film system.*** **Journal of Applied Physics, 1993. 74(5): p. 3328-3332.**
25. **Houben, A., et al.,** ***Synthesis, Crystal Structure, and Magnetic Properties of the Semihard Itinerant Ferromagnet RhFe3N.*** **Angewandte Chemie International Edition, 2005. 44(44): p. 7212-7215.**
26. **Von Batchelder, F.W. and R.F. Raeuchle,** ***Re-examination of the symmetries of iron and nickel by the powder method.*** **Acta Crystallographica, 1954. 7(5): p. 464-464.**
27. **Willis, B.T.M. and H.P. Rooksby,** ***Change of structure of ferrous oxide at low temperature.*** **Acta Crystallographica, 1953. 6(11-12): p. 827-831.**
28. **R. L. Blake, R.E.H., Tubor Zoltai, and Larry W. Finger,** ***Refinement of the Hematite Structure.*** **The American Mineralogist, 1966. 51(1): p. 7.**
29. **Černohorský, M.,** ***The ratio method for absolute measurements of lattice parameters with cylindrical cameras.*** **Acta Crystallographica, 1960. 13(10): p. 823-826.**
30. **Rao, K.V.K., S.V.N. Naidu, and L. Iyengar,** ***Thermal Expansion of Rutile and Anatase.*** **Journal of the American Ceramic Society, 1970. 53(3): p. 124-126.**
31. **Xu, K., et al.,** ***ε-Iron carbide as a low-temperature Fischer–Tropsch synthesis catalyst.*** **Nat Commun, 2014. 5.**
32. **Chun, D.H., et al.,** ***Highly selective iron-based Fischer–Tropsch catalysts activated by CO2-containing syngas.*** **Journal of Catalysis, 2014. 317(0): p. 135-143.**
33. **de Smit, E., et al.,** ***Stability and Reactivity of $\epsilon-\chi-\theta$ Iron Carbide Catalyst Phases in Fischer−Tropsch Synthesis: Controlling μC.*** **Journal of the American Chemical Society, 2010. 132(42): p. 14928-14941.**
34. **de Smit, E., et al.,** ***Local and long range order in promoted iron-based Fischer–Tropsch catalysts: A combined in situ X-ray absorption spectroscopy/wide angle X-ray scattering study.*** **Journal of Catalysis, 2009. 262(2): p. 244-256.**
35. **Sudsakorn, K., J.G. Goodwin Jr, and A.A. Adeyiga,** ***Effect of activation method on Fe FTS catalysts: investigation at the site level using SSITKA.*** **Journal of Catalysis, 2003. 213(2): p. 204-210.**
36. **Bukur, D.B., et al.,** ***Activation Studies with a Precipitated Iron Catalyst for Fischer-Tropsch Synthesis: I. Characterization Studies.*** **Journal of Catalysis, 1995. 155(2): p. 353-365.**
37. **Yashima, M., S. Kobayashi, and T. Yasui,** ***Crystal structure and the structural disorder of ceria from 40 to 1497 °C.*** **Solid State Ionics, 2006. 177(3–4): p. 211-215.**

38. **Sakellson, S., M. McMillan, and G.L. Haller, *EXAFS evidence for direct metal-metal bonding in reduced rhodium/titania catalysts.* The Journal of Physical Chemistry, 1986. 90(9): p. 1733-1736.**

39. **Ravel, B. and M. Newville, *ATHENA, ARTEMIS, HEPHAESTUS: data analysis for X-ray absorption spectroscopy using IFEFFIT.* Journal of Synchrotron Radiation, 2005. 12(4): p. 537-541.**

40. **Cuenya, B.R., *Synthesis and catalytic properties of metal nanoparticles: Size, shape, support, composition, and oxidation state effects.* Thin Solid Films, 2010. 518(12): p. 3127-3150.**

41. **Valden, M., X. Lai, and D.W. Goodman, *Onset of catalytic activity of gold clusters on titania with the appearance of nonmetallic properties.* Science, 1998. 281(5383): p. 1647-1650.**

42. **Naitabdi, A., et al., *Thermal Stability and Segregation Processes in Self-Assembled Size-Selected AuxFe1-x Nanoparticles Deposited on TiO2(110): Composition Effects.* The Journal of Physical Chemistry C, 2009. 113(4): p. 1433-1446.**

43. **Croy, J., et al., *Size-selected Pt Nanoparticles Synthesized via Micelle Encapsulation: Effect of Pretreatment and Oxidation State on the Activity for Methanol Decomposition and Oxidation.* Catalysis Letters, 2009. 131(1-2): p. 21-32.**

44. **Croy, J.R., et al., *Bimetallic Pt-Metal catalysts for the decomposition of methanol: Effect of secondary metal on the oxidation state, activity, and selectivity of Pt.* Applied Catalysis A: General, 2008. 350(2): p. 207-216.**

45. **Lu, J., et al., *Fabrication of Ordered Catalytically Active Nanoparticles Derived from Block Copolymer Micelle Templates for Controllable Synthesis of Single-Walled Carbon Nanotubes.* The Journal of Physical Chemistry B, 2006. 110(13): p. 6655-6660.**

46. **Roldan Cuenya, B., et al., *Structure and phonon density of states of supported size-selected F57eAu nanoclusters: A nuclear resonant inelastic x-ray scattering study.* Applied Physics Letters, 2009. 95(14): p. 143103.**

47. **Croy, J., et al., *Support Dependence of MeOH Decomposition Over Size-Selected Pt Nanoparticles.* Catalysis Letters, 2007. 119(3-4): p. 209-216.**

48. **Behafarid, F. and B. Roldan Cuenya, *Coarsening phenomena of metal nanoparticles and the influence of the support pre-treatment: Pt/TiO2(110).* Surface Science, 2012. 606(11–12): p. 908-918.**

49. **Porsgaard, S., et al., *Stability of Platinum Nanoparticles Supported on SiO2/Si(111): A High-Pressure X-ray Photoelectron Spectroscopy Study.* ACS Nano, 2012. 6(12): p. 10743-10749.**

50. **Naitabdi, A., F. Behafarid, and B.R. Cuenya, *Enhanced thermal stability and nanoparticle-mediated surface patterning: Pt/TiO2(110).* Applied Physics Letters, 2009. 94(8): p. 083102.**

51. **Chinchen, G.C., et al., *Synthesis of Methanol: Part 1. Catalysts and Kinetics.* Applied Catalysis, 1988. 36(0): p. 1-65.**

52. **Martens, J.H.A., et al., *Structure of rhodium/titania in the normal and the SMSI state as determined by extended x-ray absorption fine structure and high-resolution transmission electron microscopy.* The Journal of Physical Chemistry, 1988. 92(7): p. 1903-1916.**

53. **Guglielminotti, E., et al.,** ***The effect of iron on the activity and the selectivity of Rh/ZrO2 catalysts in the CO hydrogenation.*** **Journal of Molecular Catalysis A: Chemical, 1995. 103(2): p. 105-116.**
54. **Katzer, J.R., et al.,** ***The role of the support in CO hydrogenation selectivity of supported rhodium.*** **Faraday Discussions of the Chemical Society, 1981. 72(0): p. 121-133.**
55. **Johnston, P., R.W. Joyner, and P.D.A. Pudney,** ***The interaction of synthesis gas (CO-H,) with small rhodium particles*** **Journal of Physics: Condensed Matter, 1989. 1(Supplement B): p. SB171- SB176.**
56. **Bengoa, J.F., et al.,** ***Influence of intermediate iron reduced species in Fischer-Tropsch synthesis using Fe/C catalysts.*** **Applied Catalysis A: General, 2007. 325(1): p. 68-75.**
57. **Herranz, T., et al.,** ***Genesis of iron carbides and their role in the synthesis of hydrocarbons from synthesis gas.*** **Journal of Catalysis, 2006. 243(1): p. 199-211.**
58. **Shimizu, K.-i., A. Satsuma, and T. Hattori,** ***Selective catalytic reduction of NO by hydrocarbons on Ga2O3/Al2O3 catalysts.*** **Applied Catalysis B: Environmental, 1998. 16(4): p. 319-326.**
59. **Huang, Y.-y., B.-y. Zhao, and Y.-c. Xie,** ***A novel way to prepare silica supported sulfated titania.*** **Applied Catalysis A: General, 1998. 171(1): p. 65-73.**
60. **Teramura, K., et al.,** ***In Situ Time-Resolved Energy-Dispersive XAFS Study on Photodeposition of Rh Particles on a TiO2 Photocatalyst.*** **The Journal of Physical Chemistry C, 2008. 112(23): p. 8495-8498.**
61. **Kuroda, H., et al.,** ***Temperature-dependence of EXAFS spectra of supported small metal particles.*** **Faraday Discussions, 1991. 92: p. 189-198.**
62. **Johnston, P., et al.,** ***In situ studies of supported rhodium catalysts.*** **Faraday Discussions of the Chemical Society, 1990. 89(0): p. 91-105.**
63. **Tanaka, H., et al.,** ***Comparative study of Rh/MgO modified with Fe, Co or Ni for the catalytic partial oxidation of methane at short contact time. Part I: Characterization of catalysts.*** **Applied Catalysis A: General, 2010. 378(2): p. 175-186.**
64. **Palomino, R.M., et al.,** ***The effect of Fe–Rh alloying on CO hydrogenation to C2+ oxygenates.*** **Journal of Catalysis, 2015. 329(0): p. 87-94.**
65. **Gronchi, P., E. Tempesti, and C. Mazzocchia,** ***Metal dispersion dependent selectivities for syngas conversion to ethanol on V2O3 supported rhodium.*** **Applied Catalysis A: General, 1994. 120(1): p. 115-126.**
66. **Yu, J., et al.,** ***CO hydrogenation over Fe-promoted Rh-Mn-Li/SiO2 catalyst: The effect of sequences for introducing the Fe promoter.*** **Fuel Processing Technology, 2013. 112: p. 100-105.**
67. **Ngo, H., Y.Y. Liu, and K. Murata,** ***Effect of secondary additives (Li, Mn) in Fe-promoted Rh/TiO2 catalysts for the synthesis of ethanol from syngas.*** **Reaction Kinetics Mechanisms and Catalysis, 2011. 102(2): p. 425-435.**
68. **Chen, G.C., et al.,** ***Direct conversion of syngas to ethanol over Rh/Mn-supported on modified SBA-15 molecular sieves: Effect of supports.*** **Fuel Processing Technology, 2011. 92(3): p. 456-461.**
69. **Egbebi, A., et al.,** ***Effect of Li Promoter on titania-supported Rh catalyst for ethanol formation from CO hydrogenation.*** **Catalysis Today, 2010. 149(1-2): p. 91-97.**
70. **Mo, X., et al.,** ***La, V, and Fe promotion of Rh/SiO2 for CO hydrogenation: Effect on adsorption and reaction.*** **Journal of Catalysis, 2009. 267(2): p. 167-176.**

71. **Gao, W., et al.,** ***Core-shell Cu@(CuCo-alloy)/Al2O3 catalysts for the synthesis of higher alcohols from syngas.*** **Green Chemistry, 2015. 17(3): p. 1525-1534.**
72. **Claure, M.T., et al.,** ***Tuning of higher alcohol selectivity and productivity in CO hydrogenation reactions over K/MoS2 domains supported on mesoporous activated carbon and mixed MgAl oxide.*** **Journal of Catalysis, 2015. 324: p. 88-97.**